UNIVERSITÀ DEGLI STUDI DELL'INSUBRIA

Facoltà di Scienze Matematiche, Fisiche e Naturali

Anno Accademico 2006-2007

Laurea Specialistica in Fisica

BENT SILICON CRYSTALS FOR THE LHC COLLIMATION: STUDIES WITH AN ULTRARELATIVISTIC PROTON BEAM

Laureando: Said Hasan
Matricola 611281

Tutor:	Dr. Michela Prest Università degli Studi dell'Insubria
Cotutors:	Dr. Walter Scandale CERN Ginevra Dr. Erik Vallazza INFN sezione di Trieste

A Francesca

Contents

Riassunto **3**

Introduction **6**

1 Crystal channeling **11**
- 1.1 Channeling in straight crystals . . . 12
  - 1.1.1 The continuum approximation . . . 13
  - 1.1.2 Particle motion in the channel . . . 18
  - 1.1.3 Dechanneling . . . 22
  - 1.1.4 Axial channeling . . . 24
  - 1.1.5 Energy loss . . . 27
    - 1.1.5.1 Suppressed electron collisions . . . 28
    - 1.1.5.2 Channeling radiation . . . 29
- 1.2 Bent crystals . . . 32
  - 1.2.1 Particle motion in a bent channel . . . 33
  - 1.2.2 Volume capture . . . 37
  - 1.2.3 Volume reflection . . . 41

2 A channeling application: the beam collimation **49**
- 2.1 Beam collimation . . . 50
- 2.2 The history of crystal collimation . . . 51
  - 2.2.1 The IHEP experiments . . . 52
  - 2.2.2 The RHIC and Tevatron experiments . . . 55
    - 2.2.2.1 The whole arc effect . . . 63
- 2.3 The LHC collimation . . . 68
  - 2.3.1 First phase of the LHC collimation . . . 69
  - 2.3.2 The crystal option . . . 73

3 The September 2006 beam test **81**
- 3.1 Experimental setup . . . 82
  - 3.1.1 The beam . . . 82

3.1.2 The detectors 83
3.1.2.1 AGILE silicon microstrip 84
3.1.2.2 Gas chamber 85
3.1.2.3 Scintillators 86
3.1.3 The goniometer 87
3.1.4 The crystals 88
3.1.4.1 Strip crystals 88
3.1.4.2 Quasimosaic crystals 90
3.2 Experimental procedure 91

4 The September 2006 results 97
4.1 Track reconstruction 98
4.2 Definition of the ST4 crystal horizontal size 104
4.2.1 Check on QM2 and double crystals 112
4.3 Rotational effect 112
4.3.1 Evaluation of the effect (QM2, ST4 crystals) 113
4.3.2 Double crystal scan 122
4.4 Efficiency measurements 131
4.4.1 Method definition (ST4 crystal) 132
4.4.1.1 Reflection efficiency 132
4.4.1.2 Channeling efficiency 136
4.4.1.3 Volume capture and dechanneling 139
4.4.2 The QM2 Crystal 142
4.4.3 Double crystal 146

5 The May 2007 beam test 153
5.1 Going beyond 153
5.2 Setup upgrade 154
5.2.1 Higher precision 157
5.2.2 Faster 158
5.3 New Crystals 160

Conclusion 167

List of figures 172

List of tables 173

List of acronyms 173

The bibliography 180

Riassunto

Questa tesi è incentrata sullo studio del channeling e dei fenomeni ad esso correlati che avvengono in cristalli incurvati. Già nel 1912, Stark ipotizzò che in un cristallo alcune direzioni potevano essere più trasparenti al passaggio di particelle cariche rispetto a quanto accade in un materiale amorfo.

L'idea di Stark rimase tale fino agli anni Sessanta quando diversi esperimenti mostrarono l'anomalo potere penetrante di fasci di ioni in cristalli. Da allora, il channeling in cristalli è stato intensamente studiato a basse energie.
Nel 1976, Tsyganov propose di sfruttare il channeling in cristalli incurvati per deflettere fasci di particelle di alta energia, un'idea che trovò conferma sperimentale nel 1979 al Fermilab; ciò aprì la strada allo sviluppo di numerose applicazioni: dallo steering dei fasci all'estrazione di fasci secondari; dallo sviluppo di microfasci alla produzione di fasci intensi di fotoni di altissima energia.

Il lavoro di tesi è stato svolto nel contesto della collaborazione H8RD22, che sta sviluppando un innovativo sistema di collimazione per LHC basato su cristalli incurvati, finalizzato al raggiungimento della sua luminosità nominale.

Il channeling (come gli altri fenomeni ad esso correlati) ha luogo quando una particella carica attraversa un cristallo allineata rispetto ad un suo piano (o asse); in questo caso, l'interazione tra le particelle e gli atomi del cristallo non è più rappresentata da una serie di eventi non correlati tra loro, ma può essere descritta come il movimento della particella in un campo elettrico medio, che formando una buca di potenziale è in grado di confinare il moto della particella.

Se la particella ha carica positiva, viene confinata in una regione del cristallo lontana dai nuclei atomici caratterizzata da una bassa densità di elettroni, il che si riflette in una soppressione sia dello scattering multiplo sia della perdita di energia per ionizzazione.

La capacità di confinamento mostrata dal potenziale interatomico del cristallo può essere sfruttata per deviare la traiettoria delle particelle che lo attraversano. Ciò si ottiene piegando il cristallo in modo da produrre una curvatura dei piani atomici, che è in grado di deviare la particella carica confinata nella buca di potenziale prodotta dai piani cristallini.

In un cristallo curvo la condizione di tangenza tra il canale formato dalla

buca di potenziale e la traiettoria della particella può avere luogo, a seconda dell'orientazione del cristallo, in un punto al suo interno (nel volume cristallino); in questo caso due fenomeni possono avvenire: la cattura nel canale (volume capture) o, con maggiore probabilità, la riflessione della particella dal lato opposto rispetto alla curvatura (volume reflection).

Un completo studio sperimentale del fenomeno di volume reflection è stato svolto durante l'attività di tesi; infatti l'elevata efficienza ed accettanza angolare che caratterizzano questo processo di deflessione lo rendono particolarmente interessante per essere sfruttato in un sistema di collimazione.

L'idea alla base di tale sistema consiste nell'usare un cristallo curvato come un collimatore primario intelligente, che estragga le particelle dall'alone del fascio dirigendole su un assorbitore; in questo modo si raggiungerebbe un'efficienza molto più elevata di quella ottenibile in un tradizionale sistema di collimazione multi stadio in cui si utilizza un bersaglio amorfo come collimatore primario.

Gli studi effettuati presso gli acceleratori di Fermilab (Illinois), RHIC (New York) e IHEP (Protvino, Russia) per verificare la fattibilità di una collimazione basata sui cristalli costituiscono il primo passo nello sviluppo di questo sistema innovativo indirizzato ai collisori adronici attuali e futuri. I primi due capitoli della tesi contengono un riassunto dei principali concetti riguardanti i fenomeni connessi al passaggio di particelle cariche nei cristalli e una panoramica di ciò che è stato finora fatto al fine di sfruttare questi fenomeni per la collimazione. Particolare enfasi è dedicata al caso di LHC: gli attuali limiti del suo sistema di collimazione sono discussi assieme alle possibilità e alle difficoltà che un sistema basato su cristalli incurvati comporterebbe.

Nel Settembre 2006, si è svolto un testbeam sulla linea di fascio H8 dell'SPS (CERN) con protoni di momento pari a 400 GeV/c; lo scopo dell'esperimento era effettuare misure accurate degli effetti di channeling e volume reflection utilizzando i cristalli di ultima generazione.
Un goniometro ad alta precisione e un sistema di rivelazione basato su detector a microstrip di silicio sono stati installati per allineare il cristallo e misurare gli angoli di deflessione delle particelle. Il setup è descritto in dettaglio nel terzo capitolo.

Il fulcro della tesi è contenuto nel capitolo quattro, in cui si presenta in dettaglio l'analisi dei dati raccolti con i detector a microstrip di silicio (in origine disegnati per il satellite AGILE); i dati provenienti dai diversi detector sono stati utilizzati per ricostruire la traccia delle singole particelle, una novità nel campo del channeling dal momento che di solito per effettuare questi esperimenti si impiegano rivelatori a integrazione.

Grazie alla presenza di un rivelatore ad alta risoluzione posto vicino al cristallo, è stata effettuata l'analisi delle proprietà del cristallo in funzione della posizione in cui è attraversato dalle particelle. Ciò ha permesso la scoperta di un effetto di rotazione del cristallo rispetto alla direzione verticale che è stato successivamente interpretato come una torsione provocata dalle forze applicate per ottenere la curvatura.

La volume reflection è stata osservata per la prima volta a questa energia confermando l'elevata efficienza e accettanza angolare prevista sia teoricamente che tramite simulazioni Montecarlo. È stato effettuato un test con due cristalli allineati, attraversati dal fascio in successione, ottenendo la doppia riflessione delle particelle entranti. I dati relativi a questo test sono stati analizzati riscontrando anche in questo caso la torsione dei cristalli, effetto utilizzato durante l'analisi per discriminare il contributo dei singoli cristalli nel risultato finale.

Si è sviluppato un metodo di misura delle efficienze dei diversi effetti di deflessione prodotti dai cristalli; questo metodo applicato nei diversi casi ha dato risultati consistenti e compatibili con le previsioni teoriche; si è misurata un'efficienza di riflessione superiore al 98%.

L'ultima parte della tesi è una panoramica su come il setup sperimentale è stato modificato per le successive prese dati grazie all'esperienza maturata durante l'esperimento di Settembre 2006 e la successiva analisi dati. Questi cambiamenti si sono concretizzati nel testbeam molto interessante di Maggio 2007 il cui setup sperimentale è brevemente descritto nel capitolo 5 dove sono anche mostrati i miglioramenti ottenuti rispetto al precedente sistema di rivelazione. Durante l'esperimento sono stati compiuti test su multi-riflettori costituiti da più cristalli i cui risultati incoraggianti aprono la strada a prossimi esperimenti su fascio circolante per verificare l'effettiva efficacia di un sistema di collimazione basato su cristalli.

Introduction

This thesis work deals with a phenomenon discovered some time ago: in 1912 in fact, Stark suggested that certain directions in a crystal could be more transparent to the passage of charged particles than what happens in amorphous materials. The idea stood in stand by till the ’60s when several experiments realized that ion beams had an anomalous penetrating capability in crystals.

From there on, channeling in crystals has been intensively studied at low energies. In 1976, a Russian physicist, Tsyganov, proposed to bend a crystal to deflect a high energy beam, an idea which found its experimental confirmation in 1979 at Fermilab, opening the way to several applications from steering beams for collimation purposes to extracting them, from the development of micro-beams to the production of high intensity radiation.

This thesis work has been performed in the research framework of the H8RD22 collaboration, who is developing an innovative crystal-based collimation system which should allow LHC to reach its nominal luminosity.

Channeling (as well as other related phenomena) takes place when a charged particle crosses a crystal aligned with respect to its plane (or axis); in this case, the interaction of the particles with the atoms of the crystal is not anymore a series of uncorrelated events but can be described as the motion of the particle itself in an average electric field which, forming a potential well, is able to confine the particle motion. If the particle is positive, it is confined in a crystal region far from the atomic nuclei with a small electron density, resulting in a suppression of both the multiple scattering (nuclear interactions) and the energy loss via ionization (electronic interactions).

Being able to confine the motion of ultrarelativistic particles, the interatomic crystal potential can be exploited to deviate the particles motion. This is achieved bending the crystal and thus producing a curvature of the atomic planes, which is able to deviate the charged particle confined in the interatomic potential well.

In a bent crystal the tangency condition between the potential well and the particle trajectory can happen inside the crystal (in its volume) resulting in either a capture in the channel (volume capture) or, more probably, in a reflection to the opposite side with respect to the bending (volume reflection).

A complete experimental study of the volume reflection has been performed for this thesis work as its large efficiency and angular acceptance suggest it as a good candidate for a crystal-based collimation system.

The basic idea of such a system is to use a bent crystal as a smart primary collimator, which extracts the incident halo particles from the beam directing them onto an absorber; in this way a cleaning efficiency higher than the one achievable with an amorphous target (used as a primary collimator) should be reached.

The studies performed at the Fermilab (Illinois), RHIC (New York) and IHEP (Protvino, Russia) accelerators to verify the feasibility of a crystal based collimator represent the first step to consider crystal collimation as a possibility for the present and future hadron colliders.

The first two chapters of this thesis contain a review of the main concepts of the phenomena connected with the passage of charged particles in crystals and of the principles and problems of the beam collimation, with particular emphasis on the LHC case.

In September 2006, a beam test was held on the H8 SPS (CERN) beamline with 400 GeV/c protons; the experiment was designed to perform accurate measurements of both the channeling and the volume reflection effects with the last crystal generation.

A high precision goniometer and a silicon microstrip detector system were installed to align the crystal and perform the single particle track reconstruction. The setup and its details are described in the third chapter.

The core of this thesis is contained in chapter 4, where the analysis of the data collected with the silicon detectors (originally designed for the AGILE satellite) is presented in detail, underlining the importance of a setup capable of tracking the single particles, which is in a way a novelty in the crystal field since integrating detectors are usually employed to perform these experiments.

Thanks to the presence of a high resolution detector near the crystal, the analysis of the crystal properties with respect to the different regions of the crystal surface where the particles impinge has been performed. This has allowed the discovery of a rotation of the crystal itself with respect to the vertical position which has been interpreted as a torsion of the crystal due to the forces applied on it to obtain the curvature.

The volume reflection effect has been measured for the first time at this energy confirming the theoretical expectations; a test with two aligned crystals in series has been performed obtaining the double reflection of the incoming protons. The data of the two crystals have been analyzed recognizing the torsion effect and using it to discriminate the contribution of each of them in the final result.

A method to measure the efficiency of the various crystal effects has been developed and applied on different crystals showing its consistence and giving results compatible with both the simulation and the theoretical expectations.

The last part of the thesis is dedicated to a critical review of what should have been changed in the following data taking period, changes that have been implemented leading to a very interesting run in May 2007: from the upgrade of the detectors to obtain a better spatial resolution to the possibility of reconstructing both the incoming and outcoming angle of the particle, from the multireflection studies to the observation of the axial channeling, the data collected in May open the way to the possibility of performing tests on circulating beams and of developing a real collimation setup.

Chapter 1

Crystal channeling

This chapter presents an overview of the main concepts of charged particles channeling in crystals.

The idea that certain directions in a crystal could be more transparent to the passage of charged particles than in an amorphous material was first suggested by Stark [1] (1912) who realized that the motion of a charged particle which enters a crystal at a small angle with respect to a crystal lattice direction can be confined in crystal regions called channels. These regions are characterized by a low nuclear and electronic density so that the energy loss of a particle which is crossing them is reduced. These first ideas on channeling were overshadowed by the interest in the potentiality of X-ray diffraction and put aside until the early 1960s when computer simulations [2] and experiments [3] revealed anomalously long ion ranges in crystals.

The theoretical explanation of the channeling effect has been given by Lindhard [4] who has shown that the particle confinement is caused by the particle coherent scattering with the crystal lattice.

A number of investigations into the channeling of low energy (several MeV) charged particles has been performed [5] and in 1974 these studies were extended to the high energy region, with the experiments started at CERN around the time the SPS was built; the first high energy observation of channeling was made at the PS accelerator with 1.1 GeV/c protons [6].

In 1976 Tsyganov proposed to use a bent crystal to deflect a high energy particle beam [7]; the idea is based on the fact that the channeled particle motion is confined in the channel itself which follows the crystalline planes direction, so when the crystal is bent, channeled particles should follow the crystal curvature. This was experimentally confirmed in 1979 at FNAL in Batavia opening the way for many applications which involve the steering of beams with crystals.

The bent crystal study performed in the following years to improve the crystal behaviour revealed new interesting effects such as volume capture and volume reflection. The last one consists in the particle reflection at the opposite angle with respect to the bending one; its high efficiency and angular acceptance makes it a good alternative to channeling for some specific applications such as beam collimation. After a review of the channeling effect in straight crystals, the theory of bent crystals and of these new effects will be described.

1.1 Channeling in straight crystals

This section presents the theoretical explanation of the channeling effect given by Lindhard [4]. He pointed out that the interaction of a charged particle impinging on a crystal with a small impact angle with respect to the crystallographic axis (or plane) can be described through an average continuous potential generated by the axis (or the plane) instead of the single atoms one.

Any charged particle hitting a solid target experiences a number of collisions characterized by different impact parameters, which determine a variety of processes: from Rutherford scattering to δ-ray emission, from ionization to X-ray production. In an amorphous material or a misaligned crystal, these collisions are uncorrelated so the yield of the different processes is independent from the target orientation.

If the target material is monocrystalline, the scenario changes; in fact, a crystal is a regular arrangement of atoms located on a lattice so that, depending on the observation, the atoms are arranged in strings or planes, as shown in fig. 1.1.

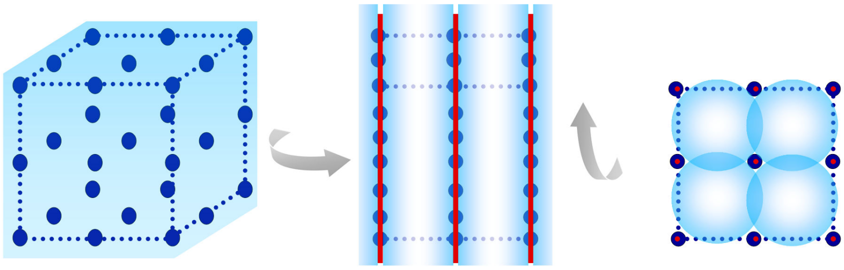

Figure 1.1: A regular crystalline structure; from the reader point of view the atoms appear: (left) in a non-ordered structure; (center) arranged in planes, after a rotation around an axis; (right) arranged in strings after a rotation around the orthogonal axis.

When the motion of a charged particle is aligned with respect to the crystalline planes or axis, a coherent interaction with the atoms of the planes (axis) takes place. This coherent scattering results, for positive particles, in the suppression of the processes requiring small impact parameters in the collision between the particle itself and the atoms such as nuclear reactions, large angle scattering, energy loss and so on.

This happens because the particle is confined in the space between the crystalline planes (axis) by the electric potential originated by the atoms in the planes (string).

When a charged particle is aligned to a crystal plane (axis), in fact, its interaction with the atoms can be described through the electric potentials of a continuous charged distribution obtained by smearing the atomic charge along the crystal planes (string); the periodicity of these planar (axial) charge distributions forms a series of potential-wells which can confine the charged particles crossing the crystal (sec. 1.1.1).

When the motion of a particle is confined between the crystalline planes, the particle is said to be in a planar channeling condition (sec. 1.1.2), while, if it is confined between the crystal axes, it is said to be in axial channeling (sec. 1.1.4).

The particles are confined in the channel as long as their transversal (to the channel direction) momentum is not sufficient to overcome the potential barrier; this happens until the angle between the particle and the channel is smaller than a critical value which depends on the particle energy and on the potential barrier height.

According to this, a channeled particle can leave the channel if it gains a transversal momentum component large enough; this phenomenon called dechanneling (sec. 1.1.3) can happen thanks to the particle scattering in the channel.

When a particle is channeled, it is confined in a crystal region far from the nuclei with a reduced electron density so that its energy loss is reduced (sec. 1.1.5) in comparison with the amorphous one. Also the radiative processes which are significant for light particles are strongly affected by the channeling interaction, resulting in a coherent radiation emission called channeling radiation (sec. 1.1.5.2) which, for positive particles, differently from the bremsstrahlung process, shows a narrow peak.

1.1.1 The continuum approximation

A particle going through an amorphous material or a misaligned crystal experiences *uncorrelated* collisions with single atoms through a variety of processes depending on the different impact parameters; among them, angular scattering with nuclei and energy loss with atomic electrons are the most common. These events are uncorrelated so the global effect can be computed considering the single collisions weighed by the material density.

If a positive charged particle hits a crystal with a small angle with respect to the crystallographic axis (or plane), its motion is not determined any more by the single atom scattering but by the coherent effect of the atomic axis or plane. In this condition (low angle approximation) the single atoms potential can be replaced by an average continuous potential.

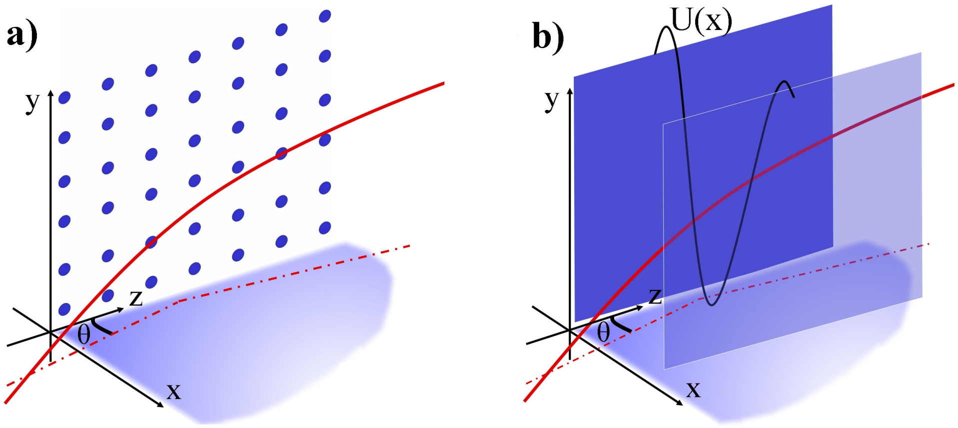

Figure 1.2: a) A particle (red line) moving in a crystal misaligned with respect to the axis but at a small angle with respect to the crystalline plane (placed in the $z-y$ plane). b) The particle experiences an average potential due to the planes ($U(x)$, represented by the black line).

The scheme in fig. 1.2(a) shows a particle whose motion in the crystal is misaligned with respect to the atomic string but it is at a small angle with respect to the atomic plane. This means that the particle feels the effect of the whole plane instead of the single atoms the plane is composed of; in this condition the electric field of two neighbouring planes can trap the particle, an effect called planar channeling. If the particle is aligned not only with the crystal plane but also with the crystal axis it can be contained in the potential generated by the atomic string and the effect is known as axial channeling. From now on the planar channeling will be presented in detail being the topic of this thesis work. The axial channeling will be briefly described in sec. 1.1.4.

The effect of the whole plane on the particle is described by a continuous potential (fig. 1.2(b)); the value of the potential can be computed averaging on the y and z directions as shown in the following equation:

$$U_{pl}(x) = N d_p \int_{-\infty}^{\infty} \int_{-\infty}^{\infty} V(x,y,z) \mathrm{d}y \mathrm{d}z \tag{1.1}$$

where N is the number of atoms per unit volume, d_p is the interplanar spacing, so that $N \cdot d_p$ represents the planar atom density; $V(x,y,z)$ is the potential between the particle and the single atom and it is given by:

$$V(r) = \frac{Z_i Z e^2}{r} \Phi\left(\frac{r}{a_{TF}}\right) \tag{1.2}$$

where Z_i and Z are the atomic numbers of the particle and the atom, r is the distance between them (so in eq. 1.1, $V(x,y,z) = V(\sqrt{x^2+y^2+z^2})$). The first term of eq. 1.2 represents the point-like Coulomb potential, while $\Phi(r/a_{TF})$ takes into account the atom charge distribution; a_{TF} is the Thomas Fermi screening radius: $a_{TF} = 0.8853 a_B Z^{-1/3}$, with $a_B = 0.529$ Å. Lindhard [4] suggested the following analytical approximation for the screening function:

$$\Phi\left(\frac{r}{a_{TF}}\right) = 1 - \left(1 + \frac{3(a_{TF})^2}{r^2}\right)^{-1/2} \tag{1.3}$$

Putting together these three equations the continuous potential generated by the single crystal plane can be obtained:

$$U_{pl}(x) = 2\pi Z_1 Z e^2 N d_p \left(\sqrt{x^2 + 3(a_{TF})^2} - x\right) \tag{1.4}$$

To complete the picture, this expression which represents the static lattice potential has to be modified taking into account the atomic thermal vibrations that cause distortions of the lattice structure. The atoms vibration can be considered independent and distributed according to a gaussian probability distribution so the potential generated by the crystal plane should be averaged over this distribution. The effect of the thermal vibration is small: the one dimensional rms displacement of silicon atoms at the temperature of 300 K is $\rho = 0.075$ Å to be compared with the silicon lattice constant $L_c = 5.431$ Å [8]. Qualitatively the main effect of the thermal vibration occurs at small distances from the plane (string) where the infinite static potential is modified to have a finite maximum as shown in fig. 1.3.

A charged particle which moves in the crystal is affected by the sum of the different planes potential and the resulting potential is:

$$U(x) \simeq U_{pl}\left(\frac{d_p}{2} - x\right) + U_{pl}\left(\frac{d_p}{2} + x\right) - 2U_{pl}\left(\frac{d_p}{2}\right) \tag{1.5}$$

where only the contribution of the two nearest planes is considered (first two terms); the origin of the transversal coordinate x is chosen in the middle of the two planes and the third term fixes the potential value at the origin to zero ($U(0) = 0$).

The most used crystals for channeling investigation in high energy experiments are made of silicon (more rarely germanium); this is due to the development status of the semiconductor technology. These crystals belong to the diamond

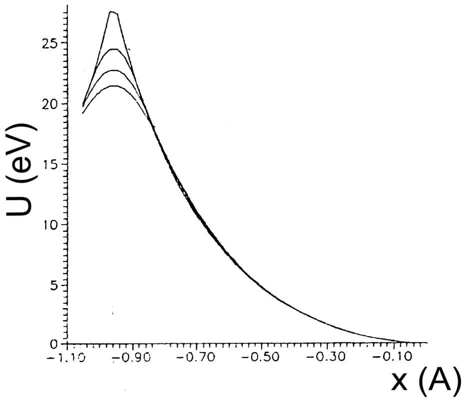

Figure 1.3: The potential generated by the (110) silicon plane computed in the Moliér approximation for different temperatures. From top to bottom the lines correspond to T=0 K (static), 77 K, 300 K and 500 K.

group and they are characterized by the covalent bond so each atom is linked to four neighbours forming a regular tetrahedron with a face centered cubic (fcc) crystalline structure as shown in fig. 1.4.

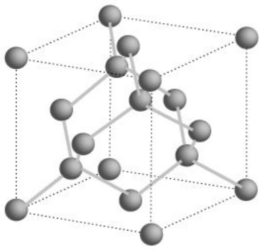

Figure 1.4: The diamond cubic lattice: two identical face centered cubic lattices pushed one into the other and shifted along the bulk diagonal by one quarter of its length.

Fig. 1.5 shows the principal planes of the fcc crystalline structure indicated by the Miller indices; each plane has a different interatomic distance (d_p) which determines the planar potential (given in eq. 1.5). The planes useful for channeling are (110) and (111) while (100) generates a too small potential to be of any interest in this frame.

Table 1.1 summarizes the characteristics of silicon, germanium and tungsten crystals underlining the maximum potential value reached for each plane. The particular structure of the diamond group crystals (fig. 1.4) involves two different interplanar distances which generate two interplanar channels with different characteristics; in table 1.1 these channels are called 111s (short) and 111l (long).

In fig. 1.6 the interplanar potential trends for the (110) and (111) planes in silicon are plotted while the dashed line (fig. 1.6 (a)) is the harmonic potential approximation that will be used in sec. 1.1.2 to derive the particle motion in the

	Channel	L_c	d_p [Å]	a_{TF} [Å]	ρ [Å]	Z	$\mathbf{U}(\mathbf{x_c})$ [eV]
Si		5.43		0.194	0.075	14	
	110		1.92				**16**
	111l		2.35				**19**
	111s		0.78				**4.2**
Ge		5.65		0.148	0.085	32	
	110		2.00				**27**
	111l		2.45				**30**
	111s		0.81				**7.2**
W		3.16		0.112	0.050	74	
	100		1.58				**63**
	110		2.24				**105**

Table 1.1: Parameters of some planar channels in silicon, germanium and tungsten crystals. The potentials are given in the Moliér approximation and $x_c = d_p/2 - 2\rho$.

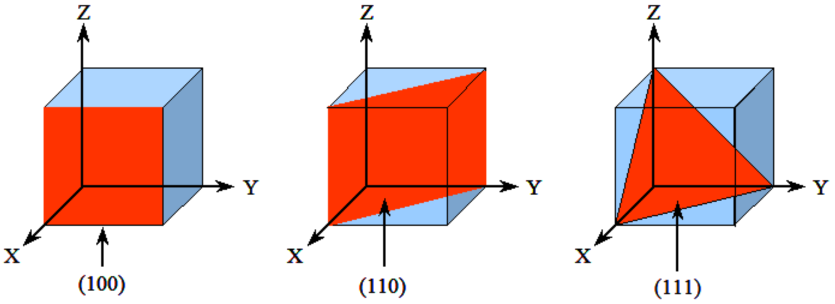

Figure 1.5: Orientation of the most important crystallographic planes in the cubic lattice system, indicated by the Miller indices.

channel.

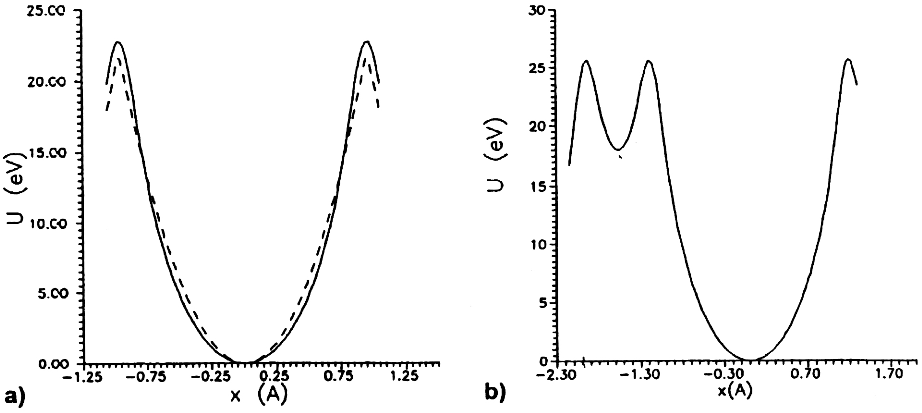

Figure 1.6: The interplanar Moliér potential for: a) the (110) Si channel and b) the (111) Si channel which is characterized by two potential wells corresponding to its two interplanar distances. The dashed line is the harmonic potential approximation.

1.1.2 Particle motion in the channel

A charged particle moving in a crystal is in a planar channeling condition if it has a transversal momentum component (with respect to the crystalline planes) insufficient to overcome the potential well, as it is schematically shown in fig. 1.7.

In this condition, the particle experiences a series of correlated collisions; although these are quantum events the particle motion can be described in the clas-

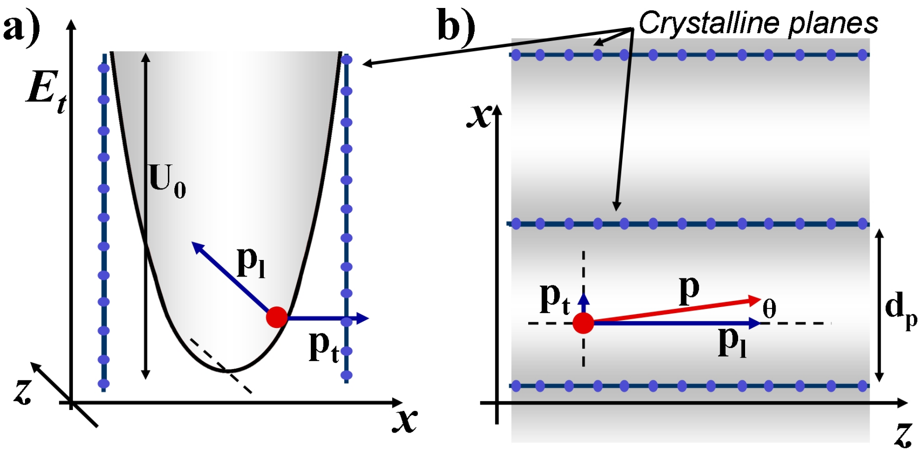

Figure 1.7: a) A particle contained in the interplanar crystalline potential. b) Top view of the channels with the same particle, its transversal (p_t) and longitudinal (p_l) (with respect to the planes direction) momentum components are shown. The angle $\theta = p_t/p_l$ represents the small misalignment between the particle and the plane.

sical mechanics frame, thanks to the large number of energetic levels accessible in the interplanar potential.

Taking into account the harmonic potential approximation $U(x) = U_0\left(x\frac{2}{d_p}\right)^2$ the energy spacing between levels is $\hbar\left(\frac{8U_0}{d_p^2 M_o}\right)^2$ where M_o is the oscillating mass; so the classical approximation is valid if:

$$N_o = \frac{d_p}{\hbar\sqrt{8}}\sqrt{U_0 M_o} \gg 1 \tag{1.6}$$

where N_o is the number of the accessible energetic levels; for a particle trapped in the channel, M_o is the relativistic mass so the condition 1.6 is always fulfilled for heavy particles (protons) while for light ones (electrons and positrons) the classical approach becomes valid in the 10-100 MeV range.

The condition to apply the continuum approximation (sec. 1.1.1) is that the particle moves at a small angle with respect to the crystalline planes so $\theta \ll 1$; since $\theta = p_t/p_l$, it follows that $p_t \ll p_l$. Using this information the total conserved energy of the system can be approximated:

$$E = \sqrt{p_t^2 + p_l^2 + m^2c^2} + U(x) \simeq \frac{p_t^2c^2}{2E_l} + E_l + U(x) \tag{1.7}$$

where $E_l = \sqrt{p_l^2c^2 + m^2c^4}$; p_l is not affected by the potential so it is conserved, which means that E_l is conserved and thus $\frac{p_t^2c^2}{2E_l} + U(x)$ is conserved too, due to energy conservation. This quantity which is called the particle transversal energy E_t can be expressed as a function of the angle between the particle direction and the crystal planes ($\theta = p_t/p_l$):

$$E_t = \frac{p_l^2c^2}{2E_l}\theta^2 + U(x) \simeq \frac{p^2c^2}{2E}\theta^2 + U(x) = \text{const.} \tag{1.8}$$

where in the second equality according to the condition $p_t/p_l \ll 1$, p_l has been approximated with the total momentum p, while E_l with the total energy E. This equation defines the particle trajectory in the (x,θ) plane; in the harmonic approximation these trajectories represent a set of ellipses depending on the value of E_t as shown in fig. 1.8.

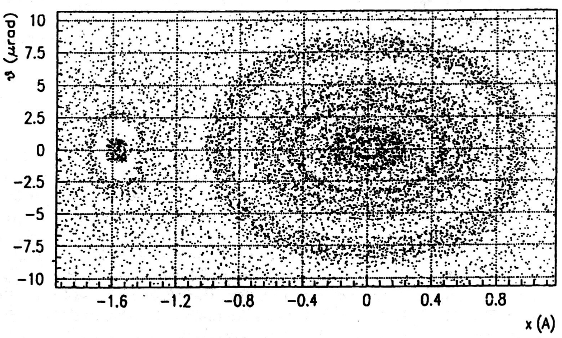

Figure 1.8: Simulated trajectories of 450 GeV/c protons in the phase space (x,θ) in the (111) silicon plane for a straight crystal. The different ellipses correspond to different transversal energy values [9].

The particle is trapped in the channel if its transversal energy is smaller than the maximum value of the potential barrier that is $E_t < U_{max}$; this in turn becomes the condition defining the possible values of θ and x for a channeled particle:

$$\frac{p^2c^2}{2E}\theta^2 + U(x) \leq U_{max} \tag{1.9}$$

U_{max} is reached at the plane itself ($x = d_p/2$). In this position the particle could be immediately removed from the channel by the scattering with the nuclei, which means that below a minimum distance with respect to the plane, the particle is still not in channeling. This distance is about a_{TF} so the maximum transversal position reachable in channeling is $x_c \simeq d_p/2 - a_{TF}$ and the corresponding potential value $U(x_c)$ represents the maximum of the potential U_{max}. To be precise the atoms thermal vibration has to be taken into account as the nuclear motion increases the effective transversal dimension of the atomic plane. Experiments [10] and computer simulations [11] have shown that 5ρ is a good approximation for the atomic layer thickness and for very high energy particles (multi TeV region) this thickness decreases to 2ρ due to the reduction of the scattering effects; so a better estimation of the critical transversal value is $x_c \simeq d_p/2 - a_{TF} - 2\rho$.

Taking into account the relation $pc^2 = vE$, eq. 1.9 becomes:

$$E_t = \frac{pv}{2}\theta^2 + U(x) \tag{1.10}$$

which allows to compute the maximum angle (θ) available for channeling, for particles which enter the crystal in the center of the channel that is with the minimum value of the potential energy ($U(0) = 0$); in this case eq. 1.9 becomes $pv\theta^2 \leq U_{max}$ and the critical angle θ_c is:

$$\theta_c = \sqrt{\frac{2U_{max}}{pv}} \tag{1.11}$$

For a silicon crystal U_{max} is ≈ 20 eV (see table 1.1) thus θ_c is 280 μrad at 500 MeV, 9.42 μrad at 450 GeV and 2.39 μrad at 7 TeV. It has to be noted that the critical angle decreases as the square root of the energy while the multiple scattering as the energy of the incoming particles so the effects due to multiple scattering which (as will be shown) reduce the channeling efficiency become less important at high energy.

The angle θ can be expressed as $\frac{\mathrm{d}x}{\mathrm{d}z}$ where dx and dz are the infinitesimal increase in the transversal and longitudinal spatial directions (see fig. 1.7); with this substitution eq. 1.10 gives the following differential equation which describes the particle motion in the channel:

$$E_t = \frac{pv}{2}\left(\frac{\mathrm{d}x}{\mathrm{d}z}\right)^2 + U(x) \tag{1.12}$$

Differentiating with respect to z:

$$pv \cdot \frac{\mathrm{d}^2x}{\mathrm{d}z^2} + U'(x) = pv \cdot \frac{\mathrm{d}^2x}{\mathrm{d}z^2} + U_0 \cdot \frac{8x}{d_p^2} = 0 \tag{1.13}$$

The solution of this equation gives the particle trajectory corresponding to a sinusoidal oscillation in the channel:

$$x = \frac{d_p}{2}\sqrt{\frac{E_t}{U_0}}\sin\left(\frac{2\pi\cdot z}{\lambda}+\phi\right) \tag{1.14}$$

The length of the oscillation period is $\lambda = \pi d_p\sqrt{\frac{pv}{2U_0}}$; for example for a 450 GeV/c proton in silicon $\lambda \sim 27$ μm.

1.1.3 Dechanneling

In the particle trajectory derivation (sec. 1.1.2) the transversal energy conservation is assumed, which in real crystals is not exactly true because of the scattering processes with electrons, the difference between the real potential and the continuum approximation as well as the crystal lattice defects. The transversal energy of the channeled particles can in fact grow and eventually overcome the potential well causing the particles exit from the channel; this process is called *dechanneling*. The inverse process is also possible: particles which go through the crystal misaligned with respect to its plane (amorphous condition) can lose their transversal energy and be trapped in the channel, an effect known as *volume capture* (sec. 1.2.2).

Dechanneling is a complex phenomenon and its full description, which includes the scattering effects in the real crystal, is achieved through Montecarlo computer simulations [12]; in principle the reduction of the number of the channeled particles as a function of the crystal depth can be approximated by an exponential decay [9]:

$$N = N_0 e^{-\frac{L}{L_D}} \tag{1.15}$$

where L is the length of the crystal and L_D the dechanneling length given by:

$$L_D = \frac{256}{9\pi^2}\frac{pv}{\ln(2m_e c^2\gamma I^{-1})-1}\frac{a_{TF}}{Z_i r_e m_e c^2} \tag{1.16}$$

where I is the ionization potential (for silicon is $\simeq 172$ eV), m_e is the electron rest mass, r_e the classical electron radius and Z_i is the charge number of the particle. Eq. 1.15 and 1.16 are computed using the diffusion formalism, since soft collisions ($\theta_s \ll \theta_c$) dominate; this means that the dechanneling process acts on a long distance scale with respect to the single collision. Moreover in deriving the expression 1.16 only the dominant electron contribution is taken into account as the potential fluctuation caused by the discreteness of the crystal lattice has a much smaller influence [13]: note that the particle oscillation length in the channel (λ)

Energy (GeV)	0.5	14	120	400	7000
$\mathbf{L_D}$ (cm)	0.5	1.0	7.2	21.9	316

Table 1.2: Values of the dechanneling length for the single scattering at large angle as a function of the energy.

is a factor 10^5 larger than the interatomic spacing (d_p).
Finally, the Lindhard approximation for the interplanar atomic potential given in eq. 1.4 is used in the computation of eq. 1.16.

The dechanneling length is an indication of the particle tendency to remain in channeling; its second term (eq. 1.16) depends on the energy and states that L_D linearly increases with the energy (apart from a small logarithmic correction), as expected given that the multiple scattering effects linearly scale with energy. In table 1.2 different dechanneling values are computed as a function of the energy for the (110) channel in silicon.

The third term (eq. 1.16) gives the dependence on the material and its orientation; it states the proportionality of L_D with d_p so, for example, the ratio L_D^{111}/L_D^{110} (the dechanneling length for the (111) and (110) orientation) should be of the order of $d_p^{111}/d_p^{110} = 1.23$ (see table 1.1) which is in good agreement with the measured value of 1.4 ± 0.2 [14]. It should be clarified that though two different channels correspond to the (111) orientation their interplanar distance is in the ratio $3d_p^s = d_p^l$ so particles moving in the small interplanar interval d_p^s in a long crystal can be ignored as their dechanneling length is a factor 3 shorter.

As already stated, the diffusion formalism can be applied because of the soft scattering relative importance; since the angular kick is $\theta_s \ll \theta_c$, the angle of the particle is changed by frequent infinitesimal steps. In the MeV energy range this approximation works well since the maximum possible angular kick for a single collision $\theta_s^{max} \simeq 1.4 m_e/M$ (where M is the particle mass) [9] is smaller than the critical angle θ_c; for example, in silicon for proton energies up to 10 MeV, $\theta_s^{max} \simeq 0.77$ mrad while $\theta_c > 1$ mrad.

In the energy range of $\simeq 100$ GeV, $\theta_c \simeq 10$ μrad therefore rare collisions with $\theta_s > \theta_c$ can happen: the particle is thrown outside the channel and this event cannot be described by the diffusion formalism. Also in this case a characteristic length along which the single hard scattering events occur can be computed [12]:

$$L_{single} = \frac{4 a_{TF} d_p p v}{Z_i e^2} \tag{1.17}$$

The comparison between the two dechanneling lengths shows that the diffusion model provides a good description of the dechanneling process; in fact the contribution of the single hard scattering is small with respect to the diffusion one:

$L_D \simeq 0.55\ \mathrm{m} \cdot p$ [TeV/c] while $L_{single} \simeq 10\ \mathrm{m} \cdot p$ [TeV/c]. Thus the experimental data can be reasonably fit using the diffusion formalism. Fig. 1.9(a) shows the computed trend of L_D as a function of the energy for the (110) and (111) orientation in silicon compared to the single scattering one; in fig. 1.9(b) some experimental results are presented to show the linearity of L_D with respect to the particle pv.

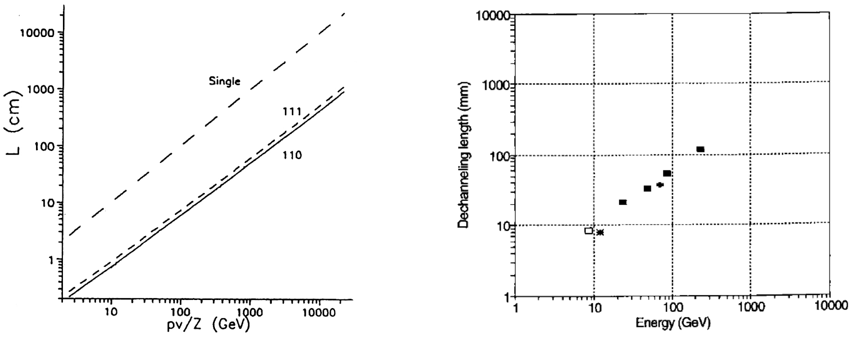

(a) (b)

Figure 1.9: a) Computed L_D trend as a function of pv (note that $pv \simeq E$ for relativistic particles) for the (110) Si plane (solid line) and the (111) Si plane (short dashes). The line with the long dashes corresponds to the dechanneling length for single scattering. b) Measurements of the dechanneling length in silicon in various experiments [8].

The given dechanneling description is valid for positive charged particles which are channeled in the central region of the crystalline plane where the electron density is small and almost constant. On the contrary negative particles are channeled around the atomic plane as their potential well minimum corresponds to the nuclei positions. The high electron and nuclear densities in this region, increasing the scattering probability, makes the dechanneling length much shorter than the positive particles one.

1.1.4 Axial channeling

Sec. 1.1.1 has demonstrated that a particle moving at small angles ($\theta < \theta_c$) with respect to a crystallographic plane feels the electric field generated by the atoms in the plane as if produced by a continuous charge distribution with planar symmetry. The periodicity of these planar charge distributions (due to the crystal lattice structure) forms a series of potential wells which can trap the charged particles crossing the crystal; these particles are said to be in a planar channeling condition.

A particle can be aligned with respect to the crystal planes in a direction (for example the vertical one, fig. 1.2) and at the same time in the perpendicular one. In this case the particle is moving at a small angle relative to the crystal atomic strings and it feels the electric field generated by the atoms of the string as if produced by a charge distribution with cylindrical symmetry. Fig. 1.10 shows that the interaction between the atoms of the string and the particle can be described with a continuous potential with axial symmetry.

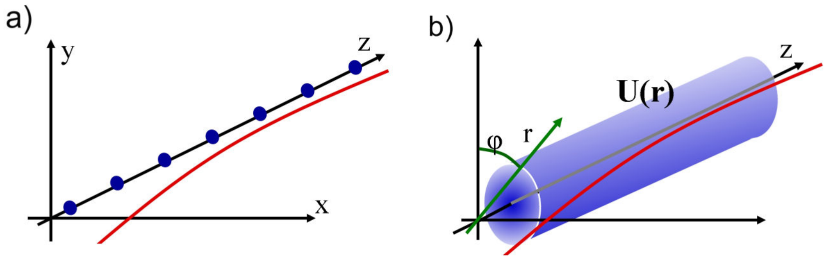

Figure 1.10: a) A particle moving at a small angle with respect to a crystal axis. b) The continuous potential with radial symmetry as it is felt by the aligned particle.

The potential of an isolated atomic string $U_A(r)$ in the Lindhard approximation (eq. 1.3) is:

$$U_A(r) = \frac{Z_i Z e^2}{a_i} \ln\left(1 + \frac{3a_{TF}^2}{r^2}\right) \tag{1.18}$$

where a_i is the interatomic spacing in the string, r is the distance between the particle and the axis, a_{TF} is the Thomas Fermi constant whose values for the most common crystals are given in table 1.1. The transverse electric field generated as the sum of the fields produced by the single atomic strings shows a rather complicated structure (fig. 1.11).

The negative charged particles which enter the crystal aligned with its axis can be trapped by the strong field of the atomic string and, being attracted by the positive charge of the nuclei, their motion is confined near the atomic strings. The positive charged particles, on the other hand, may be captured in the well of a minor potential placed between the atomic strings.

The particle motion in the field $U(r)$ with cylindrical symmetry [16] is characterized by two conserved quantities, the angular momentum J and the energy in the transverse plane E_t, which can be decomposed into a radial component and a circular one. In fact, the angle between the particle trajectory and the crystal axis (z) which is $\theta = \sqrt{\mathrm{d}x^2 + \mathrm{d}y^2}/\mathrm{d}z^2$ can be expressed in the cylindrical coordinate

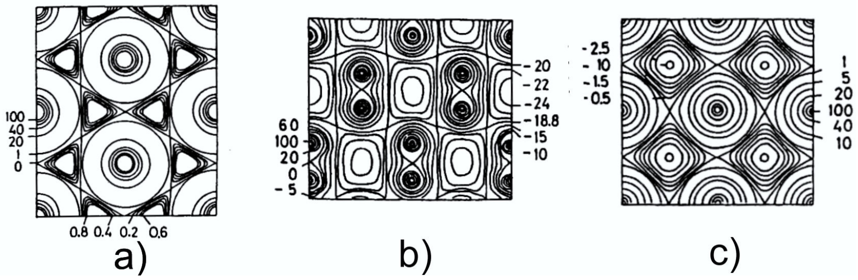

Figure 1.11: Axial potential computed [15] with the use of the Moliér approximation, in the following orientations: a) (111) Si; b) (110) Si; c) (100) Si. The numbers give the potenvial in eV.

system:

$$\theta = \sqrt{\left(\frac{\mathrm{d}r}{\mathrm{dz}}\right)^2 + \left(\frac{r\mathrm{d}\phi}{\mathrm{dz}}\right)^2} = \sqrt{\theta_r^2 + \theta_\phi^2} \tag{1.19}$$

According to this and taking into account that the angular momentum is $J = p \times r = pr\theta_\phi$, eq. 1.12, which gives the transversal energy value and was computed for the planar channeling case, becomes:

$$E_t = \frac{pv}{2}\theta^2 + U(r) = \frac{pv}{2}\theta_r^2 + \frac{J^2}{2M\gamma r^2} + U(r) \tag{1.20}$$

where the last two terms are the effective potential in which $\frac{J^2}{2M\gamma r^2}$ represents a centrifugal term whose effect is to move the effective potential minimum aside from the channel center ($r = 0$) where the real $U(r)$ has the minimum; so, as J increases, the effective potential minimum moves farther from the atomic string for the negative particles and nearer to them for the positive ones.

The resulting motion in the channel will be a radial oscillation around the effective potential minimum together with a rotation of the radial direction around the axis. Taking into account the angular relations: $\theta_r = dr/dz$ and $J = pr^2 \cdot d\phi/dz$, from eq. 1.20 the following differential equations which describe the particle trajectory in the (z, r, ϕ) space can be obtained [9]:

$$z = \int \frac{dr}{\frac{2}{pv}[E_t - U(r)] - \frac{J^2}{p^2 r^2}} + \text{const.} \tag{1.21}$$

$$\phi = \int \frac{\frac{J^2}{r} dr}{2M\gamma[E_t - U(r)] - \frac{J^2}{r^2}} + \text{const.} \tag{1.22}$$

The first one gives the longitudinal coordinate z as a function of the radial one r while the second one describes the motion in the transversal plane giving the angular coordinate ϕ as a function of the radial one r. A classical description of this motion called 'rosette' motion has been given by Kumm et al [17], while a quantum mechanical treatment can be found in [18].

As in the planar channeling case the condition for axial channeling is that the transversal energy E_t does not overcome the maximum value of the potential well U_0. This condition can be transformed in the request for the particle angle with respect to the axis (θ) to be smaller than a critical value $\theta_c = \sqrt{2U_0/pv}$ as shown in sec. 1.1.2. The U_0 values for the most important axes in Si, Ge, W crystals are given in table 1.3.

crystal	Si			Ge			W		
axis	100	110	111	100	110	111	100	110	111
U_0 (eV)	89	114	105	157	203	185	842	979	979

Table 1.3: The potential well depth of some axial channels of silicon, germanium and tungsten crystals, calculated in the Moliér approximation at room temperature.

Comparing these U_0 values with the ones of the planar case given in table 1.1, the critical angle is $2-3$ times greater for the axial channeling than for the planar one. This favours the axial channeling with respect to the planar one but on the other hand for positive charged particles the interatomic axial channels are small, asymmetric and rather dependent on the axial direction while for the negative ones the dechanneling (the probability to exit from the channeling condition, sec. 1.1.3) is large as they travel near the atoms and so the nuclear scattering can rapidly change their transversal energy.

1.1.5 Energy loss

The most relevant manifestation of channeling in straight crystals is an anomalous energy loss with respect to the amorphous material or misaligned crystals. The energy loss for ionization is suppressed because channeled particles are confined in a region of the crystal with a small electron density (sec. 1.1.5.1) while the energy irradiated by a channeled light particle (a positron or an electron) is more intense than the standard bremsstrahlung one and has a peculiar peaked structure as described in sec.1.1.5.2.

1.1.5.1 Suppressed electron collisions

The charged particle energy loss in the materials is mostly due to electronic collisions. In an amorphous material or in a misaligned crystal the scattering processes are independent meaning that the impact parameter of a collision is not influenced by the previous one. In this case the energy lost by relativistic particles follows the Landau distribution [19]. The energy loss at high energies is due to the two equal contributions of the hard and close collisions and of the soft and distant ones, because of the equipartition rule [4].

In channeling, particles are subject to a highly correlated series of collisions which result in the suppression of the large angle Rutherford scattering, of nuclear reactions and also of close scattering with the electrons which is the most significant way of energy loss.

This happens because channeled particles (if positive) move in a crystal region where the electron density $\rho_e(x)$ is lower than the average amorphous value. Fig. 1.12(a) shows the electron density in a silicon crystal (average along the (110) and (111) planes) as a function of the transverse coordinate; it is obtained from the second derivative of the interplanar Moliér potential (according to the Poisson law $\rho_e(x) = U''(x)$). Fig. 1.12(b) presents the experimental evidence of the close electron scatterings reduction inside the channel. It shows the δ-ray yield as a function of the incident angle with respect to the (110) axis, for 11.9 GeV protons impinging on a 0.54 mm Ge crystal [20]: the δ-rays are atomic electrons emitted in hard knock on collisions, and since they can be produced only in close impacts their yield is proportional to the electron density along the particle trajectory.

The suppression of the close scatterings in the channel produces the decrease of both the mean value and the spread of the energy loss for the channeled particle. This reduction depends on the average transversal position that the particle keeps in the channel therefore on the transversal energy; fig 1.12(a) shows the mean energy loss (dashed line) superimposed to the electron density as a function of the transversal position in the channel.

According to this, the minimum energy loss is the one of the particle with the minimum transversal energy which goes through the crystal in the channel center where the electron density is minimum. Because of the equipartition rule, the ratio between the energy loss in the channeling and in the amorphous condition is:

$$\frac{\langle \Delta E \rangle_{chan}}{\langle \Delta E \rangle_{amo}} = 0.5[1+\rho_e^r(0)] = \frac{12(d_p/a_{TF})}{[(d_p/a_{TF})^2+12]^2} \simeq 0.6 \tag{1.23}$$

where the second term represents the addition of the contribution from the distant soft collisions (which does not change in channeling) and from the close ones which scales down with the electron density; $\rho_e^r(0)$ represents the reduced electron density evaluated in the center of the channel. The numerical value is computed

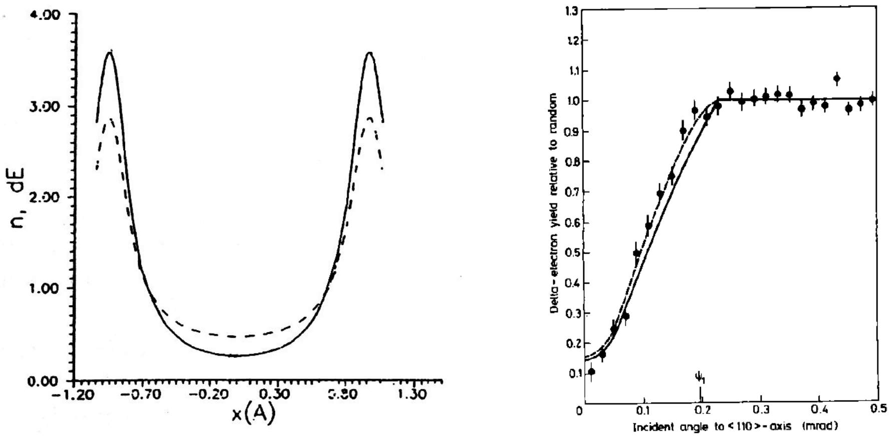

(a) (b)

Figure 1.12: a) The electron density (solid line) and the mean energy loss (dashed line) as a function of the transversal coordinate normalized to the amorphous value, in a Si crystal aligned with respect to the (110) plane. b) Measured and calculated δ-ray yield as a function of the incident particles angle.

using the Lindhard potential approximation (eq. 1.4, 1.5), for the (110) and (111) silicon planes.

The energy lost in the crystal is a useful experimental observable as it is an important link between the electronic properties of the crystal and the particle state in it. It can be used to study the crystal properties [20] or to tag the channeled particle, greatly simplifying the channeling measurements especially when the efficiency is low (as it happens with a divergent beam ($\theta_{beam} \gg \theta_c$)) and the channeled beam fraction is difficult to identify. To perform this measurement the crystal (which is a semiconductor) is doped so that the deposited energy in the depleted crystal zone can be collected.

In Fig 1.13 the energy loss distribution of 15 GeV/c momentum protons in 0.74 mm of germanium in amorphous orientation is compared with: (a) the energy loss distribution of the particle in planar channeling, and (b) the one of the axial channeled particle. As anticipated the most probable energy value is reduced (almost a factor two) and the spread of the distribution is smaller; in the planar channeling case, a high energy tail is present due to channeled particles with a transversal energy close to the critical value.

1.1.5.2 Channeling radiation

When an electron or a positron crosses a crystalline target misaligned with respect to the crystalline axis or planes an incoherent bremsstrahlung is emitted.

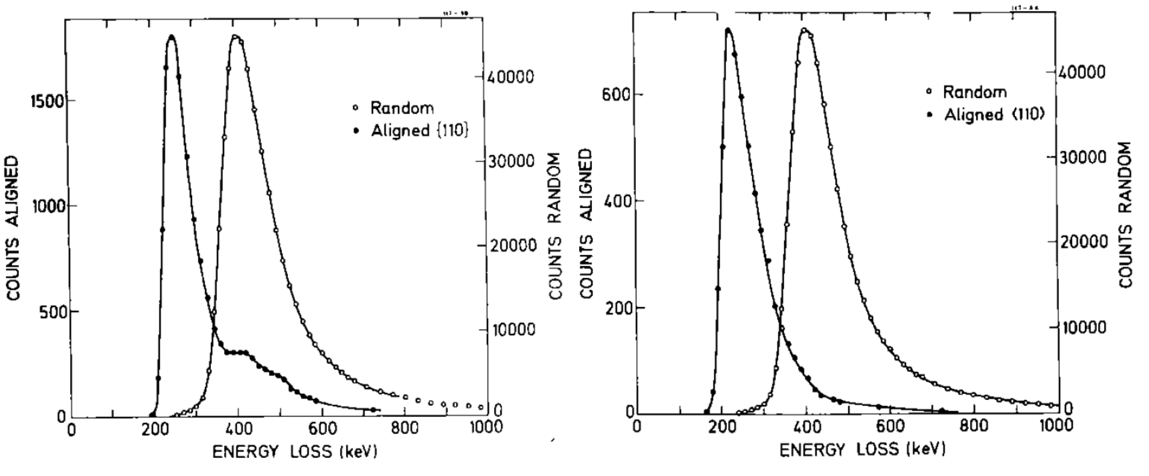

(a) (b)

Figure 1.13: Energy loss spectra in a germanium crystal: comparison between misaligned (random) particles and a) particles in planar channeling; b) particles in axial channeling.

In aligned crystals the radiation emission can be strongly enhanced through coherent emission effects which take place in the regular crystalline structure. Two kinds of intense radiation can be emitted: the coherent bremsstrahlung and the channeling radiation.

As the particle incident direction is turning towards the planar direction, the particle starts to feel the crystalline structure, and coherence in the emitted radiation results in the peak structure of the coherent bremsstrahlung [21]. The peak energies depend on the crystal geometry and on the incident angle with respect to the planes; the spectral shape is the same for positrons and electrons.

The coherent bremsstrahlung happens for angles between the crystalline direction (axis or plane) and the particle trajectory small but larger than the critical channeling angle; in other words it is emitted when the particle is not in channeling. If the angle between the incoming beam and the crystal planes goes below the critical value θ_c, particles are trapped in channeling (sec. 1.1.2). The special motion in the channel gives rise to coherence effects and the resulting radiation is called *channeling radiation*.

The structure of this radiation depends on the interplanar potential form; therefore positrons and electrons which are trapped in different potential wells produce different channeling radiation spectra. Positrons oscillate in a nearly harmonic potential (fig. 1.6) with a wavelength $\lambda = \pi d_p\sqrt{\frac{pv}{2U_0}}$ (eq. 1.34); the corresponding angular frequency is:

$$\omega_0 = 2\pi\frac{v}{\lambda} = \frac{2}{d_p}\sqrt{\frac{2U_0}{m\gamma}} \tag{1.24}$$

where the relativistic relation $pc^2 = vE$ has been used. The emitted radiation by a channeled positron is strongly enhanced in this frequency (and in the superior harmonics) apart from the Doppler effect shift:

$$\omega_\gamma = n \cdot \frac{\omega_0}{1 - \beta \cos\theta} \tag{1.25}$$

which gives rise to a peaked structure in the spectrum as shown in fig. 1.14(a) where the contribution of the first two harmonics is visible.

The electrons move in a strongly non-harmonic potential and the oscillation frequency becomes a function of the transverse energy generating a broad spectrum as shown in fig. 1.14(b).

The sensitivity to the charge sign is a peculiarity of the channeling radiation with respect to both the incoherent and coherent bremsstrahlung radiation.

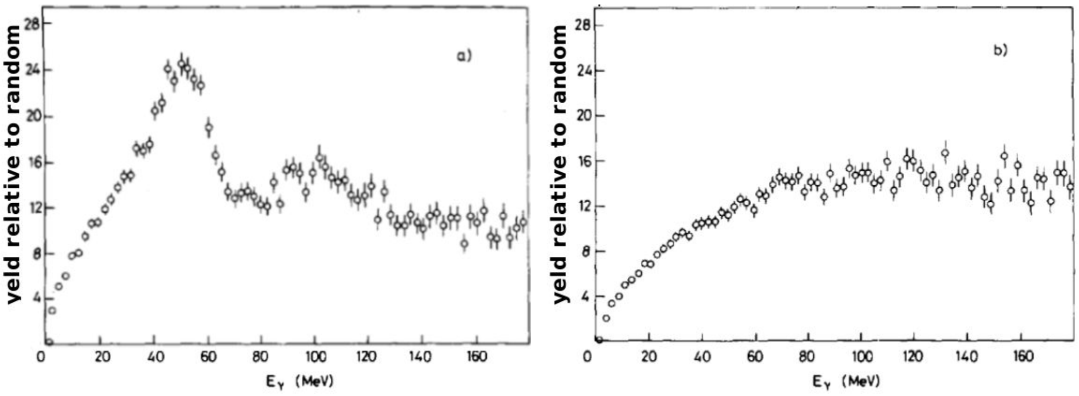

(a)

(b)

Figure 1.14: Photon energy spectra for a 10 GeV/c particle beam impinging on a silicon crystal ((110) plane, 0.1 mm thickness) normalized to the incoherent bremsstrahlung spectra: a) positron case, the peak structure relative to the first and second harmonics is clearly visibile ; b) electron case, the spectrum shows an increase with respect to the bremsstrahlung one without any relevant structures [22].

1.2 Bent crystals

In 1976 the appealing idea to steer a high energy particle beam with a bent crystal was suggested by Tsyganov [7]; he realized in fact that the bending of the crystallographic planes produces a curved channel which is able to deflect the channeled particles.

The motion of a channeled particle, in fact, is confined (in the transversal direction) by a potential well; this property can be used to deviate the particle trajectory, through a curved channel.

A curved channel can be obtained from a straight one bending a crystal with a mechanical holder as shown in fig. 1.15(b). Fig. 1.15(a) shows the scheme of a bent crystal; note that (differently from the scheme), for practical mechanical reasons, $R \gg w$ where R is the curvature radius and w is the crystal width; note that the crystal length l is independent from the radial coordinate r differently from the scheme in fig. 1.15(a). The red line represents the particle trajectory which is deviated of the angle $\theta_b = \frac{l}{R}$.

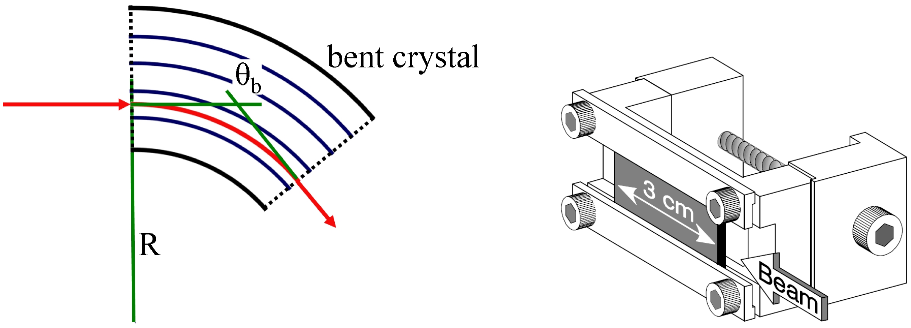

(a) (b)

Figure 1.15: a) The bent crystal working principle; b) an example of a bending device.

The curvature (R^{-1}) effect can be described by the replacement of the atomic interplanar potential with an effective one, which takes into account the centrifugal force, that lowers the interplanar potential barrier and the critical angle.

According to this, a critical curvature radius R_c, which corresponds to the maximal curvature allowing channeling, can be defined. The quantity computed in the straight crystal case can be expressed with a correction due to the curvature where $\frac{R_c}{R}$ represents the correction scale.

The interaction of particles with a bent crystal has revealed two new effects: the volume capture and the volume reflection. They both happen when an initially misaligned particle, after having performed a random motion in the crystal volume, reaches a point tangent with the channel.

In this point the particle is close to the channeling condition so that an eventual energy loss can bring it in the channeling regime; in this case, the particle is volume captured (sec. 1.2.2), otherwise it is reflected by the effective centrifugal potential (sec. 1.2.3).

1.2.1 Particle motion in a bent channel

A macroscopical curvature of the crystal (that is a curvature radius of the order of several meters) has a negligibile effect on the microscopical crystalline structure of the crystal (Angstrom scale) itself. This implies that the continuous interplanar potential computed in sec. 1.1.1 remains unchanged; however a particle trapped in the channel feels a centrifugal force as well as the planar potential. Fig 1.16 describes the particle interaction in the channel both in the laboratory inertial frame (plot a) and in the non inertial frame in which the longitudinal direction (z in the plot) follows the channel orientation (plot b).

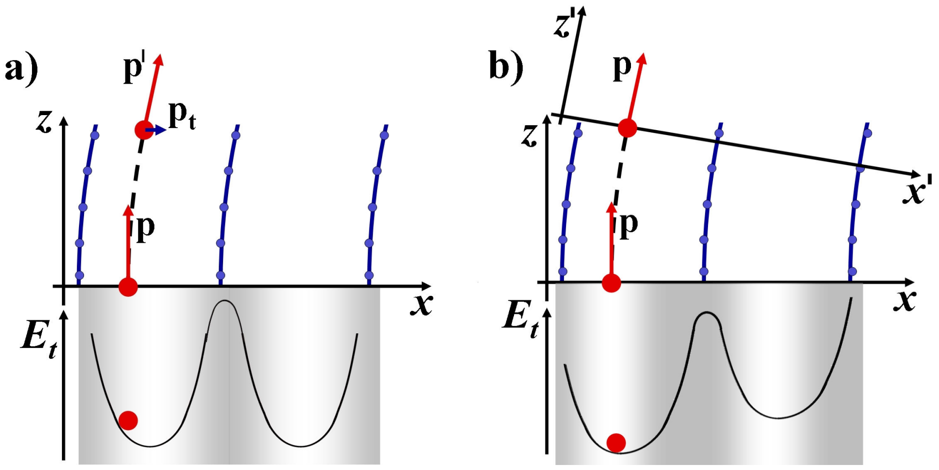

Figure 1.16: Scheme of the channeling motion of a particle which enters a bent crystal aligned with its planes described: a) in the laboratory inertial frame in which the particle assumes an angle with respect to the planes which are curved; this implies that its equilibrium position in the potential is no more in the channel center; b) in the non inertial frame which rotates with the particle; the centrifugal force appears and modifies the interplanar potential.

In the first case, although the particle approaches the channel aligned with respect to the crystal planes ($p_t = 0$), to follow the channel curvature its momentum has to acquire a transversal component; so the interplanar potential applies a force which modifies the particle momentum. This implies that the particle equilibrium point in the channel must be external with respect to the minimum of the interplanar potential (where the force applied to the particle by the potential vanishes). In the non inertial system the particle momentum direction doesn't change, but a centrifugal force directed towards the external side of the channel appears. The contribution of this force should be added to eq. 1.13 which expresses the equilibrium of the forces applied on the particle:

$$pv\frac{\mathrm{d}^2x}{\mathrm{d}z^2}+U^{'}(x)+\frac{pv}{R(z)}=0 \tag{1.26}$$

where $R(z)$ is the curvature radius as a function of the position in the channel; if it is independent from the position ($R(z)=R$) the crystal curvature is an arc of circumference and the effective interplanar potential $U_{eff}(x)$ has the following analytical form:

$$U_{eff}(x)=U(x)+\frac{pv}{R}x \tag{1.27}$$

The expressions given in sec. 1.1.2 which describe the particles motion for an arbitrary interplanar potential $U(x)$ remain valid with the substitution with $U_{eff}(x)$. It is interesting to note that the correction to the potential is a term of the form pv/R so at different energies if the ratio pv/R doesn't change, the corrections to the motion due to the crystal bending are the same.

According to eq. 1.27, as the curvature ($1/R$) increases, the minimum of the potential is shifted towards the outer planes and the potential well depth is reduced on the outer planes side, as shown in fig. 1.17 where the interplanar potential is plotted for 3 different curvature radii.

In other words the centrifugal force pushes the particles towards the atomic plane as the curvature increases so there must exist a critical curvature beyond which the scattering probability with nuclei grows so much that channeling is no longer possible. This happens when the centrifugal force equals the electric field produced by the atomic plane at the critical distance $x_c=d_p/2-a_{TF}$ which can be considered the channel border:

$$\frac{pv}{R_c}=U'(x_c) \tag{1.28}$$

R_c is defined as the critical curvature radius (Tsyganov critical radius) below which channeling is no longer possible for a particle of momentum p. According to the Lindhard potential expression given in eq. 1.4, an approximate expression of R_c can be computed:

$$R_c=\frac{pv}{U'(x_c)}\simeq\frac{pv}{\pi N d_p Z_i Z e^2} \tag{1.29}$$

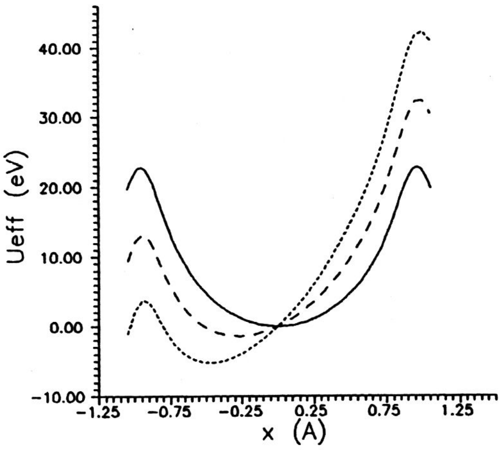

Figure 1.17: The interplanar silicon ((110) planes) potential computed in the Molíer approximation for: the straight crystal (solid line), a pv/R of 1 GeV/cm (dashed line) and 2 GeV/cm (dotted line).

In deriving this expression, the contribution of the single plane is taken into account; in fact the x_c position is so close to an atomic plane, that the contribution to the potential from the other planes is negligible. Since in silicon $U'(x_c) \simeq$ 5 GeV/cm, the critical curvature radius for relativistic particles of energy E ($pv \simeq E$) is approximately $R_c^b = \frac{E[\text{GeV}]}{5}$ cm.

The shape of the effective potential well (fig. 1.17) shows a decrease of the potential barrier in the external direction with respect to the crystal bending, as the ratio pv/R increases. Indeed the maximum transversal energy value for a fixed momentum particle decreases with the curvature and if U_0 is the transversal energy limit to be channeled in a straight crystal, when the same crystal is bent the maximum transversal energy will assume a new value $U_0^b < U_0$. This also affects the critical angle (given in eq. 1.11) which becomes $\theta_c^b = \sqrt{\frac{2U_0^b}{pv}} < \theta_c$. An approximated value of U_0^b as a function of the curvature radius can be computed taking into account the harmonical approximation according to which the effective potential of eq. 1.27 becomes:

$$U_{eff}(x) = U_0 \cdot \left(\frac{x}{x_c}\right)^2 + \frac{pv}{R}x \tag{1.30}$$

As shown in sec. 1.1.1, the real interplanar potential is defined to have its minimum in the middle of two atomic planes and to reach its maximum U_0 in the critical positions $-x_c$, x_c. Eq. 1.30 shows that if $U(x)$ is harmonic, $U_{eff}(x)$ is harmonic too; the effect of the centrifugal term is to shift its minimum in the (U_{eff}, x) plane, so that its coordinate becomes $x_{min} = -\frac{pvx_c^2}{2RU_0}$; the height of the potential barrier will then be:

$$U_0^b = U_{eff}(x_c) - U_{eff}(x_{min}) = U_0 - \frac{pv}{R}x_c + \frac{1}{2U_0}\left(\frac{pv}{R}x_c\right)^2 \tag{1.31}$$

According to eq. 1.29 the critical radius in the harmonic approximation is $R_c^h = \frac{pvx_c}{2U_0}$ so the potential barrier can be expressed as:

$$U_0^b = U_0\left(1 - 2\frac{R_c^h}{R} + \left(\frac{R_c^h}{R}\right)^2\right) = U_0\left(1 - \frac{R_c^h}{R}\right)^2 \tag{1.32}$$

For a curvature radius tending to infinity, which means in a straight crystal, $U_0^b = U_0$; if the curvature radius increases, U_0^b decreases as it is expected (note that only the region $R > R_c^h$ is considered). Thus if θ_c is the critical angle of a straight crystal, when the crystal is bent with a $1/R$ curvature, it becomes

$$\theta_c^b = \theta_c\left(1 - \frac{R_c^b}{R}\right) \tag{1.33}$$

It was pointed out that the effective potential in a bent crystal is still harmonic, so the particle trajectories in the channel have the same shape of the ones in a straight crystal (eq. 1.14):

$$x = -x_c\frac{R_c}{R} + x_c\sqrt{\frac{E_t}{U_0^b}}\sin\left(\frac{2\pi \cdot z}{\lambda} + \phi\right) \tag{1.34}$$

In fact, they have the same period λ but the oscillation takes place around a new equilibrium point, $x_{min} = -x_c R_c/R$.

The equilibrium point displacement of the channeling oscillation corresponds to a change of the particle distribution in the channel: the channeled particles are shifted towards the atomic plane because of the centrifugal force so they experience a greater electron density with respect to the straight crystal. This should increase the dechanneling probability (sec. 1.1.3) but, as the valence electrons in silicon and germanium have a roughly uniform distribution in the channel, the electron scattering probability of a channeled particle is almost insensitive to the crystal curvature for curvature radii $R \geq 2R_c$. Indeed this effect is hidden by the greater influence on the dechanneling yield caused by the reduction of the maximum transversal energy. This implies that also with the same scattering probability in a curved crystal the possibility to overcome the potential barrier increases;

it can be shown that the dechanneling length is proportional to the maximum transversal energy [9], so if L_D is the dechanneling length in a straight crystal, when the crystal is bent it becomes:

$$L_D^b = L_D\left(1 - \frac{R_c^h}{R}\right)^2 \tag{1.35}$$

In addition, the dechanneling length in a crystal with a given curvature is no more a linear function of the particle pv as shown is sec. 1.1.3: in the effective potential the curvature radius R always appears in the fraction $\frac{pv}{R}$; the critical radius has been defined for a fixed particle energy but in the same way, once the curvature radius is fixed, a critical particle energy pv_c can be defined. Eq. 1.35 becomes:

$$L_D^b = L_D\left(1 - \frac{pv}{pv_c}\right)^2 \propto pv\left(1 - \frac{pv}{pv_c}\right)^2 \tag{1.36}$$

The dechanneling length in a bent crystal is no more a monotonic function of the energy but has a maximum value in $pv = 1/3 \cdot pv_c$ which is the optimal choice to minimize the dechanneling losses in a bent crystal.

1.2.2 Volume capture

A particle which enters the crystal is channeled if its transversal energy doesn't overcome the potential barriers created by the crystal planes; if the scattering effects are neglected, the transversal energy is a conserved quantity and the particle follows the channel. In sec. 1.1.3 it has been pointed out that the scattering effects gradually modify the transversal energy giving to the channeled particle a finite probability to exit the channel, a phenomenon called dechanneling. For any given particle trajectory in the crystal the reverse one is possible (Lindhard reversibility rules [4]), meaning that a reverse dechanneling mechanism should exist: a particle with a transversal energy above the critical value can lose part of the energy because of multiple scattering, and be captured in the channel; this phenomenon is called *feed in* or *volume capture* in the bent crystal frame.

In a crystal, the dynamics of the two beam populations, the channeled particles and the random ones (in amorphous condition), is determined by the two opposite mechanisms (dechanneling and feed in), so that the effective dechanneling can be defined as the total fraction of particles which leave the channel. In Fig. 1.18(a) a possible particle trajectory in a straight crystal is shown: at the beginning the particle momentum is parallel to the channel so the particle is trapped in the channel itself; during the confined motion the particle experiences a series of electron collisions which finally allow it to overcome the planar potential barrier (*dechanneling*); once free, the particle moves randomly changing its angle with respect to the channel because of multiple scattering; at a certain point the particle is re-captured in a channel (*feed-in*).

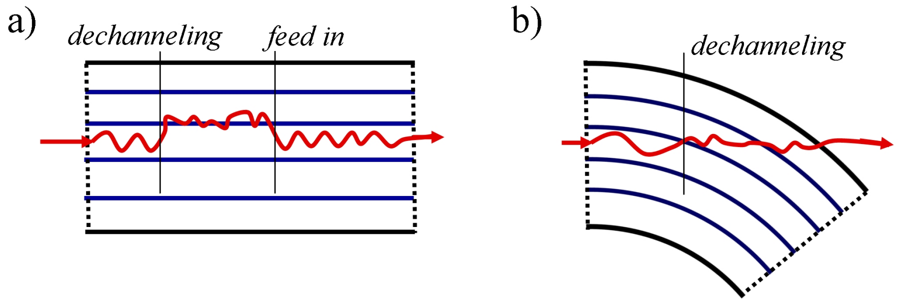

Figure 1.18: a) A possible particle trajectory in a straight crystal: the particle is first dechanneled and subsequently re-channeled (feed-in); b) a similar trajectory in a bent crystal: after the dechanneling the feed-in probability rapidly decreases as the particle is no more aligned with the channel.

The equivalent process in a bent crystal is shown in fig. 1.18(b); in this case once the particle has left the channel it performs a random motion in the crystal but differently from the straight crystal case the channel rotates its direction as the particle moves forward in the crystal itself. If δz is the particle longitudinal displacement in the crystal, the angle between the particle and the channel is $\theta \simeq \frac{\delta z}{R}$ (where the curvature radius is assumed to be greater than the crystal length, $R \gg l_c$). When the particle path is greater than $R\theta_c$ the angle between its trajectory and the channel direction is greater than the critical angle θ_c so the particle is misaligned with respect to the planar potential and cannot be channeled. According to this the re-channeling after dechanneling in a bent crystal is improbable (the feed-in is a negligible correction in the effective dechanneling computation).

Fig. 1.18 shows two examples of trajectories in which the particle enters the crystal in channeling condition but it is also possible that a particle enters the crystal in a random condition and then is captured in the channel. In this case, in the straight crystal the capture can happen along the whole crystal length while in the bent one the particle can be captured only when its trajectory is nearly tangent to the channel, that is when the angle between the particle and the channel is $\theta < \theta_c$. Differently from the straight crystal case in a bent crystal the quasi tangent condition can be reached also for impact angles larger than the critical angle as long as the impact angle stays smaller than the crystal bending angle ($\theta < \theta_b$). As shown in fig. 1.19(a) when θ increases, the tangent condition moves within the crystal volume, which is the reason why the corresponding capture process is called *volume capture*.

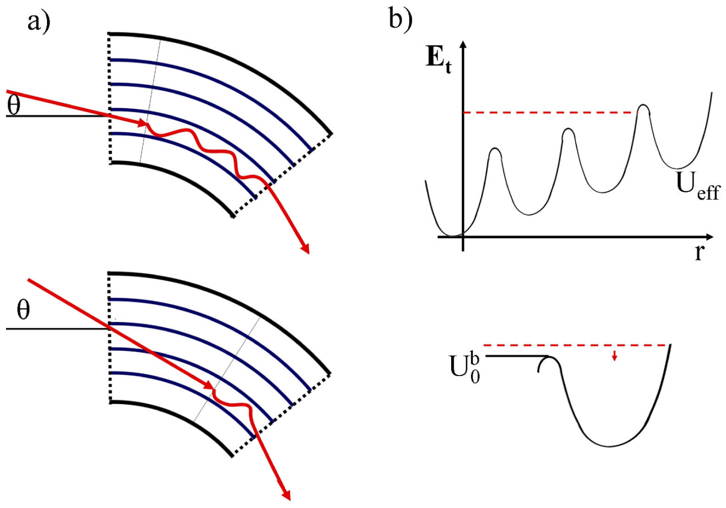

Figure 1.19: a) Two schematic examples of volume captured particles in a bent crystal: as the misalignment increases (from top to bottom) the volume capture point moves farther on inside the volume. b) Trajectory of a volume captured particle represented in the phase space (transversal energy versus radial position); in the zoom (bottom plot) note that the particle reaches a quasi-channeling condition.

Fig. 1.19(b) shows the particle trajectory represented in fig. 1.19(a) (top) in the (E_t, r) phase space: the particle transversal energy E_t (dashed line) is plotted as a function of the radial coordinate; the curve represents the effective potential (which is the sum of the interplanar crystal electric field and the centrifugal force). The transversal energy is a motion constant (sec. 1.1.2) so it is represented by a constant line as a function of the particle displacement in the r direction; moreover E_t is the sum of a kinetic term and a potential one as shown in sec. 1.1.2:

$$E_t = pv\theta^2 + U_{eff}(r) \tag{1.37}$$

Since $U_{eff}(r)$ increases with r due to the centrifugal force, the E_t kinetic contribution ($pv\theta^2$) should decrease; pv is constant so θ decreases. This represents (in the non inertial frame which rotates with the channel) the progressive particle alignment with respect to the channel.

At a certain radial coordinate $r = r_t$ the potential $U_{eff}(r_t)$ equals the transversal energy E_t so that the particle is aligned with the channel ($\theta = 0$). Note (zoom of fig. 1.19(b)) that in the r_t position the particle potential energy is higher than the external potential barrier and so the particle cannot be contained in the channel (this is the origin of the effect called *volume reflection* treated in sec. 1.2.3).

Although the particle is not in channeling, its transversal energy slightly overcomes the maximum transversal energy value (U_0^b); in this condition the particle is in quasi-channeling as a small transversal energy decrease, due to scattering, is enough to bring the particle in channeling. In this case the particle is *volume captured*.

The volume capture is strictly related to dechanneling because both depend on the scattering probability. The variation of the number (n_c) of channeled particles due to dechanneling is given by the following differential equation which leads to the exponential trend given in sec. 1.1.3:

$$\frac{\mathrm{d}n_c}{\mathrm{d}z} = -\frac{n_c}{L_D} \tag{1.38}$$

where dz is the infinitesimal increment in the longitudinal direction and L_D is the dechanneling length (eq. 1.16); adding the feed-in contribution, eq. 1.38 becomes:

$$\frac{\mathrm{d}n_c}{\mathrm{d}z} = -\frac{n_c}{L_D} + \frac{n_{qc}}{L_F} \tag{1.39}$$

where n_{qc} is the number of quasi-channeled particles and L_F is the feed-in length, which due to the reversibility rule is $L_F = L_D$. In this situation the particles incoming angle is greater than the critical angle so at the beginning no particles are channeled; according to this in eq. 1.39 $n_c = 0$ and so:

$$\frac{\mathrm{d}n_c}{\mathrm{d}z} = \frac{n_{qc}}{L_D} \tag{1.40}$$

It was pointed out that the longitudinal distance along which the particles are aligned to the channel ($\theta < \theta_c$) is $\delta z = \theta_c R$ so since $\delta z \ll L_D$ the number of captured particles is approximately:

$$\delta n_c \simeq n_{qc}\frac{L_D}{\delta z} = n_{qc}\frac{L_D}{R\theta_c} \tag{1.41}$$

meaning a volume capture probability:

$$P_{vc} = \frac{\delta n_c}{n_{qc}} \simeq \frac{R\theta_c}{L_D} \tag{1.42}$$

Considering the trajectories reversibility in the crystal, a more rigorous formula for P_{vc} can be derived [9], introducing a numerical correction factor:

$$P_{vc} = \frac{\pi}{2}\frac{R\theta_c}{L_D} \tag{1.43}$$

The volume capture trend as a function of the beam energy can be computed, considering that $\theta_c \propto \sqrt{pv}$ and $L_D \propto pv$ (if the logarithmic correction is neglected):

$$P_{vc} \propto \frac{R}{(pv)^{3/2}} \tag{1.44}$$

1.2.3 Volume reflection

The *volume reflection* represents the particle deviation in a single point inside the crystal due to an elastic scattering with the atomic potential barrier; it was considered for the first time in computer simulations [23] and recently observed [24]. In this section the volume reflection mechanism will be discussed pointing out its great interest in high energy physics applications due to its great efficiency and angular acceptance.

When a particle enters the crystal with an angle larger than the critical one (θ_c), its transversal energy overcomes the potential barrier and the particle cannot be channeled. According to this, it crosses the crystal as an amorphous material and during this motion the angle between the particle and the crystal planes decreases due to the crystal curvature (fig. 1.20(a)). The same phenomenon can be described, in the non inertial reference system which follows the channel direction, as an increase of the effective potential felt by the particle (fig. 1.20(b)). The particle transversal energy E_t, in fact, is a conserved quantity given by the sum of a kinetic part ($pv\theta^2$), a potential one (U_{eff}) and an offset which depends on the particle entrance point in the crystal and can be set to zero, so that to an increase of the effective potential a decrease of the angle θ should correspond. At a certain point the potential U_{eff} equals the particle transversal kinetic energy, so that $\theta = 0$ meaning that the particle is tangent to the crystal planes. At this point the particle starts to fall in the potential well increasing its transversal energy in the opposite direction: in other words, the particle has been reflected.

It is useful to analyze the situation in the inertial frame to have a better comprehension of what is happening and to compute the reflection angle. Let's consider the case of a particle which starts and ends its motion in the center of a channel: when the particle enters the crystal its transversal energy makes it overcome the potential barrier of the different channels but as the crystal is bent the barriers become more and more parallel to the particle momentum and at a certain point a barrier will stop the particle motion towards the center of the crystal. In this point the barrier breaks the particle motion towards its direction (in other words, it has deviated the particle), which, according to the energy conservation, means that the potential energy of the barrier $U(r_t)$ should be subtracted from the particle kinetic energy in the transversal direction. Therefore the particle is deviated of an angle

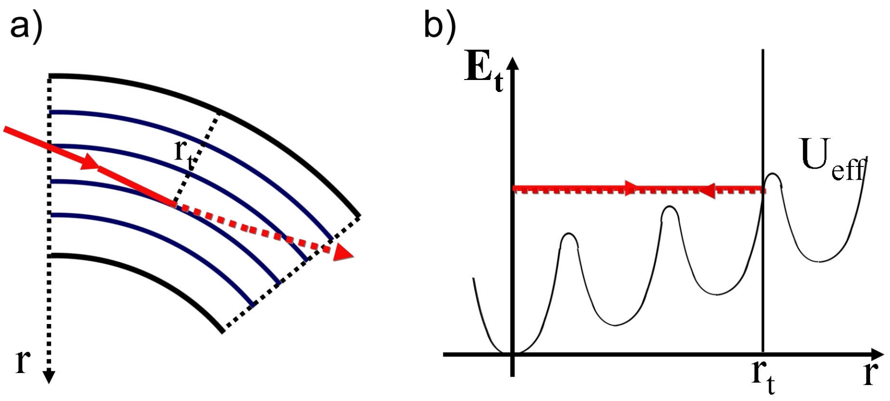

Figure 1.20: Reflection of a charged particle in the crystal volume at the turning radial coordinate r_t: a) schematic view of the crystal; b) phase space of the particle transversal energy as a function of the radial coordinate.

$\delta\theta = \sqrt{\frac{2U(r_t)}{pv}}$. After being stopped, the particle is on the top of the potential barrier from where it is pushed towards the channel center (it falls in the potential well); the potential energy $U(r_t)$ is converted in kinetic energy which means the particle assumes another angular kick $\delta\theta = \sqrt{\frac{2U(r_t)}{pv}}$.

The reflection has been described in two steps: first the particle is stopped by the barrier (it assumes a $\delta\theta$ kick) and then it is accelerated in the opposite direction (it assumes another $\delta\theta$ kick). As in the case of the elastic scattering of a ball on a wall, the total deflection angle shoud be $2\delta\theta$:

$$\theta_r = 2\sqrt{\frac{2U(r_t)}{pv}} \tag{1.45}$$

The plot of fig. 1.20(b) shows that after being reflected the particle transversal energy is too large for the particle to be trapped in channeling so the particle exits from the crystal in the direction assumed after the reflection.

To compute θ_r the value of $U(r_t)$ is needed; $U(r)$ is the crystal interplanar periodic potential whose period is the distance between the crystal planes (d_p); so $U(r+nd_p) = U(r)$. If $r_t = nd_p + x$ where x is defined as the distance between the reflection point and the nearest channel center, $\theta_r = 2\sqrt{\frac{2U(x)}{pv}}$. This is schematically shown in fig. 1.21(a) where x_b is defined as the low coordinate of the reflecting potential so that the possible x values are between x_b and $d_p/2$.

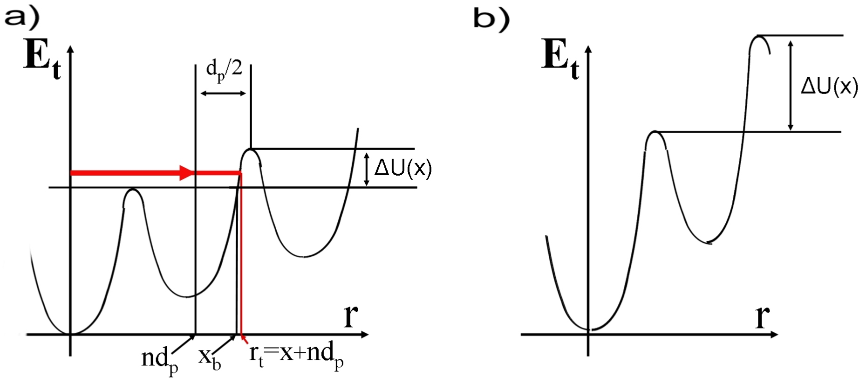

Figure 1.21: a) Schematic of the effective potential at the turning point; b) effective potential of smaller radius (compared with the one in (a)): the reflecting area $\Delta U_{eff}(x)$ increases.

Let's assume a large bending radius ($R \gg R_c$); the effective potential has a small component due to the centrifugal force (pv/R) so the x_b value will be close to $d_p/2$ so that $x \simeq d_p/2$ and consequently the volume reflection angle can be approximated:

$$\theta_r \simeq 2\sqrt{\frac{2U(d_p/2)}{pv}} = 2\theta_c \tag{1.46}$$

This approximation takes into account the limit $R \rightarrow \infty$ which clearly does not allow the reflection so that the maximum reachable θ_r value is just below $2\theta_c$. Note that although different particles can be reflected in different turning points depending on their initial transversal energy, they will have almost the same reflection angle because the x value is almost fixed. But when the curvature radius decreases the reflection region ($x_b < x < d_p$) of the potential barrier increases (fig. 1.21(b)) and the reflection angle being a function of x will assume a larger distribution of values as shown by the simulation in fig. 1.22. The conclusion is that increasing the crystal curvature the reflection angle distribution spread increases too while its mean value decreases.

The angular distributions shown in fig. 1.22 are strongly asymmetric but they do not take into account that before and after the volume reflection, particles cross the crystal as an amorphous layer being subject to multiple scattering whose contribution smooths the distributions, strongly reducing their asymmetry as shown in fig. 1.23(a). In fig 1.23(b) the same angular distribution is plotted in a wider

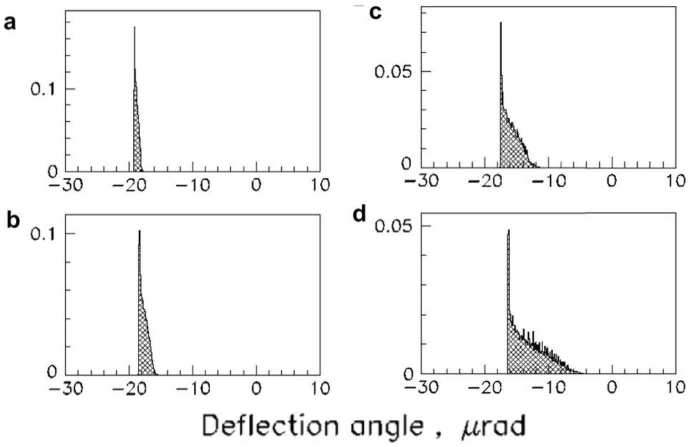

Figure 1.22: Simulated angular distributions of 400 GeV protons scattered by a (110) silicon crystal bent with different curvature radii: a) 40 m; b) 20 m; c) 10 m; d) 5 m (the critical radius R_c is ~ 0.8 m) [25].

angular range showing its tail in the crystal bending direction, where two peaks appear in correspondence to the bent planes direction. They are composed of the particles captured into the channeling regime during the reflection (volume capture, sec. 1.2.2).

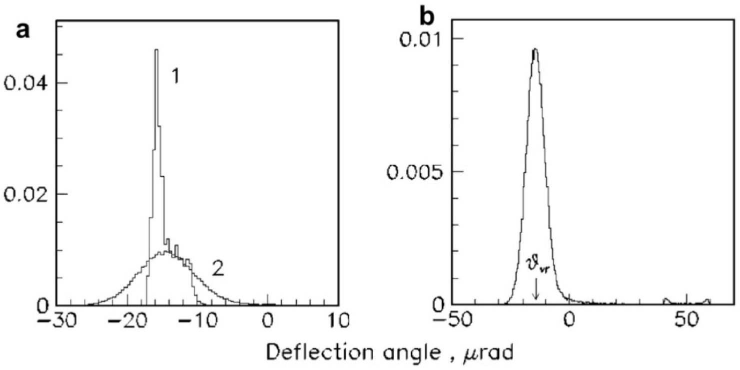

Figure 1.23: Simulated angular distributions of 400 GeV protons scattered by a (110) silicon crystal (curvature radius 10 m): plot 1 without the multiple scattering contribution; plot 2 taking it into account; b) the same plot in a larger horizontal (angular) scale; the right tail of the distribution shows the volume captured particles.

Eq. 1.46 gives the volume reflection angle under two conditions: 1) $R \gg R_c$;

2) the particle enters and leaves the crystal in the center of the channel. They both favour a large reflection angle; a more precise estimation of the volume reflection angle is 1.5 θ_c rather than 2 θ_c. A complete discussion can be found in [25] (based on Montecarlo simulation) and in [26] (based on analytical calculation).

The dependence of the reflection angle on the bending radius has been discussed briefly: a smaller bending radius, increasing the crystal curvature allows the reflection in crystal lattice points in which the interplanar potential is less intense so smaller reflection angles become possible and the average deflection angle decreases.

Also the entrance and the exit point coordinate in the channel change the volume reflection angle; eq. 1.46 is based on the assumption that the particle enters and exits the channel in points where the interplanar potential has a minimum and is subject to a reflection where it has a maximum. Let's suppose that the particle enters and exits the crystal in points where the interplanar potential has a maximum; in the computation of its transversal energy change the initial and final contribution should be subtracted. In fact, even though the reflection angle does not vanish at the beginning and at the end of the crystal, the particle is misaligned with respect to the channel so the potential contribution to the particle transversal energy is small if compared to the one of the reflection point.

The volume reflection, as well as channeling is able to deflect charged particles, even though, after its discovery in Montecarlo simulations, it has not been considered as an alternative to channeling for beam steering. The reason is that its deflection angle is fixed and small, if compared to the channeling one. For example, even at a relative high energy ($\sim$100 GeV) with a relative short crystal ($\sim$ 2 mm) the reflection angle is of the same order of magnitude of the multiple scattering.

In spite of this, there are some factors that make the volume reflection study interesting for this application:

- the channeling angular acceptance is fixed (θ_c) which could be a problem with a beam with a divergence $\theta \gg \theta_c$ because the deflection efficiency will be limited. On the other side, the volume reflection acceptance (which is the crystal bending angle) is larger and can be adjusted depending on the situation;

- at very high energy the scaling properties favour volume reflection ($\theta_c \propto E^{-\frac{1}{2}}$) with respect to multiple scattering ($\theta_{ms} \propto E^{-1}$) and channeling ($\theta_c \propto \dfrac{1}{R_c} \propto E^{-1}$);

- volume reflection is characterized by a high efficiency; the simulation shows that all the non-volume captured particles are reflected; since the volume

> capture probability scales as $E^{-\frac{2}{3}}$ very high efficiencies (close to 100%) are expected at high energy.

The first volume reflection observation [27] was performed at the IHEP laboratory in Protvino (Russia) on the U-70 accelerator with a 70 GeV/c proton beam. The silicon crystal was prepared and bent using the elastic quasimosaicity effect [28] (see sec. 3.1.4.2) which allows to reach a very small thickness in the beam direction; the crystal was 0.72 mm (along the beam) with an area of 20×60 mm^2; the bending angle was 423 μrad.

The rms of the beam divergence (in the bending plane) was 15 μrad, the average multiple scattering value for a 70 GeV proton crossing the crystal was 13.5 μrad while the critical angle for the used (111) silicon crystal was 24 μrad. In this condition if the crystal is properly oriented the volume reflection should overcome both the beam spread and the multiple scattering of the crystal being easily detectable.

Fig. 1.24 shows the experimental setup. In addition to the quasimosaic curvature (used for channeling) the crystal has also an anticlastic curvature which changes the channel orientation as a function of the x position on the crystal surface, so a part of the crystal can be aligned for channeling while another part for volume reflection and another one can be misaligned at the same time (this is schematically shown in fig. 1.25(a)). The correct orientation of the crystal is identified by the S2 and S3 scintillators (fig. 1.24) whose counting rate increases when the crystal is in channeling.

The beam profile after the crystal is measured by two emulsion plates located at 4.6 m and 5.9 m from the crystal itself. The intensity profile recorded by the first plate is shown in fig. 1.25(b); three different regions can be identified marked with the letters A (primary beam overlapped to the reflected one), B (beam absence), C (channeled beam). They are explained in fig. 1.25(a).

The analysis of the recorded profile on both the plates gives a volume reflection angle of $\theta_r = 39.5 \pm 2.0$ μrad which expressed in terms of the crytical angle becomes $\theta_r = (1.65 \pm 0.08) \cdot \theta_c$ compatible with the simulation prediction [27].

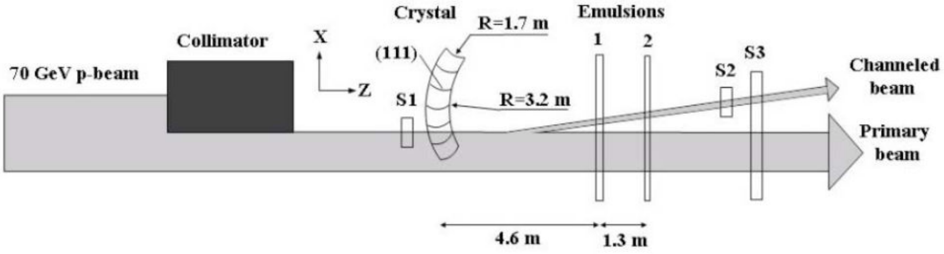

Figure 1.24: Layout of the experimental setup.

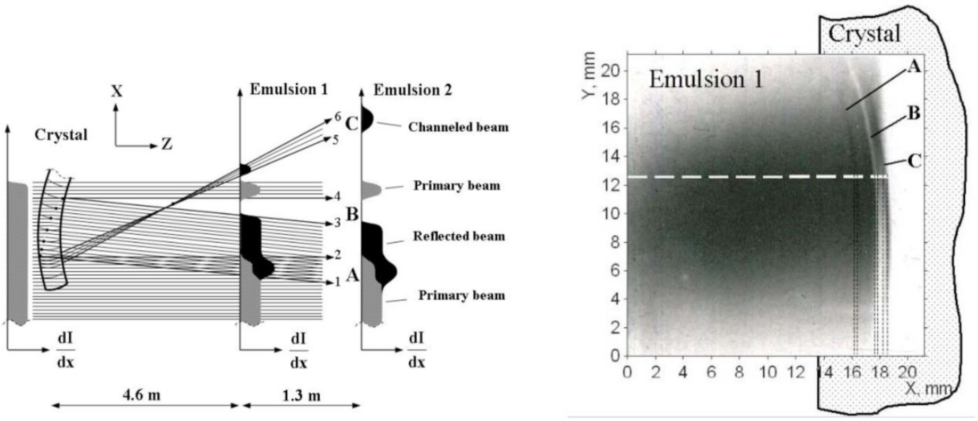

(a) (b)

Figure 1.25: a) Schematic view of the horizontal trajectories crossing the crystal and the emulsion; b) a part of the first emulsion crossed by the beam: the crystal shape and the interesting vertical lines are represented.

Chapter 2

A channeling application: the beam collimation

The field of application of bent crystals in high energy particle physics is really wide. Following Tsyganov's idea, bent crystals have been transformed into efficient instruments for particle steering at accelerators; their behaviour is predictable and reliable: in many cases they have been used with beam of high intensity over years.

One of the most studied applications is the crystal assisted extraction [29] which is characterized by many benefits if compared to the standard resonant one [30]. It also represents a possible solution for particle extraction from a very high energy beam such as the LHC one [31]. Other applications can be found in external beamlines where bent crystals are used to focus [32] or split [33] the beam. Last but not least, crystal undulators [34] are under study to produce high intensity photon beams and bent crystals to measure the magnetic moments of shortlived particles [35].

Among the various applications, in 1991 it was proposed to use bent crystals for halo collimation in SSC [36]. The basic idea was that a bent crystal used as a primary collimator should extract the incident halo particles directing them onto a secondary collimator. Although the SSC accelerator has been never built, the necessity of an efficient and robust collimation system in hadron colliders has kept the interest in the crystal collimation alive. Experiments were performed at the Tevatron and RHIC accelerators during the past few years and the present studies are addressed to develop a collimation system, which could allow LHC to reach its nominal luminosity.

This thesis work has been developed in this research context and the aim of this chapter is to give an overview on the crystal-based collimation without the presumption to give any final feasibility judgements but showing the difficulties and the potentialities of this innovative system.

2.1 Beam collimation

The collimation system is an essential apparatus in a particle accelerator: its role is to reduce the beam halo which is the external beam region, populated by particles which are leaving the nominal accelerator orbit because of phenomena connected to the beam dynamics, such as: the scattering on the residual gas particles of the vacuum system; the beam-beam interaction which takes place in colliders, where two oppositely directed rotating beams are brought into collision, and where the particles in one beam are influenced by the non linearity forces of the other beam; the non linearity field errors which cannot be avoided in the superconducting magnets in which the field types (dipole, quadrupole, etc.) have to be produced according to the coil geometry. The beam losses are becoming an increasing concern for modern accelerators causing equipment damage, residual radiation and large experimental backgrounds [37].

A collimation system is usually composed of a complex of cleaning insertions in the accelerator line, in which targets of amorphous material are positioned on the beam halo next to the beam core, to absorb the unwanted particles. In modern hadron accelerators such as LHC or the Tevatron, the high energy particles stored in the beam require the implementation of a multi-stage collimation system: a first collimator stage intercepts the primary halo beam and generates a secondary halo composed of particles with a larger misalignment with respect to the nominal beam trajectory; most of this secondary halo is then stopped by the secondary collimators which are bulk absorbers; scattering within such collimators causes a tertiary halo beam that must be intercepted by a third series of collimators.

In the LHC and Tevatron accelerators which are characterized by the use of superconducting magnets, the collimation besides the important role of minimizing the halo-induced background in the particle physics experiments is crucial to prevent the beam induced quenches of the magnets themselves. Due to the high beam energy stored, in fact, a relative small number of particles which leave the nominal beam trajectory and eventually penetrate the superconducting magnets can deposit enough energy to warm the magnets causing their quenching.

In other words the cleaning efficiency of the collimation system can represent a limit for the accelerator luminosity; this justifies the efforts in improving the collimation techniques. In this context the idea of using a bent crystal as a primary collimator was born [38].

The role of the primary collimator is to give a substantial angular kick to the incoming particle in order to increase the impact parameter on the secondary collimator, which is generally placed in the optimum position to intercept the transverse or longitudinal beam halo. The primary collimator is usually an amorphous target which scatters the impinging particles in all directions with a wide angular spread. A bent crystal used for primary collimation has the amazing property of kicking all the particles in the same direction (that can be chosen to be the radial one) and with a small angular spread; in this way the extracted, unwanted, particles will intercept the center of the absorber excluding any particles losses.

The large range of scattering angles from an amorphous primary collimator makes the optimization of the location of the secondary collimator a difficult task and limits the achievable collimation efficiency. If the primary collimator is replaced with a bent crystal, it will be possible to deflect halo particles away from the beam core. The secondary collimator can be efficiently placed to intercept the channeled beam. If the bent crystal has a high channeling efficiency, the efficiency of the collimation system can be greatly improved with respect to a conventional two stage collimation system. The performance of such a collimator clearly depends on the crystal deflection efficiency; for this reason the studies and experiments on crystal collimation are addressed to increase and measure this efficiency.

As it is pointed out in chap. 1, a bent crystal can steer a particle beam at least with two deeply different effects, channeling and volume reflection. The first crystal collimation ideas were focused on the channeling effect to deviate the particle halo into the absorber and the development of these ideas, as it will be described (sec. 2.2), has brought great improvements reaching global deflection efficiencies of 85% [30]. During these studies the development of the crystal channeling experiments revealed the first evidence of the volume reflection, whose properties (large efficiency and angular acceptance) makes it a good candidate for the collimation of high energy particle beams. This thesis work describes the first experiments addressed to explore the volume reflection properties with the aim of designing a collimation system for LHC.

2.2 The history of crystal collimation

The feasibility of crystal channeling collimation is strictly linked to a high channeling efficiency. In the first experiment with bent crystals (1979 FNAL [7]) the deflected beam fraction was only 1% but already in the next experiments it was improved. An important milestone of this evolution is represented by the experiments performed at the CERN SPS [39] in which protons diffusing from a 120 GeV beam were extracted with a bent silicon crystal with an efficiency of 10-20%. This extraction study clarified several aspects of the extraction technique proving that the multipass extraction mechanism plays an important role as far as the final extraction efficiency is concerned; fig. 2.1 shows the extraction efficiencies measured at the SPS experiment compared with the simulation.

The multipass effect takes place in a circular accelerator where the particles stay on similar orbits for many turns. When a crystal is put on the circulating beam (on the beam halo) with the correct orientation for channeling and a particle

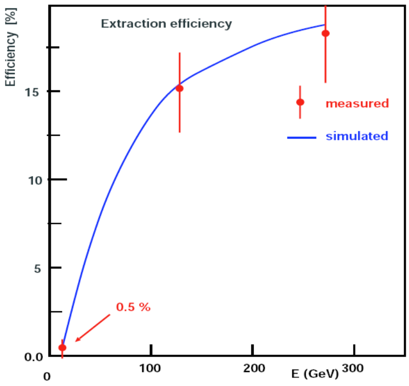

Figure 2.1: Extraction efficiency measured in the SPS experiment as a function of the beam momentum [39].

crosses it without being channeled, after a turn the particle has a new opportunity to be channeled and so on. This mechanism increases the channeling efficiency in circular accelerators; it was demonstrated [40] that the reduction of the crystal size in the beam direction increases the average number of crossings of the particles, which largely enhances the channeling efficiency. This happens because the non channeled particles behave in the crystal as in an amorphous material being scattered of an average angle which is proportional to the square root of the crystal length; so in a shorter crystal the non channeled particles present in average a smaller deflection with respect to the nominal beam trajectory. Hence, in the various crossings of the crystal they will have a smaller probability to exceed the channeling angle acceptance, that is to be misaligned beyond the critical angle.

In order to clarify the different effects of the multipass mechanism and to verify its performance comparing it with the Montecarlo simulation prediction, an experiment involving the test of very short crystals was started at IHEP at the end of 1997 [41].

2.2.1 The IHEP experiments

The Institute for High Energy Physics (IHEP) in Protvino, near Moscow, has many locations on the U-70 synchrotron ring where crystals are installed for extraction and collimation studies [29]. Two of these locations are dedicated to the crystal collimation experiment. The collimation experiments and the extraction ones have many common features; in fact, in both cases a bent crystal is put on the circulating beam to deviate the incoming particle, in the extraction experiments, to an external beamline and in the collimation ones to an absorber (secondary collimator). In any case the deflection efficiency as a function of the crystal features is the key measured parameter. For this reason it is usual to find data from experiments in the extraction configuration mixed with the ones obtained in a collimation setup. Fig. 2.2 is an example of this mixture; it contains data from different IHEP experiments performed in the period from 1997 to 2000 and presents the measured extraction efficiency for various crystals as a function of the crystal length in the beam direction, compared with the Montecarlo simulation. This plot shows that the deflection efficiency can reach a very high value, thanks to the multipass mechanism, for very short crystals; the highest efficiency value is $85.3 \pm 2.8\%$ obtained with a 2 mm long silicon crystal which deflects $\sim 10^{12}$ protons in spills of ~ 2 s.

To make a crystal deflector this short, the strip geometry has been used: a narrow (111) silicon strip, of about 40 mm in the vertical direction and a fraction of millimiter in the radial one, is bent by a metallic holder providing a curvature along the vertical direction. In this way the strip has the shape of a saddle obtaining an additional curvature in the radial direction which is used for channeling; a scheme of the strip and a more detailed description can be found in sec. 3.1.4.1. The extraction efficiency is given by the ratio of the extracted beam intensity, as measured on the external beamline, to all the beam losses in the entire ring. The intensity of the extracted beam was measured with two independent monitors of secondary emission while the reduction in the circulating beam was measured with beam transformers [41].

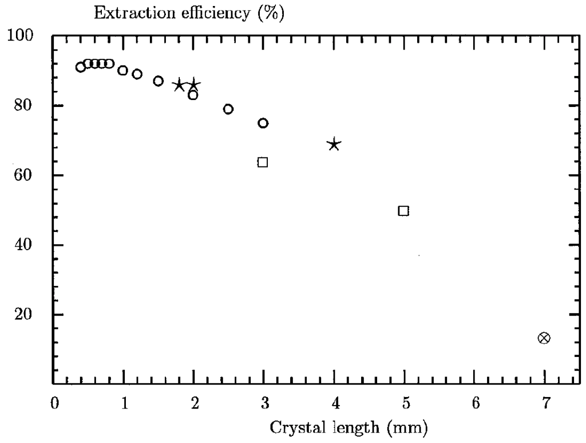

Figure 2.2: Crystal extraction efficiency for 70 GeV protons as a function of the crystal length. IHEP measurements ($\star$, $\otimes$ for a strip crystal; box for an O-shaped crystal) and Montecarlo prediction for the ideal strip ($\circ$).

In crystal collimation experiments, a bent crystal is positioned upstream of a secondary collimator (a stainless steel absorber 4 cm wide, 18 cm high, 250 cm long). This setup allows an independent check of the crystal channeling efficiencies and also gives the opportunity to work with different bending angles, unlike the extraction setup where the crystal bending angle is dictated by the geometry of the extraction. The intensity of the deflected beam is monitored with a profilometer which measures the particle intensity on the absorber entry face as a function of the radial position with respect to the beam direction. Fig. 2.3 shows a series of intensity profiles recorded by the profilometer which illustrates the effect of the crystal when used as a primary collimator. In the first plot an amorphous target is used as a primary collimator while the crystal is kept outside the beam. As expected, the beam profile is peaked at the collimator edge. In the second plot the crystal substitutes the amorphous collimator but is not aligned with the beam so it behaves exactly like an amorphous target. In the third plot the crystal is properly aligned with the beam direction and channels the particles; thus most of the incoming beam is deviated in the center of the bulk absorber entry face (peak in the center of the plot).

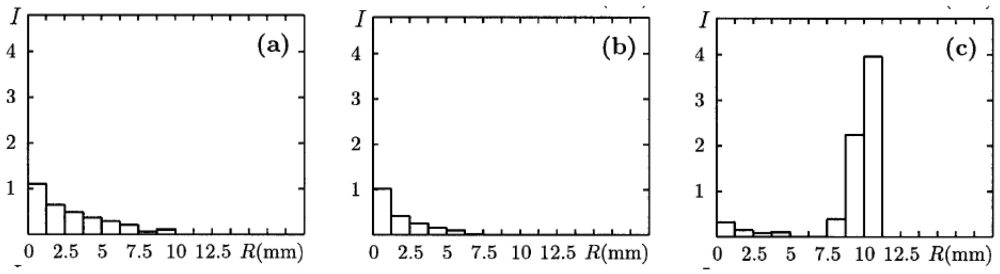

Figure 2.3: The radial beam profile observed at the entry face of the stainless steel absorber: a) the crystal is out of the beam which is scraped by the collimator alone; b) the crystal is in the beam but misaligned; c) the crystal is in the beam aligned.

The presented channeling collimation setup was also tested for the different particle energies available in the main ring of the IHEP U-70 accelerator.

A long and stable measurement has been performed at the injection energy of the accelerator (1.3 GeV). Fig. 2.4(a) shows the intensity profile recorded at this energy by the profilometer placed in front of the absorber; the crystal in use is the same which shows an efficiency of about 85% at 70 GeV. The channeling peak is still evident and the efficiency is about 15-20% which is a very high efficiency if compared to the previous measurements in the low-GeV energy range. The black area is the Montecarlo prediction which appears in good agreement with the measured data.

Another interesting test was performed during the particle acceleration from the injection energy of 1.3 GeV to the maximum energy of 70 GeV. The deflection

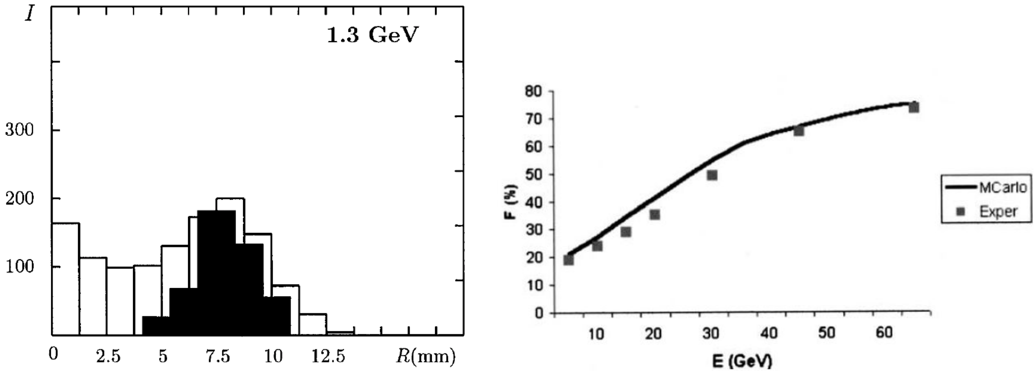

(a) (b)

Figure 2.4: a) Beam profile measured on the collimator absorber entry face with 1.3 GeV protons; the black area shows the simulated profile of the channeled peak. b) Crystal collimation efficiency measured during the accelerating phase of the U-70 ring, compared with the Montecarlo simulation.

efficiency has been measured for 7 different energies as shown in fig. 2.4(b) where the recorded efficiency is compared with the Montecarlo simulation.

2.2.2 The RHIC and Tevatron experiments

Two significant crystal channeling collimation experiments took place at the RHIC (New York) and Tevatron (Illinois) accelerator colliders. These experiments have many common features: they used the same crystal and an equivalent method to check the results. Differently from the IHEP experiments where the crystal collimators are tested to explore their potentiality, the RHIC and Tevatron measurements were addressed to increase the accelerator performance mainly reducing the experiments background. This target and the possibility to have a feedback from the running particle physics experiments gave to these experiences an important role for the future of crystal collimation. The RHIC experiment will be described in more detail, although its final result is negative, because it has several interesting features: first of all, it points out the importance of the beam characteristics knowledge showing the complexity of a crystal collimation experiment; secondly it has obtained a value of channeling efficiency with ions (Au) similar to the one reached with protons (interesting for the LHC collimation); last, but not least, the crystal scan shows a not well understood behaviour in the volume capture-reflection angular region. The Fermilab experiment also shows this crystal behaviour, but it will be described more shortly underlining the results and their possible explanations.

The relativistic Heavy Ion Collider (RHIC) consists of two 3833 m superconducting rings which can accelerate a range of ion species from protons to fully stripped gold ions. RHIC needs an efficient collimation system to remove the tails of the beam, minimize the distributed losses and reduce the background. For this reason before 2003 a bent crystal was installed in one of the RHIC rings as the first stage of a two collimation system with the goal of measuring its performances [42]. A scheme of the RHIC collimation experiment is presented in fig. 2.5. The crystal is located in the “CC Vessel“; it is an O-shaped silicon crystal, produced at PNPI (St. Petersburg) and mounted in the holder at IHEP (Protvino). Fig. 2.6 shows a schematic of the bending mechanism and a photo of the crystal mounted in the holder. The crystal length in the beam direction is 5 mm, its width is 1 mm and the bending angle is $\theta_b = 440\ \mu$rad. The crystal sits at the end of a long lever arm mounted on a pivot that moves it in the transverse direction with respect to the beam one; its angle in the horizontal plane is changed by a piezoelectric inchworm, which pushes the lever arm. The crystal angle is determined by reflecting a laser beam from the crystal face and measuring its deflection with a resolution of about 25 μrad (the laser setup is shown in fig. 2.5). About 6 m downstream with respect to the crystal position, a 450 mm long dual plate copper scraper is placed to stop the crystal channeled beam. Fig. 2.5 also shows the detectors setup dedicated to the crystal performance measurements; it is composed of: 2 scintillators that form a hodoscope to monitor particles scattered at large angles by the crystal; 8 upstream (before the copper scraper) PIN diodes, used to detect particles scattered by the crystal; an array of 4 downstream PIN diodes to detect particles scattered by the scraper and 4 dedicated ionization beam chamber monitors to measure large beam losses downstream of the scraper.

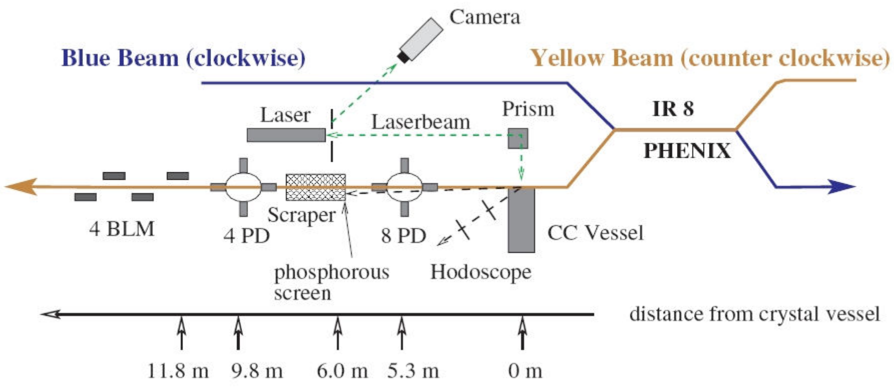

Figure 2.5: The RHIC crystal collimation setup.

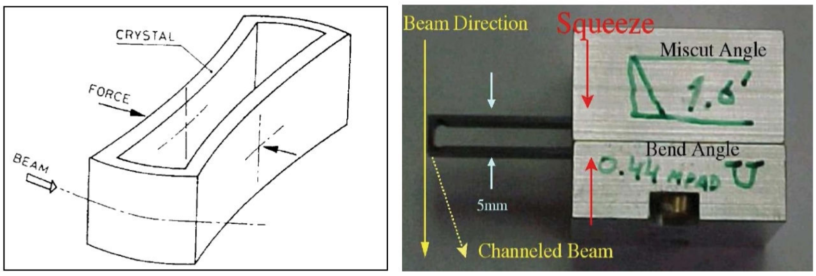

Figure 2.6: On the left, a scheme of the O-shaped bending mechanism; on the right, a photo of the O-shaped crystal used at the RHIC and Tevatron accelerators mounted on its aluminum holder.

Data were taken during all the RHIC runs between 2001 and 2003 with a variety of beam and optics combinations, during the routine operation and with minimal interference to the RHIC detectors. The data taking was organized in ”scans“ which started with the insertion of the crystal in a transverse position such that the scattering of the halo particles was detected by the upstream PIN diodes and went on with the rotation of the crystal through a range of angles with respect to the beam direction. During each scan, the beam loss rate was measured by the available detectors; fig. 2.7 shows an example of a typical crystal scan using one of the upstream PIN diodes to monitor scattering from the crystal. The drop in the scattering indicates channeling in the crystal; the channeling efficiency is determined dividing the depth of the channeling dip by the background rate. Each of the hodoscope scintillators and their coincidence were also analyzed but the background coming from particle scraping immediately upstream of them reduced the signal to noise ratio and made it difficult to use the data. The downstream PIN diodes are not useful for the analysis because they are also sensitive to scattering from the copper scraper.

A simulation was written to study the collimation feasibility. It is a C++ program which tracks particles around RHIC for a given number of turns in the range of the crystal deflection angles [42]; it uses the Montecarlo simulation CATCH (the one used also in the IHEP experiment) which simulates the crystal lattice behaviour. The simulation of the crystal behaviour in a circular accelerator has to take the beam parameters in consideration and, as it will be shown, the RHIC experimental experience indicates that the knowledge of the beam features in the crystal region is a crucial aspect to understand the channeling experimental results.

The fundamental beam parameter is the divergence of the particles impinging on the crystal entry face. In fact, the crystal can be turned to be aligned with respect to the particles average direction but if their divergence exceeds the crystal

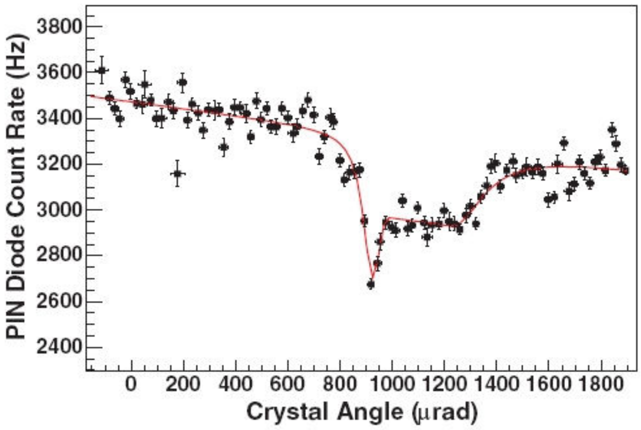

Figure 2.7: Typical crystal scan with a gold ion beam. The red line corresponds to a fit with a function given by two shifted Lorentian dips. The maximum channeling efficiency is about 25% which represents a very high efficiency if compared with the 11% obtained at the SPS with Pb ions [43].

critical angle θ_c (defined in sec. 1.1.1) the fraction of channeled particles should be proportional to θ_c/Φ where Φ is the rms of this divergence. The computed geometrical crystal acceptance (A_g) is given by:

$$A_g = \frac{2(d_p - x_c)}{d_p}\frac{\pi}{4} \simeq 0.66\frac{\theta_c}{\Phi} \tag{2.1}$$

where d_p is the crystal lattice interplanar spacing and x_c is the maximum distance from the center of the channel that a particle can have without being scattered away from the nuclei (both of them are defined in sec. 1.1.1). The factor $\frac{2(d_p - x_c)}{d_p}$ takes into account the lattice spatial acceptance and the factor $\frac{\pi}{4}$ the details of the calculation, performed assuming a uniform angular distribution of the incoming beam and the harmonic approximation of the crystal interplanar potential. The result refers to a (110) oriented silicon crystal which is the case of the RHIC collimator crystal.

Fig. 2.8(a) shows the beam horizontal phase space as it was expected in the crystal collimator location. The beam phase space in a transversal direction is given by the distribution of the angles between the nominal beam direction and the particle trajectory (projected on a transversal coordinate as the horizontal one) as a function of the particle coordinate in the same transversal direction. The accelerator theory [37] shows that the particles distribution in the transversal phase space has an elliptical form; the ellipses plotted in fig. 2.8(a) represent the boundary of this phase space distribution at different standard deviations (a gaussian beam profile is assumed). The phase space area covered by the ellipse at one standard deviation is called transverse emittance; it is an important beam quality concept (measured in rad·m) which reflects the beam production process from the source to the bunch preparation. It is interesting to note that the emittance is independent from the beam optics (magnets) and it is constant in each region of the accelerator; the accelerator optics can only modify the ellipse shape: for example near the interaction region the beam should be focused to increase the luminosity but this implies that its divergency increases.

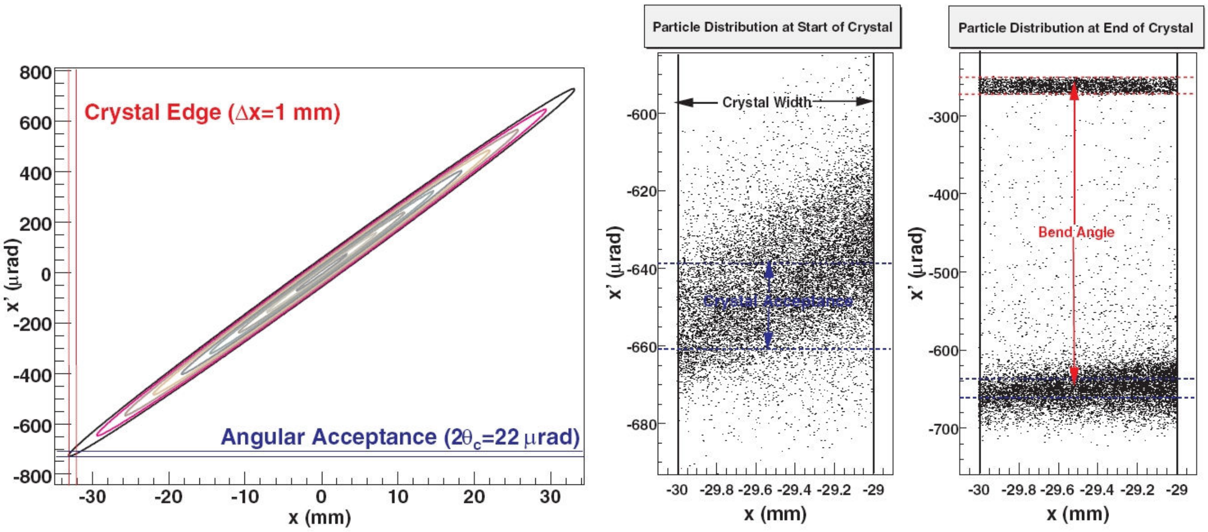

(a) (b)

Figure 2.8: a) Design beam horizontal phase space at the RHIC crystal collimator; the contours represent the beam distribution at a distance of 1 σ between each other, assuming a 15 π·mm emittance. b) Simulation of the particle hitting the crystal collimator in the horizontal beam phase space: on the left, at the entrance of the crystal (the crystal angular acceptance is indicated); on the right, at the end of the crystal (both the angular acceptance and the crystal emittance are indicated) [42].

The two orthogonal bands in fig. 2.8(a) represent the crystal spatial acceptance (vertical band) and angular acceptance (horizontal band): the particles contained in the intersection of the two bands can be channeled. The position of the vertical band depends on the crystal position (it is imposed by the collimation necessity) while its width depends on the crystal thickness. The position of the horizontal band depends on the crystal orientation and can be adjusted (rotating the crystal) to match the beam average angle on the crystal entry face; the width of this band, which is the crystal critical angle, depends on the crystal physics and cannot be changed.

The plots of fig. 2.8(b) show the simulated positions of the particle in the horizontal beam phase space: in the plot on the left, at the entrance of the crystal on the first turn of the simulation (the edges of the crystal and the range of angles within its acceptance are shown); in the plot on the right, at the exit of the crystal after many turns. The channeled particles appear between the red dotted lines; they received an angular kick approximately equal to the bending angle of 440 μrad which is enough to reach the copper collimator.

Fig. 2.9 shows a comparison between the simulation and the data of the 2001 run. The blue curve is obtained using the design beam parameters (phase space of fig. 2.8(a)); after 20 turns it reaches the promising channeling efficiency of 56±1%. The agreement between data and simulation is not good: the channeling dip is less deep in the data and shifted suggesting that the effective beam parameters are different from the design ones. In particular a rotation of the phase space ellipse could explain the horizontal shift of the channeling. In fact a measurement of the beam phase space showed a disagreement with respect to the design value revealing a greater slope of the phase space ellipse. The red curve in fig. 2.9 is given by the simulation once modified with the measured optics information; it reproduces the general shape of the data. Note that both data and simulation beside the channeling dip present a reduction in the scattering between 800 and 1200 μrad. This is an interesting and unexpected feature that will be discussed at the end of the section.

The difference between the two simulations is due to the increased tilt of the phase space ellipse leading to a larger angular divergence striking the crystal which implies a lower efficiency according to eq. 2.1. The observed global efficiency was approximately 25% which means less than half of the original prediction.

Besides the equipment protection, the important goal of crystal collimation at RHIC was to reduce background in the experiments; various background signals were recorded by each experiment to measure the effectiveness of the crystal collimator. The STAR detector [44] being located directly downstream of the crystal position should be more sensitive to its effects. Fig. 2.10 shows the STAR background rates in presence of the crystal (normalized to the uncollimated one) as a function of the distance between the crystal and the scraper. A negative position indicates that the crystal is closer to the beam than the scraper; the few times that the crystal collimation seems successful, shown by the points below the dotted line, are not understood since there is no reason why these points should be more successful than the neighbouring ones. The conclusion is that the collimation using crystals in these RHIC locations is unsuccessful. The reason why the

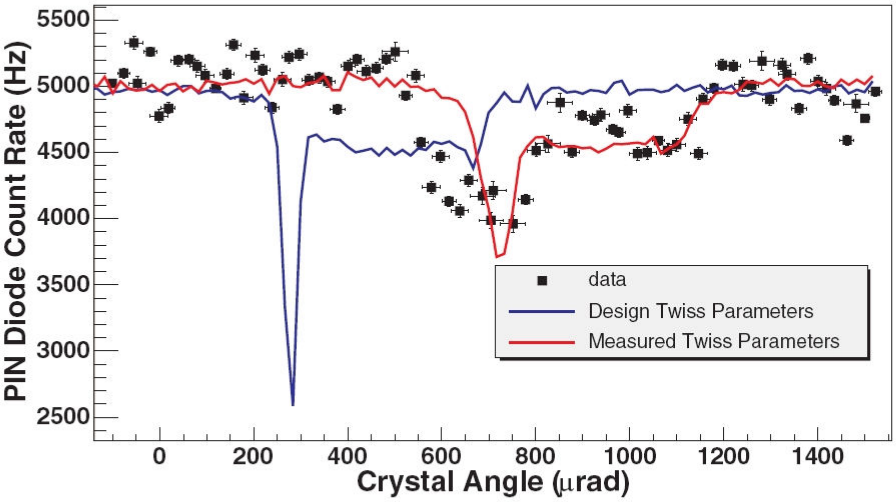

Figure 2.9: Comparison between the 2001 RHIC data and Montecarlo simulation [42].

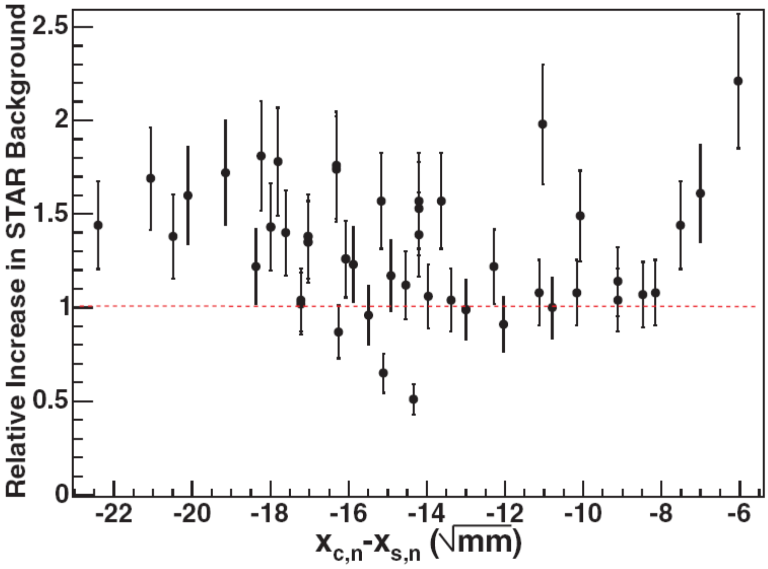

Figure 2.10: The relative background measured by the STAR experiment as a function of the distance between the crystal and the secondary collimator. The red line indicates where the crystal equals the standard collimated background. The error bars are statistical [42].

crystal does not act as a good collimator is the low channeling efficiency because of which the large amount of scattering caused by the crystal cannot be removed by a single scraper. On the other hand, the experiments have shown that an accurate knowledge of the beam phase space is necessary to predict the channeling efficiency; in particular the beam optics in the crystal location should be adjusted to present a small beam divergence at the crystal entry face to match the crystal channeling angular acceptance which is a fixed parameter. In the RHIC case it was not possible to adjust the beam optics to the ideal value as the crystal was located in an interaction region matching section. On the other hand all the available locations (the RHIC warm section) have similar beam parameters. For these reasons the crystal collimator was removed after the 2003 run and the RHIC standard collimation system was upgraded [45].

In the RHIC collimation data analysis a major attention was dedicated to the channeling efficiency measurements and simulation; however the data (see fig. 2.7) also showed an interesting and originally unexpected scattering reduction in the angular range between 1000 and 1400 μrad. This shoulder in the collimation plot is also reproduced by the Montecarlo simulation (as shown in fig. 2.9) which, to track the particles in the crystal, assumes a Moliér potential for each atom of the crystal lattice (sec. 1.1.1). Even though the agreement between data and simulation is good, the interpretation of this effect is not so easy. Before presenting a possible interpretation a brief description of the Tevatron experiments will be given since the same RHIC effect is present also in the Fermilab data.

The Tevatron accelerator had a very high background level at the CDF and D0 experiments [46]; in the 2004 shutdown, to solve this problem the machine alignment and the vacuum system were improved. On this occasion also a crystal collimator was installed to verify if it could help to reduce the proton losses; fig. 2.11 shows the background level at CDF and D0 before and after the 2004 machine development.

The Tevatron crystal collimation experiment was performed in 2005 and used the original RHIC goniometer and the same O-shaped crystal. They were positioned in a Tevatron straight section, where the crystal replaced a primary tungsten collimator and the remaining part of the two collimator system could be used. Fig. 2.12 shows a schematic of the collimator experiment and some photos of the setup. As in the RHIC experiment, a PIN diode was used to measure the scattering rate after the crystal to understand when the beam is channeled.

Fig. 2.13 illustrates a typical crystal scan using the PIN diode which measures a scattering rate proportional to the nuclear interactions (large angular scattering) in the collimator. The dip in the plot corresponds to channeling which is due to two effects: on one hand, when a particle is channeled, the nuclear interactions are suppressed (see chap. 1); on the other hand, the particle is deviated towards the secondary collimator where, being absorbed, loses the possibility to be scattered

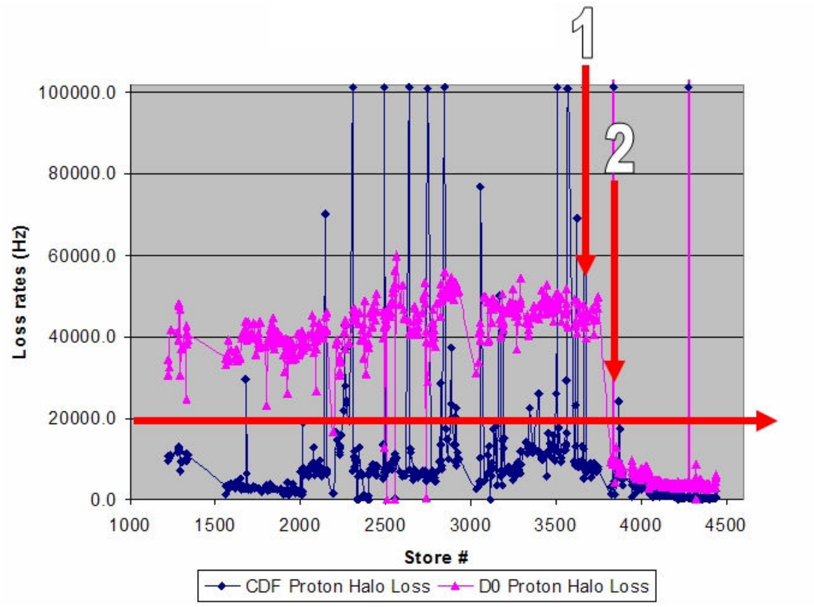

Figure 2.11: Proton halo rate recorded at the Tevatron by the two experiments CDF and D0. The horizontal arrow represents the proton halo loss limit while the vertical ones indicate the machine developments performed to reduce background: 1) the installation of a double scraper; 2) the improvement of the vacuum system and of the alignment; in this occasion the crystal collimator was installed [46].

on one of the next turns. This explanation is important to understand the origin of the shoulder near the channeling dip which characterizes both the RHIC and Tevatron data (sec. 2.2.2.1).

Besides this new and unexpected feature, the Tevatron collimation experiments have measured a channeling efficiency of 78±12%, positively influencing the background rate at the particle experiment [46]. According to these results the Tevatron crystal collimation experiments will continue testing the new and short IHEP crystals also with the goal of obtaining information for the development of a high performance collimation system for LHC.

2.2.2.1 The whole arc effect

As underlined in the previous section, both the RHIC (fig. 2.7) and Tevatron (fig. 2.13) experiments presented an unexpected feature which, although reproduced by the Montecarlo simulation, remains of difficult interpretation. The feature consists in a reduction of the background rate during the crystal angular scan, after the channeling orientation; the width of this shoulder seems to correspond to

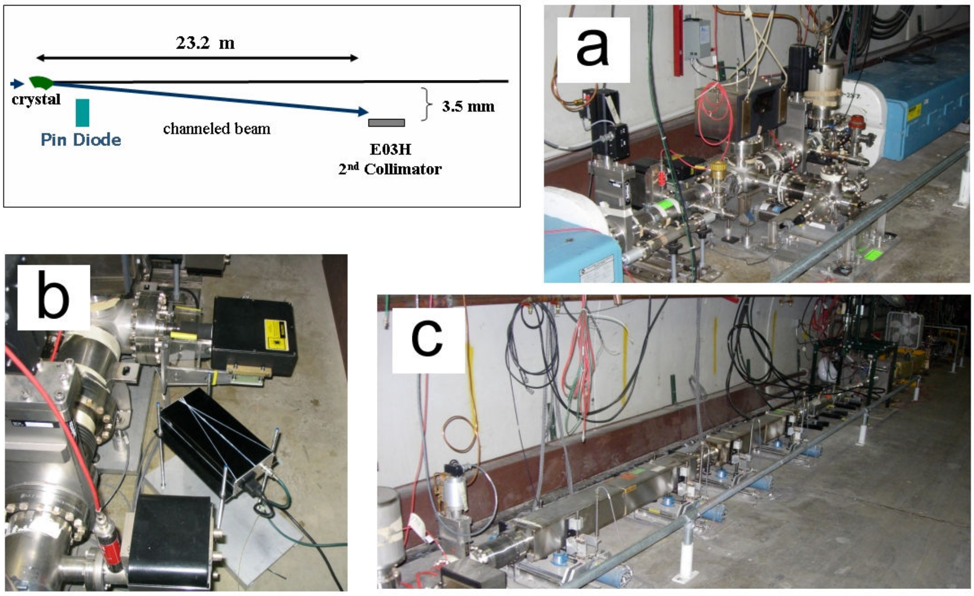

Figure 2.12: Tevatron crystal collimation setup: a schematic with some pictures: a) the crystal collimator assembly; b) the PIN diode; c) the secondary collimator.

the crystal bending angle ($\theta_b = 440$ μrad while $\theta_{shoulder-Tevatron} = 460 \pm 20$ μrad) which explains the name “whole arc effect”. This characteristic suggests that a “volume” effect is going on; in fact, when the entry face of the crystal is misaligned with respect to the beam of an angle $\theta \leq \theta_b$, the crystal bending provides a tangency point between the particles and the atomic planes inside the crystal (in its volume). In this point either the volume capture (sec. 1.2.2) or the volume reflection (sec. 1.2.3) can happen.

The volume capture deviates the particles in the channeling direction, but as it starts inside the crystal, the captured particle can follow only the final part of the channel so that its deflection angle decreases as the crystal misalignment increases. Moreover the volume capture efficiency is very small compared to the channeling one. Taking into account these factors the computed probability for a particle to impinge on the secondary collimator due to volume capture is 2% for the RHIC case and 0.5% for the Tevatron one. The single turn volume capture probability appears too small to justify the intensity of the whole arc effect but taking into account the multipass effect the volume capture efficiency can dramatically change. The multipass effect, in fact, multiplies the particle crossing of the crystal, increasing the crystal effect (for example channeling) probability; the limit of this mechanism is the multiple scattering in the crystal itself, which eventually misalignes the particle taking it outside the angular acceptance of the

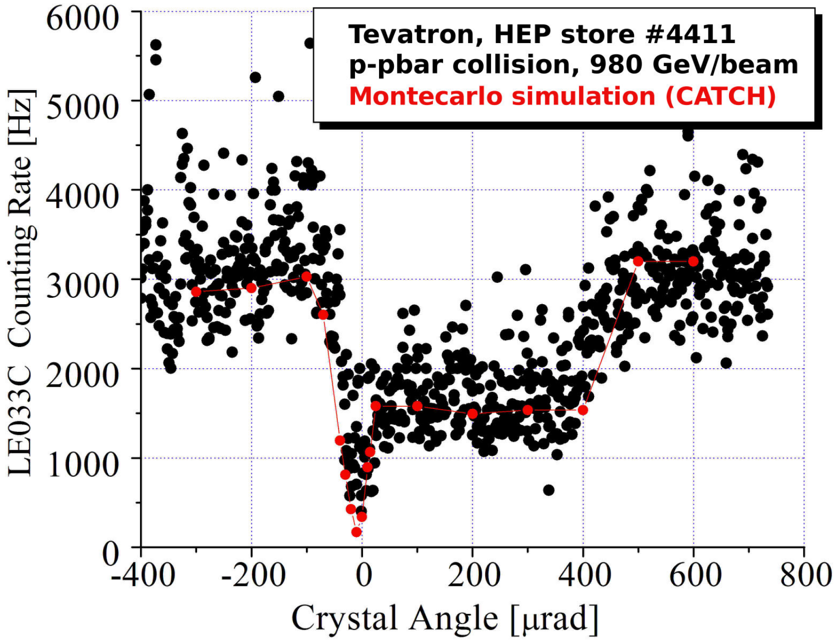

Figure 2.13: An angular crystal scan: PIN diode counting rate as a function of the crystal angle (black points); CATCH Montecarlo simulation (red points).

considered crystal effect (for example θ_c for channeling) making it impossible.

The angular acceptance of the volume capture is the crystal bending angle $\theta_b \gg \theta_c$ which means that the multipass effect weight is greater for the volume capture than for channeling. Indeed the volume capture could be an explanation of the whole arc effect as it was considered when the whole arc effect emerged. Fig. 2.14 shows the RHIC data compared with different Montecarlo simulations performed requiring an increasing number of turns; as expected the whole arc effect increases with the number of turns. The simple model used for this simulation is not able to compute a possible survival time for the particles; in other words the number of turns must be an input of the simulation. The strong dependence of the whole arc effect on the number of turns can be used to fix the average number of turns per particle; in the RHIC case this number is about 20 as can be seen in fig. 2.14.

Both the RHIC and Tevatron collimation experiments did not have a detecting system able to recognize the particle trajectory after the passage through the crystal but the agreement with the simulation suggests to use it to clarify the whole arc effect origin. Fig. 2.15 shows the simulated angular deflection distribution of particles interacting with the misaligned crystal: Au ions of 100 GeV/c for the

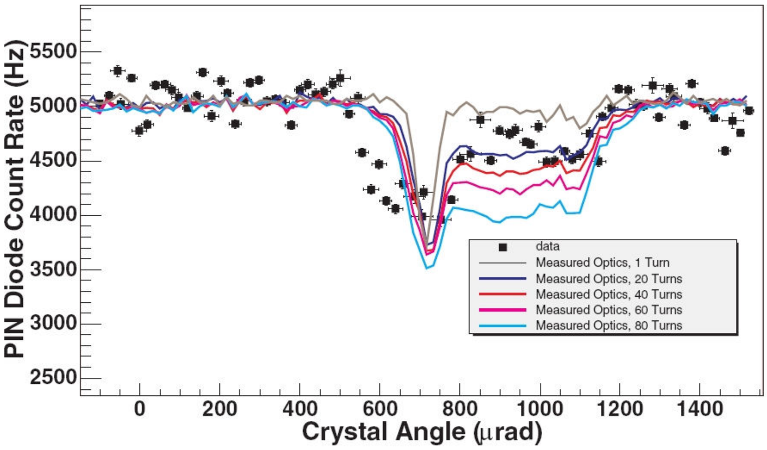

Figure 2.14: RHIC data compared with several simulations with different number of turns. The depth of the whole arc shoulder increases with the number of turns in the simulation.

RHIC collider and protons of 980 GeV/c for the Tevatron. In the plot, a positive angle corresponds to the bending direction (the one of a channeled particle); the two distributions are shifted on the opposite side as a result of the coherent scattering with the atomic potential, an effect called volume reflection. The average deflection angles are -17 μrad for RHIC and -5.3 μrad for Tevatron; these values are in agreement with the volume reflection theory within 1-2 critical angles. As predicted by the first simulation which discovered the effect, the volume reflection is extremely efficient, practically all the non volume captured particles are reflected. Apart from the angular shift, the distribution shows a greater broadening if compared with the effect of the multiple scattering: the deflection angle rms due to reflection is 22 μrad for RHIC and 7.2 μrad for Tevatron while the corresponding multiple scattering angles rms in the same silicon thickness are 13 μrad and 3.3 μrad.

The “increased multiple scattering” effect of the volume reflection gives an alternative interpretation of the whole arc effect. The PIN diode counting rate is proportional to the nuclear interactions in the crystal (angular scattering at large angles). As explained, this allows to detect the channeling because of two reasons: it reduces the nuclear interactions for particles that are channeled and extracts them from their orbit limiting the number of passages through the crystal thus reducing the effective silicon thickness. The second effect results to be the dominant one as the crystal thickness (5 mm) is very small compared with the proton nuclear interaction length. Indeed the background level recorded by the PIN diode

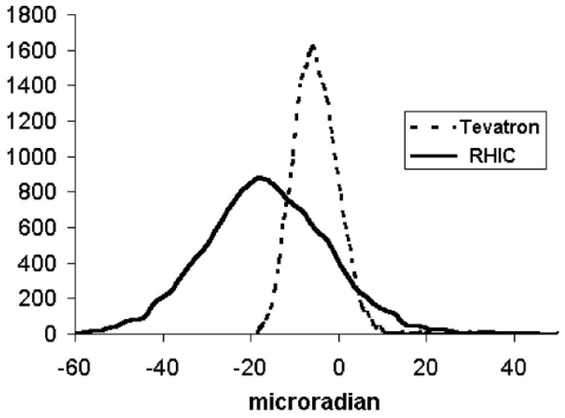

Figure 2.15: Particle deflection angle distributions due to the passage through a misaligned crystal in the RHIC and Tevatron case [47].

strongly depends on the number of turns available for the particles impinging on the crystal.

The channeling effect and the volume capture one extract particles from the orbit which goes through the crystal in less turns than the multiple scattering; the volume reflection produces the same effect, in fact it behaves as an "increased multiple scattering". In other words during the volume reflection, the multiple scattering in the crystal increases as if the crystal were longer while the nuclear interaction probability remains constant; so particles have a larger probability to leave their orbit (being absorbed in some accelerator elements) before having a nuclear interaction in the crystal.

The Montecarlo simulations foresee an extremely high volume reflection efficiency which suggests the whole arc effect to be dominated by the volume reflection (although a volume capture contribution should be present). It is evident that a direct experimental measurement should be performed to confirm the simulation results as the importance of such effects in beam dynamics is very high.

In the RHIC and Tevatron experiments, the volume reflection behaves as an increased multiple scattering reducing the nuclear interaction in the crystal. This can have some advantages in the development of a collimation system but is far from the original more intriguing idea of steering particles towards the secondary collimator core. The experiment that will be discussed in the following of this thesis will show a detailed study of volume reflection suggesting that besides the "increased multiple scattering" effect its deviating power can be used to create a channeling-like multistage collimator system with the advantages of a greater efficiency and angular acceptance.

2.3 The LHC collimation

LHC is designed to perform proton-proton collisions at a center of mass energy of 14 TeV with unprecedented high beam intensities: each beam should be filled with 2808 bunches of $1.1 \cdot 10^{11}$ protons which means a total of $3 \cdot 10^{14}$ protons. Taking into account the single proton energy, one can compute that LHC will store two beams with 330 MJ each, with a transverse energy density between 1 MJ/mm^2 to 1 GJ/mm^2. A comparison between the stored energy values of the principal high energy accelerators is shown in fig. 2.16(a).

On one hand, the stored LHC energy is enormous, with unprecedent transverse energy density; on the other, its superconducting magnets would quench (at 7 TeV) because of a small amount of energy, that is about 30 mJ/cm^3 which can be induced by a local transient loss of only $4{\cdot}10^7$ protons. Any significant beam loss into the cold section must therefore be avoided and since a primary beam halo will continuously be filled because of the accelerator dynamics a powerful collimation system is needed. As shown in fig. 2.16(b), the proton loss rate for a realistic beam lifetime is from 1000 to 10000 times larger than the magnet quench limit. This means that out of 10000 lost protons no more than a few are allowed to escape from the collimators.

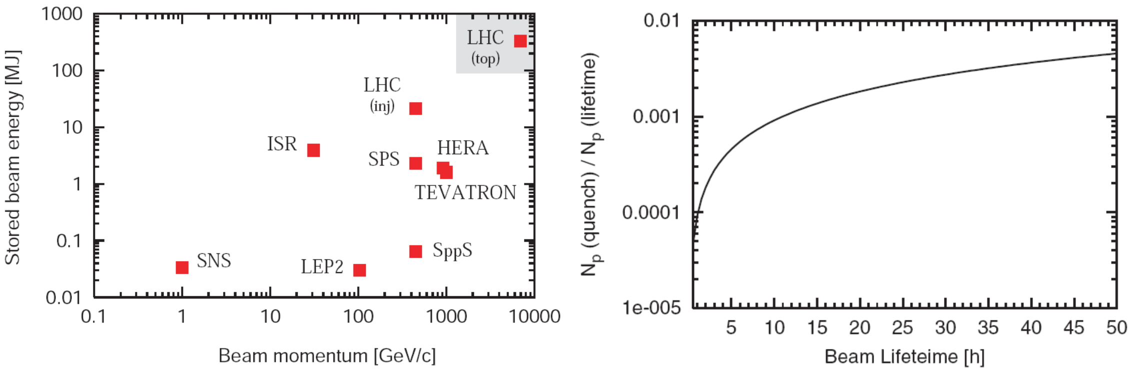

(a) (b)

Figure 2.16: a) Stored beam energy versus beam momentum for various past, present and future high power accelerators. b) Quench limit over the number of lost particles as a function of the beam lifetime.

The study performed on the LHC collimation challenge did not produce a single solution that fulfills all the machine design goals. The collimation system will be implemented in different phases so that the difficulties and the performance goals will be distributed in time, following the natural evolution of the LHC performance. The first phase is designed to be fail proof requiring a minimum number of interventions in the high radiation environment of LHC. This collimation system should limit the LHC luminosity to 40% of the nominal one. It is clear that such a system has to be modified to allow to reach the nominal machine luminosity with the help of a new generation of collimators which is not decided yet. The crystal collimator could be an interesting solution for this difficult task.

2.3.1 First phase of the LHC collimation

Although the LHC collimation system should be upgraded in the following operation years, the initial (phase 1) system will be the central part of the overall collimation setup.

Essentially this phase presents a collimation system designed to guarantee the maximum robustness against the great destructive power of the LHC beam both in normal and abnormal processes (such as irregular beam dumps, injection and oscillation).

Robustness is a collimation system key feature as its possible failures can seriously limit the LHC availability: a severe damage to a collimator in fact requires an immediate access in a high radiation environment and possible vacuum problems but also a non severe damage (small surface deformation) resulting in a reduced cleaning efficiency limits the machine performance, is difficult to be recognized and finally requires an intervention.

These damages should be avoided by a proper choice of an adequate material for the collimator jaws. The studies on the collimator materials are driven not so much by the standard collimation operation but rather by faulty operation in which a very high energy density can be deposited in the proton intercepting devices in a short time (nanosecond range). This limits the choice of materials to the low Z ones [48]. An increase in the atomic number Z in fact corresponds to a strong decrease in the radiation length which leads both to a larger contribution of the electron-gamma part within the cascade and to its higher spatial concentration, thus to a higher energy density concentration which causes a greater heating of the collimator. This effect is illustrated in fig. 2.17 where the maximum energy densities of different materials are plotted as a function of the mass length; the small Z materials (Be and graphite) show a clear advantage with respect to the high Z ones.

The final choice for the first phase setup is a graphite based collimation system (one of the secondary collimators is shown in fig. 2.18); a Be based collimator would not resist the specific one-turn energy load and would introduce concerns about toxic materials [49]. The graphite disadvantage is its poorly conducting power which increases the total impedance of the machine. The total LHC impedance is in fact dominated by the collimators impedance [50]. The impedance scales as the third power of the gap size and the collimators form very

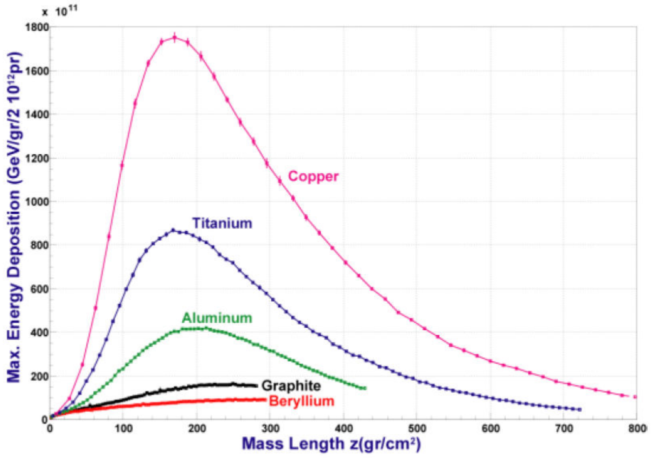

Figure 2.17: Maximum energy deposit in different materials per mass length; Fluka simulation [48].

small gaps at 7 TeV as shown in fig. 2.18(a). It has been computed that the collimator induced impedance is expected to limit the total machine intensity to about 30-40% of its nominal value [51].

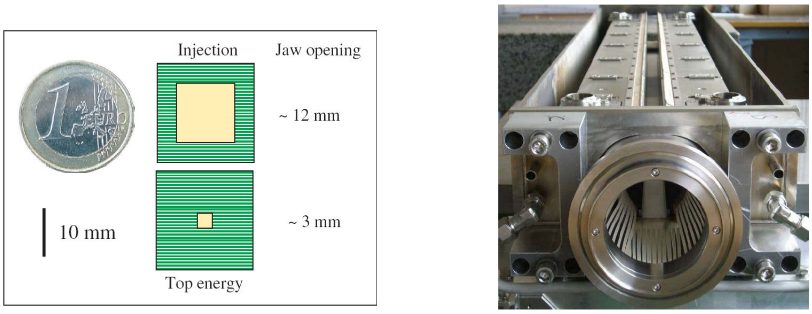

(a) (b)

Figure 2.18: a) Opening of the LHC collimators at nominal settings for injection (top) and 7 TeV (bottom). b) A view of a secondary collimator with fiber-reinforced graphite (CFC) jaws.

The initial LHC collimation layout which includes 88 ring collimators is summarized in fig. 2.19(a); the working principle of the setup is the following (schematically described in fig. 2.19(b)):

1. the shorter primary collimators (TCP) intercept protons from the primary beam halo at 6σ (rms of the beam profile) from the beam core with an

impact parameter (the average distance from the collimator surface and the proton impact position) smaller than 1 μm. The primary halo is therefore converted in a secondary one;

2. the longer secondary collimators (TCS) intercept the secondary halo at 7σ with a typical impact parameter of 200 μm. The small number of protons that escape these collimators populate the tertiary beam halo;

3. other absorbers and collimators around the ring at 10σ protect the superconducting area and other sensible insertions from the tertiary halo.

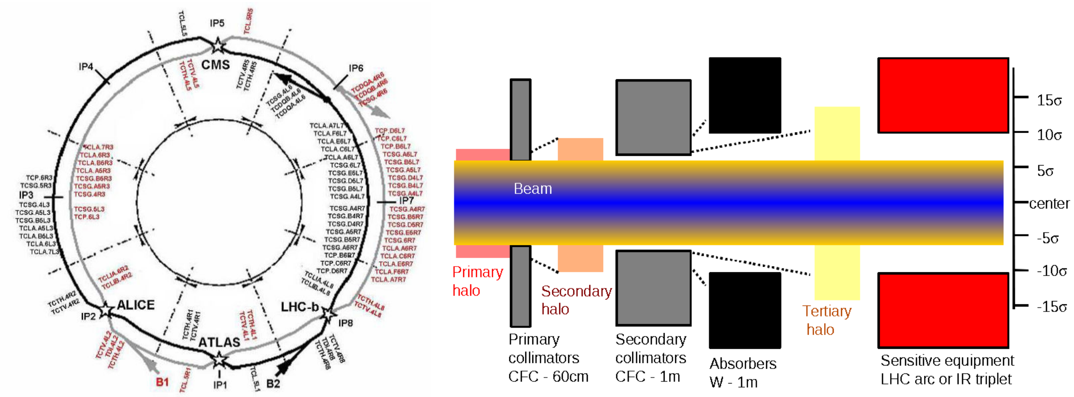

(a) (b)

Figure 2.19: a) Layout for the LHC collimation during phase 1. b) Principle of collimation and beam cleaning during collisions in phase 1.

The LHC luminosity is limited not only by the collimation system impedance, but also by its inefficiency which is compatible with the 40% of the nominal intensity; moreover it is expected that imperfections will reduce the collimation efficiency even further by a factor 2-4 [52].

The cleaning efficiency η_c is defined as the ratio between the number of protons that reach an amplitude (spatial position with respect to the beam nominal orbit) greater than 10σ outside the cleaning insertion and the protons lost in the cleaning insertion. This number can be computed from simulations which describe the halo behaviour, as shown in fig. 2.20(a) by integrating the tertiary halo above 10σ. The losses in the machine are distributed over a length which is called "dilution length" (L_{dil}) which for the LHC case is estimated to be about 50 m. According to this a local cleaning inefficiency $\eta_l = \eta_c / L_{dil}$ is defined. If R_q represents the magnet quench limit expressed in number of protons per meter per

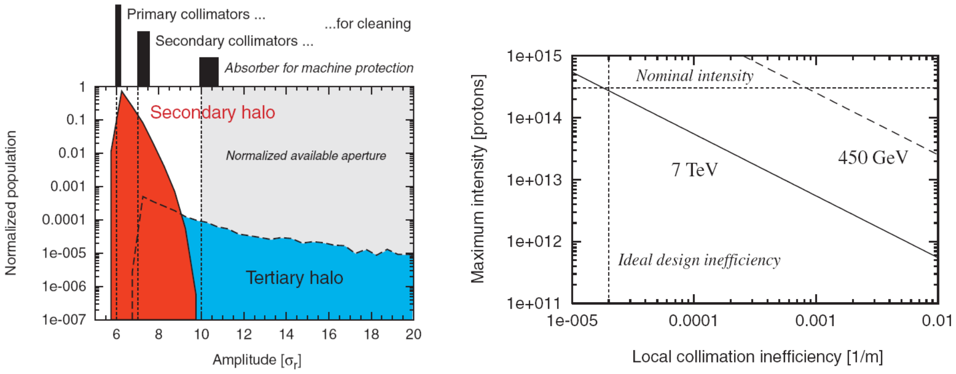

(a) (b)

Figure 2.20: (a) Normalized population of secondary and tertiary halo for protons impinging on the first collimator. (b) Beam intensity versus local cleaning inefficiency; a minimum allowed lifetimes of 0.2 h (7 TeV) and 0.1 h (450 GeV) are assumed. The nominal machine intensity requires an ideal local inefficiency of $2{\cdot}10^{-5}$ m^{-1}.

second, the maximum allowed proton loss rate R_{loss} in the machine is:

$$R_{loss} = \frac{R_q \cdot L_{dil}}{\eta_c} \tag{2.2}$$

As R_{loss} is $\Delta N_p/\Delta T$, that is the number of protons lost per unit time, the beam lifetime is given by:

$$\tau = -\frac{\Delta T}{ln\left(1 - \frac{R_{loss}\Delta T}{N_{tot}}\right)} \simeq \frac{N_p^{tot}}{R_{loss}} \tag{2.3}$$

where N_p^{tot} is the initial number of protons. N_p^{tot} is defined from R_{loss} which represents the maximum allowed proton loss before quenching; in other words, it represents the maximum beam intensity compatible with a given beam lifetime τ. The required minimum beam lifetime for the LHC operation (τ_q) is 0.2 h [53]. So the maximum number of protons in the LHC beam can be derived as a function of the local collimation inefficiency:

$$N_{tot} = R_q \cdot \tau_q \cdot \frac{1}{\eta_l} \tag{2.4}$$

Fig. 2.20(b) shows the maximum proton intensity as a function of the local collimation inefficiency, both at the injection energy (450 GeV) and at the top one (7 TeV). At the top energy a beam lifetime (τ_q) of 0.2 h and a quench level (R_q) of $7{\cdot}10^8$ protons/(m·s) have been considered. To allow the nominal beam intensity ($3\cdot10^{14}$ protons), a local cleaning inefficiency below $2\cdot10^{-5}$ m^{-1} should be achieved. At the injection energy the quench level is much lower, R_q =$7.6\cdot10^6$ protons/(m·s), and the collimation has less stringent requirements. As anticipated, in the present collimation layout, the ideal cleaning inefficiency is not reached; this is one of the reasons that make the collimation upgrade an important task in the LHC future.

2.3.2 The crystal option

In the previous section it has been pointed out that the actual LHC collimation system limits the machine luminosity to about 30-40% of the designed one. In addition to this, the collimator jaws will experience long term damage due to beam loss induced radiation. An upgrade of the system and the R&D on advanced collimators are therefore an important part of the LHC collimation system. 34 ring locations have been already equipped for this mandatory upgrade but the final design choices and decisions will be based on the experience with the LHC beams and the initial collimator system. Many aspects of LHC including its collimation system present uncertainties, as an unknown energy range will be probed, so the information from its first operational period will be very useful to decide the future upgrades, even though it is already known that the collimation system phase 2 should be based on an innovative collimator design.

Bent crystals represent a possible solution for the LHC collimation upgrade. The idea of the crystal collimation is based on the substitution of the primary collimator with a bent crystal, as schematically shown in fig. 2.21: while the amorphous primary collimator transforms the primary halo in a wider secondary one, a crystal collimator deviates the primary halo outside the beam (studies where performed to obtain an extracted beam from the LHC halo [31]) so that it can be more easily absorbed. In this way the collimation efficiency increases giving a greater freedom in the collimation system design so that also the collimator impedance could be reduced. A real estimation of the crystal collimation performance will be given through Montecarlo simulations which integrate the crystal channeling physics in the LHC environment. The reliability of these simulations depends on the knowledge of the crystal physics and on the capability of developing a technology for the crystal bending and assembly adequate for a large scale use of crystals as collimators.

This section briefly lists the open questions as far as crystal collimation is concerned; some of these questions are being addressed in the experiments described in the second part of this thesis work. The arguments concerning *the crystal deflection properties* and the one related to *the integration in the LHC machine environment* can be ideally divided as they require different know-how.

The topics which can be collected in the first class are: **the efficiency** and **the**

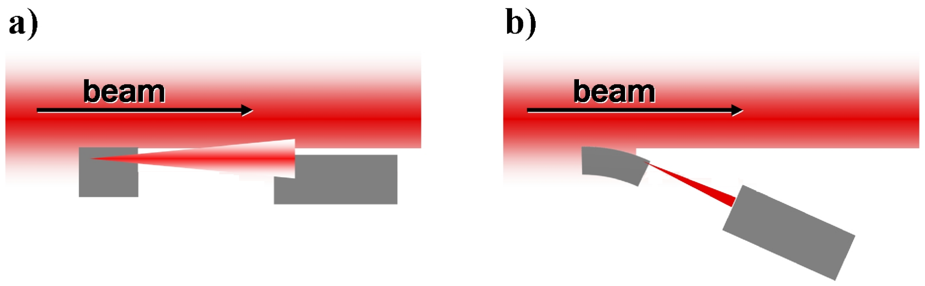

Figure 2.21: a) Traditional multistage collimation system: an amorphous target spreads the primary halo (secondary halo) so that most of it can be intercepted by a (more distant with respect to the beam) secondary collimator. b) Crystal based collimation: a bent crystal deviates (through channeling) the primary halo into an absorber.

angular acceptance of the crystal which are crucial to evaluate the performance of the final collimation setup; **the angular deviation width** and **the shape of the deflected beam**. Starting from these points, in the following description some arguments already discussed in the chapter are summarized and a comparison between the crystal channeling and the volume reflection is presented.

Crystal efficiency

It is the probability for a halo particle to be deflected by the crystal; only a high efficiency allows a good cleaning performance. Indeed this is the crucial task for the crystal collimation feasibility. The research for a high deflection efficiency has identified three collimation possibilities: the “singlepass” channeling which consists in the channeling in a crystal so long that the channeling probability in a second turn is highly suppressed; the “multipass” channeling, in which the crystal length is optimized to allow the multipass, granting a high efficiency (fig. 2.22 shows a Montecarlo simulation for the LHC condition) and finally the volume reflection which is characterized by a high singlepass efficiency, close to 100%. Several considerations on the efficiency bring to exclude the possibility of using a long crystal and seem to favour the volume reflection effect, which however provides a smaller angular deflection. Thus multipass and volume reflection are still an open choice.

Angular acceptance

It represents the angular range of the incoming particles in which the crystal deflection can take place. It is traditionally included in the crystal efficiency (see eq. 2.1) and can be thought of as an efficiency component depending on the beam

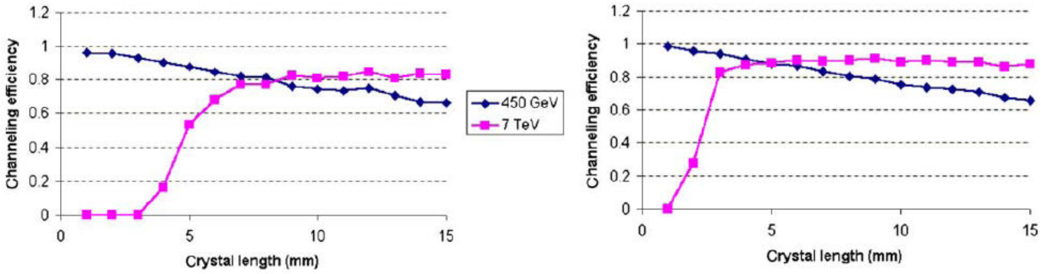

Figure 2.22: Simulated channeling efficiency as a function of the crystal length for both the injection energy and the top one of the LHC beam; the crystal bending radii are adjusted to obtain a deflection angle of: 200 μrad (left) and 100 μrad (right) [54].

characteristics (divergence in the bending plane). The channeling angular acceptance is fixed and it is the Lindhard critical angle (eq. 1.11) which depends on the energy. It is 9.4 μrad at the LHC injection energy and 2.4 μrad at 7 TeV. The volume reflection angular acceptance corresponds to the crystal bending angle which can be adjusted and it is usually larger than 100 μrad; the large angular acceptance is one ingredient of the volume reflection high efficiency. In fact, a larger angular acceptance implies more stability with respect to the beam variations and less stringent alignment requirements.

Deflection angle

It is the entity of the angular kick provided by the primary collimator; multiplied by the distance from the secondary collimator it gives the average impact parameter on its surface. A larger impact parameter facilitates the absorption of the extracted beam by the secondary collimator. In addition to this a larger angular kick allows to obtain a given impact parameter with a more compact system. So in general a greater angular deflection has to be preferred for collimation. To have an idea of the values involved, substituting the primary collimator with a crystal in the present (phase 1) LHC collimation system, an angular kick of about 32 μrad would be required [55]. The channeling deflection angle depends on the product between the crystal length and its bending radius which are adjustable parameters, but their growth reduces the channeling efficiency; in fact a longer crystal increases the dechanneling probability and limits the multipass effect, while the bending radius should be kept far below its critical value (Tsyganov's critical radius, eq. 1.29).

Fig. 2.22 shows the predicted efficiency reduction between a deflection angle of 0.1 mrad and 0.2 mrad; anyway these angles are much larger than the reflection one ($\theta_r \simeq 1.5 \cdot \theta_c$). According to this a single reflection will hardly satisfy the collimation requests (at least in a phase 1 like setup). What helps volume reflection is again its efficiency and angular acceptance: their values should in fact allow multiple volume reflections (schematically shown in fig. 2.23) reaching the deflection needed for collimation.

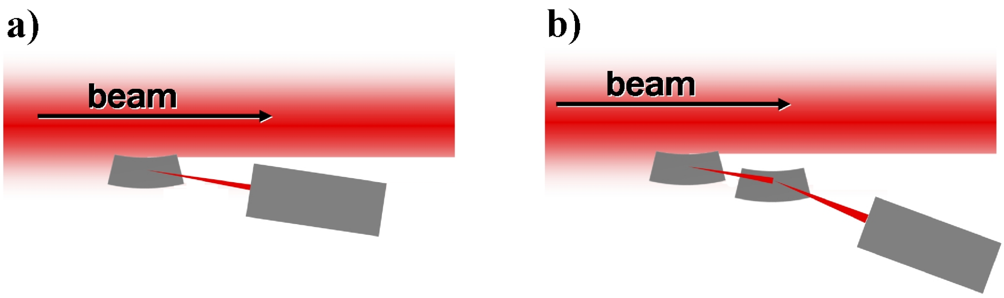

Figure 2.23: Crystal collimation due to volume reflection using a single crystal (a); to increase the final deflection angle of the primary halo different crystals can be put in series (multiple volume reflection) (b).

Characteristics of the deflected beam

Given that the crystal role is to deflect the halo particles with a well known efficiency and a given average angle, also the shape of the crystal outcoming particles distribution should be known to design a powerful collimation system. Any relative small inefficiency is in fact not tolerated.

As anticipated, the final evaluation of a crystal based collimation system will be given through Montecarlo simulations in which all the crystal physics details should be included. The most important information on the deflected beam characteristics are two:

- the rms and the tails structure of the particles distribution originated by the selected effect should be known to design the secondary collimators;
- a precise evaluation of the other competing crystal effects should be performed. If for example a multi volume reflection based collimation is chosen, a small fraction of protons could be volume captured and receive an angular kick in the opposite direction representing a problem that can be solved with some specific absorber implemented in the collimation setup.

In addition to these “crystal physics” topics, there are other important questions which need answers to make the crystal collimation feasible. They are mainly of technical nature and concern: **the crystal alignment**, **the crystal surface specification** and finally **the resistance to the LHC radioactive environment**.

Crystal alignment

For an efficient operation the crystal must be properly aligned with respect to the beam halo direction; the requested alignment precision depends on the angular acceptance. It should approximately be an order of magnitude better to ensure that the maximum allowed efficiency is reached. As demonstrated by the goniometer described in sec. 3.1.3, which has a precision of 1 μrad, this is an affordable technological task.

A comparison between channeling and volume reflection can be done. The first one has a smaller angular acceptance requiring a greater precision and realignment following every beam halo change in direction (which can happen during the accelerating phase). The second one, having a larger acceptance, needs a smaller precision and it is less sensitive to the beam variation, although the possibility of using multiple reflection requires an additional alignment between the different crystals which is under study (the first attempts are shown in chap. 4). It is worth mentioning that a conventional collimation system presents similar problems of alignment accuracy; for example in the LHC collimation system the primary collimator, 1 m long, should be aligned with an accuracy of 20 μrad [54].

Surface specification

The roughness of the crystal surface is usually modelled as a thin amorphous layer where the crystal lattice presents imperfections and channeling and other crystal effects have a very small probability to happen. This thin amorphous layer is not negligible because the average impact parameter on the primary collimator is usually very small, 100-200 nm [56] in the present LHC collimation setup. If a crystal substitutes the primary collimator, many particles impinging on its entry face will scrape its surface and will cross an amorphous-like target instead of a crystal deflector.

This could appear hopeless but halo particles have a “natural” drift velocity of 2 nm per turn (the interaction with the amorphous layer can increase it) which increasing the impact parameter every turn eventually allows the particle to be deflected by the crystal. In other words, it is a specific application of the multipass effect. The presence of a superficial amorphous layer on the crystal surface has been considered in the multipass channeling simulation developed for LHC [54] to evaluate its impact on the efficiency. Fig. 2.24(b) shows the simulated efficiency as a function of the amorphous layer thickness; a smaller thickness corresponds to a greater efficiency in a predictable manner but thanks to the multipass effect the presence of the amorphous layer is not so important. In any case the technique developed for the crystal surface treatment which involves both mechanical polishing and chemical etching (see fig. 2.24(a)) can produce a crystal surface with imperfections below 100 nm [57]. This is a great result especially if compared with the requirements of the present LHC primary collimators which should have a flat surface with an accuracy (nonflatness) of 10 μm.

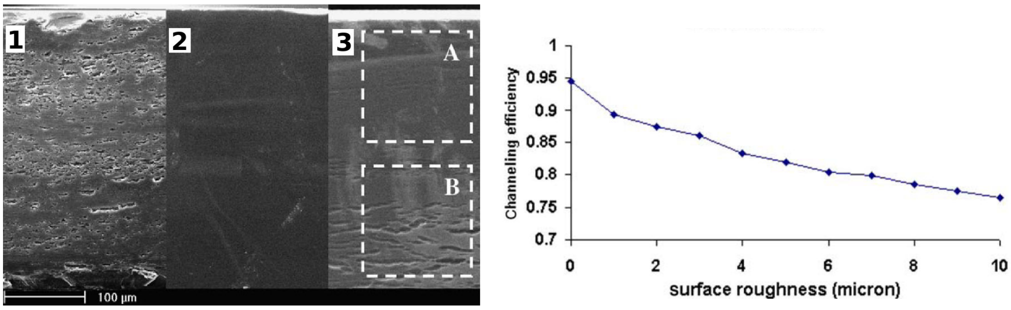

(a)

(b)

Figure 2.24: a) Images of a silicon crystal surface: 1) after the cut (diamond blade); 2) after mechanical polishing; 3) after chemical etching (A and B underline a smooth zone and one with densely distributed cracks) [58]. b) Simulated channeling efficiency as a function of the crystal surface roughness (amorphous layer width).

Radiation hardness

As well as any standard collimator, a crystal should resist to the energy deposited by the particles which could cause thermal shock, radiation damage and eventually the reduction of the crystal life intended as an early deterioration of its deflecting power. Experimental data show that crystals can resist to a high intensity particle flux for short times which emulates possible abnormal collimation situations and that they maintain their properties after having received a high radiation dose integrated on a long time of operation. The ability to withstand a high beam intensity was tested at IHEP [30] where a 5 mm long crystal was exposed for several minutes to the entire circulating beam (10^{13} 70 GeV protons) resulting in 10^{14} proton hits (taking into account an average number of turns per particle estimated with the Montecarlo simulation) in spills of 50 ms every 9.6 sec. After this exposure which corresponds to an instant dump of 1000 LHC bunches, the crystal was tested in an external beam. The deflected beam observed with photoemulsions (fig. 2.25) was normal, without breaks or significant tails produced by dechanneled particles.

Information on the crystal lifetime in a radioactive environment comes from

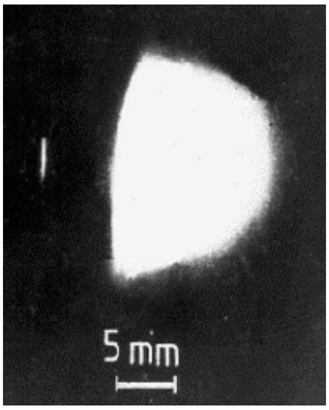

Figure 2.25: Photograph of the deflected (left) and incident (right) beams as seen downstream of the crystal in an external beam test. No damage is evident [30].

experiments that have operated with crystals for years. The CERN experiment NA48 [33] for example showed that at the achieved irradiation of $5{\cdot}10^{20}$ protons/cm^2 the crystal lost only 30% of its deflection efficiency which means $\sim$100 years lifetime in the intense beam of the NA48 experiment. Similar results are recorded by the IHEP extraction beamlines [59] proving that crystals can stand high radiation doses without being damaged.

Chapter 3

The September 2006 beam test

The experiment described in this chapter was performed to improve the understanding of the interaction of ultra relativistic protons with bent crystals. Different bent crystals were tested on the H8 external SPS beamline (sec. 3.1.1) with a 400 GeV/c proton beam. The crystals were designed and bent to provide homogeneous curvature radii and small silicon thicknesses in the beam direction; they belong to two types according to their geometrical and bending features: the strip crystals and the quasimosaic ones.

These designs, which from the technological point of view are rather new, were tested at the IHEP laboratory (sec. 1.2.3 and sec. 2.2.1) with encouraging results: the volume reflection was detected for the first time [27] and unprecedented channeling extraction efficiencies were recorded [30]. The experiment on the H8 beamline had the task of investigating the behaviour of the crystals at high energy, providing precise measurements especially for the volume reflection effect.

This purpose was achieved through an innovative experimental approach in the crystal channeling field. The past channeling experiments used integrated beam profile measurements and the information from the accelerator control detectors to estimate the deflection angles and the efficiencies of the various crystal effects. The aim of this experimental apparatus was instead the reconstruction of the single particle track so that a direct measurement of the particles outcoming direction from the crystal is obtained; moreover the angular information can be correlated with the impact position on the crystal surface provided by the detector placed near the crystal.

This chapter will describe the experimental setup from the beam and the detector point of view underlining their pros and cons. The last part of the chapter is dedicated to the description of the crystal features and of the experimental procedure followed to test them.

3.1 Experimental setup

The experimental setup (shown in fig. 3.1) reflects the will to achieve a versatile and fail proof experimental apparatus; the presence of many detectors of different kinds ensures both rapidity and precision with a high reliability provided by the redundancy (sec. 3.1.2). The particle trajectory is reconstructed by the silicon microstrip detectors placed upstream (near the crystal) and downstream in another experimental hall at a distance of about 70 m from the crystal.
Two independent silicon tracking systems are present; they are both based on detectors originally designed for space missions, the AGILE satellite (sec. 3.1.2.1) and the AMS experiment [60]. The analysis presented in the next chapter is based on the information from the AGILE detectors.
The silicon detectors provide precise measurements while a fast detection of the crystal orientation is obtained thanks to a high rate gas chamber (sec. 3.1.2.2). Both the silicon detectors and the gas chamber are triggered by a set of scintillators.

The alignment of the crystals with respect to the beam is provided by a goniometric system which has a precision of about an order of magnitude higher than the Lindhard critical angle (sec. 1.1.1) computed at the experiment energy ($\theta_c \sim 10\ \mu$rad).

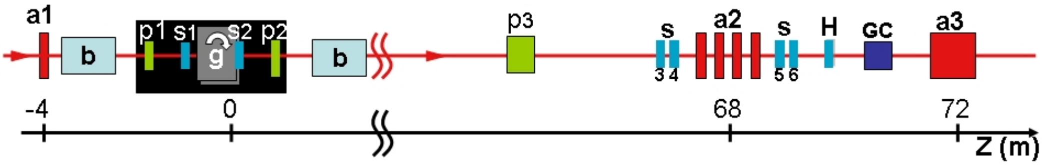

Figure 3.1: The experimental setup: (a1) the upstream AGILE detector -first module-; (b) horizontal bending magnet; (p1) first AMS silicon detector; (s) scintillator; (p2) second AMS silicon detector; (p3) downstream AMS silicon detector; (s) scintillator; (a2) downstream AGILE silicon detector -the silicon chambers-; (s) scintillators; (gc) gas chamber; (a3) downstream AGILE silicon detector -minitracker-.

3.1.1 The beam

The H8 external beamline is located in the North Area of the CERN SPS. The experiment used a 400 GeV/c primary proton beam emitted in spills of 4.8 s every 16.8 s. The nominal intensity, which is about 2×10^{12} protons per pulse, was reduced to about 5×10^4 during the experiment.

The beam spot diameter at the crystal has been measured with the silicon microstrip detectors to be about 1 mm FWHM; fig. 3.2 shows the beam profile measured by the AGILE first module placed about 4 m before the crystal. The shape of the beam is due to the collimators used to reduce the intensity.

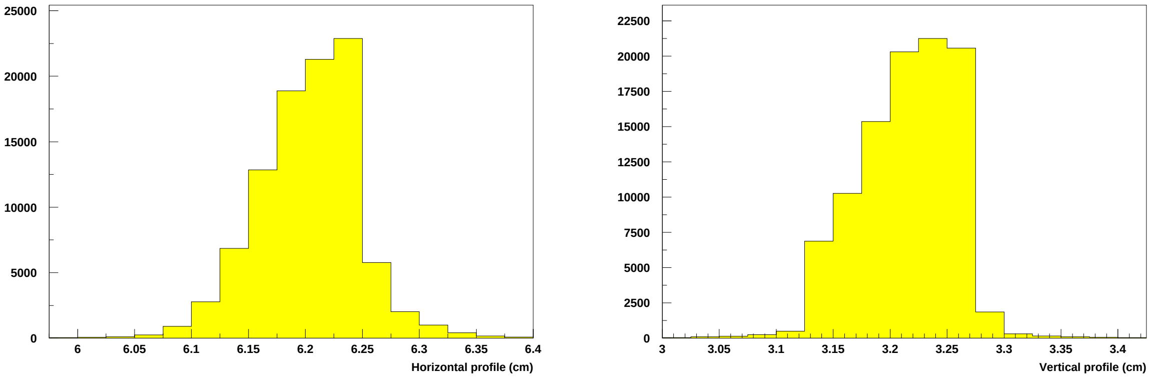

(a) (b)

Figure 3.2: Beam profile measured by the AGILE detector placed 4 meters before the crystal: (a) in the horizontal direction, (b) in the vertical one.

The beam divergence has been measured in dedicated runs without the crystal; fig. 3.3 shows the beam profile (in the horizontal direction) measured with the AGILE silicon chambers and the divergence beam profile that is the angular distribution of the beam particles reconstructed with the first module and the silicon chambers information following the procedure described in sec. 4.1. The spread of the divergence distribution (σ=9.28 μrad) reflects the beam divergence and its widening due to multiple scattering on the material along the beamline. The multiple scattering contribution has been estimated to be about 3.5 μrad. Subtracting in quadrature this contribution gives a beam divergence at the crystal of about 8.6 μrad, which is larger that the value of 3 μrad as expected from the accelerator experts simulation of the beamline.

3.1.2 The detectors

The detectors of the experimental apparatus can be divided in three classes: the silicon microstrip detectors to perform high resolution measurements; the gas chamber for the fast detection of the channeling condition and the scintillators which provided the trigger.

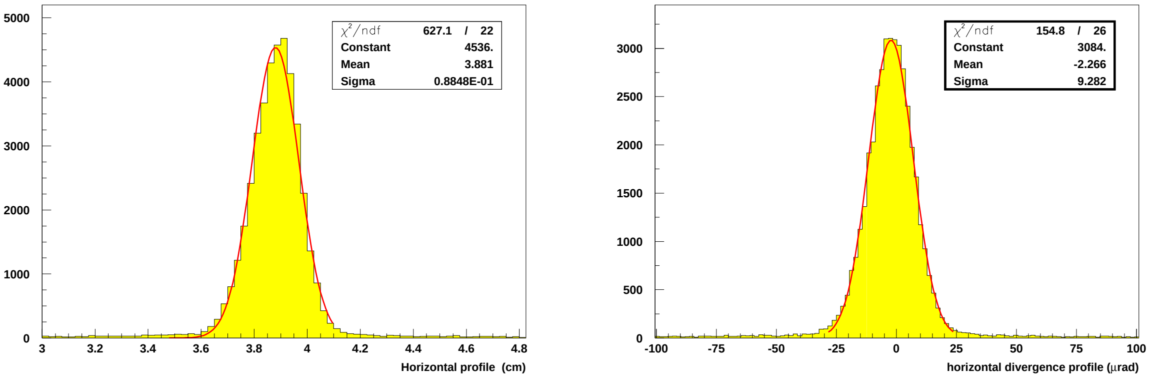

(a) (b)

Figure 3.3: (a) The beam profile in the downstream region measured by the silicon chamber, in the horizontal direction. (b) The beam divergence reconstructed using the first module and the silicon chamber information.

3.1.2.1 AGILE silicon microstrip

Fig. 3.4 shows the position of the AGILE detectors with respect to the crystal. They are silicon microstrip detectors originally designed for the AGILE satellite [61][62]. In total there are 20 silicon tiles organized in 10 x-y assemblies. The dimension of each silicon tile is 9.5 $\times$9.5 cm^2 and the thickness is 410 μm; the physical strip pitch is 121 μm while the readout one is 242 μm thus a floating strip scheme has been adopted. The detectors are AC coupled with polysilicon resistors for the biasing. Each tile is readout by three low noise self triggering ASICs (TAA1 by Ideas, Norway); the readout is a multiplexed one with a maximum rate of 10 MHz. The detectors are organized in 3 separate measuring "stations":

- the "first module" which is located in the upstream region, before the first bending magnet; it is a single x-y detector;

- the downstream region, which is located at about 70 m from the goniometer, consists of two measuring "stations": the "silicon chambers" (fig. 3.5), a group of 4 x-y silicon tiles and the "minitracker" which is a small scale prototype of the AGILE silicon tungsten tracker with 6 x-y planes as shown in fig. 3.6.

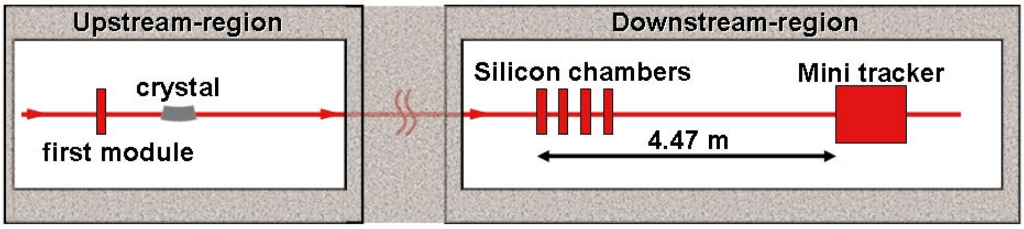

Figure 3.4: A schematic diagram showing the AGILE microstrip detectors position with respect to the crystal.

Figure 3.5: The 4 x-y silicon chambers in the downstream region.

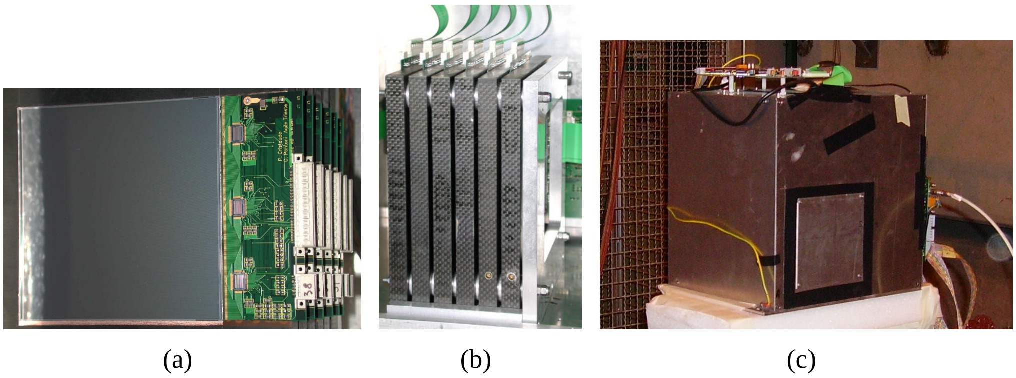
(a) (b) (c)

Figure 3.6: The minitracker: (a) the single tile and its readout ASICs (TAA1); (b) the 6 x-y planes; (c) its box.

3.1.2.2 Gas chamber

A detector for planar channeling studies, capable to withstand high particle rates and working in self-triggering mode, has been assembled using a parallel-plate gas chamber [63]. In the H8 data taking this detector is used for the fast angular crystal scans, to get information on their orientation with respect to the beam and to provide the online characterization of the crystals under investigation.

The detector (fig. 3.7) consists of two parallel flat electrodes assembled with a uniform gap and installed within an aluminum frame of 25 (height) × 110 (width) × 175 (length) mm^3, filled with a gas mixture (70% Ar + 30% CO2) at atmospheric pressure. The anode electrode is arranged on a glass-ceramic plate covered by a Ni-Cu-V multi-layer and treated photo-lithographically to produce 64 strips, 150 μm wide, with a 200 μm pitch. The cathode electrode is made of a low-resistance sputtered silicon plate of $0.5 \times 10 \times 50\ \mathrm{mm}^3$.

Due to the relatively small active area, the detector was mounted on a movable support, with a step precision of 4 μm and a total range of about 50 mm for both the horizontal and vertical movements.

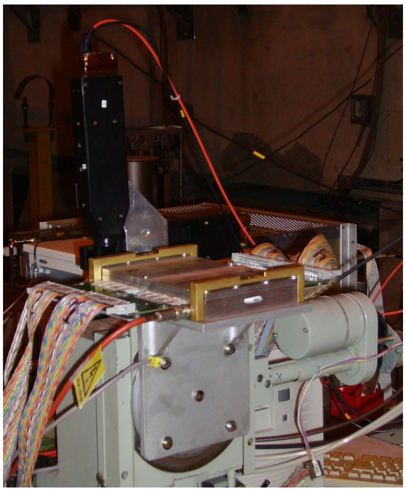

Figure 3.7: A photo of the gas chamber during the experiment.

3.1.2.3 Scintillators

Two thin scintillation counters were installed on the granite table (S1, 100 μm thick in the horizontal direction) and on the upper linear stage of the goniometer (S2, 80 μm thick). They were used to define the exact beam position with respect to the crystals.

A pair of identical scintillators (S3-S4: $100\times100\times4\ \mathrm{mm}^3$) was placed downstream of the AMS detectors and used to define the trigger for the silicon detectors. Two additional scintillators were used in the downstream detector region: a 100 μm thick (S5) and a 2 mm thick one (S6), mounted on movable supports for a redundant measurement of the beam divergence and profile.

A scintillating hodoscope (H), made of 16 vertical strips with a total sensitive area of 3.2×4.0 cm^2, was used for beam monitoring. Each strip is 2 (horizontal) $\times$ 4 (along beam) $\times$ 40 (vertical) mm^3. The hodoscope was used during the data taking to provide fast information on the crystal alignment and the beam stability.

The scintillators conditioning and readout electronics is based on NIM and VME commercial modules. The signals are sent to a programmable trigger logic unit, a custom module (INFN Ferrara) which generates the trigger signals for the silicon microstrip detectors, receiving as an input the discriminated signals from all the scintillators and the hodoscope, in addition to the busy signals from the silicon stations data acquisition and the SPS accelerator signals (such as the spill signal).

3.1.3 The goniometer

The study of channeling phenomena requires a very accurate angular alignment of the crystals with respect to the proton beam. In sec. 1.1.1 it was shown that the critical angle for channeling (that is its angular acceptance) is of the order of 10 μrad for 400 GeV/c protons in silicon and the beam divergence in the H8 beamline was expected to be about 3 μrad thus an alignment system with the precision of $\sim$1 μrad is necessary to perform a detailed studied of the channeling phenomena. Moreover, such a precision is more than enough to study the volume reflection which has a larger angular acceptance and less stringent requirements on the alignment.

A high precision goniometric system has been implemented for the experiment described in this chapter (a scheme (a) and a photo (b) are shown in fig. 3.8). Besides the angular alignment, this system is designed to allow the precise positioning of the crystal on the beam. Therefore it consists (as shown in fig. 3.9) of different stages:

- a linear one to put the goniometer on the beam (52 mm range);
- a rotational one to align the crystal with respect to the beam (360° range);
- another linear stage is designed to put the crystal holder on the rotational axis (102 mm range);
- on the top two crystal holders can be mounted so that, through a 180° rotation of the goniometer, two crystals can be analyzed without stopping the beam.

The two translational stages have an accuracy of 1.5 μm, a bidirectional repeatability of 2 μm and a resolution of 5 μm over the whole range; the rotational

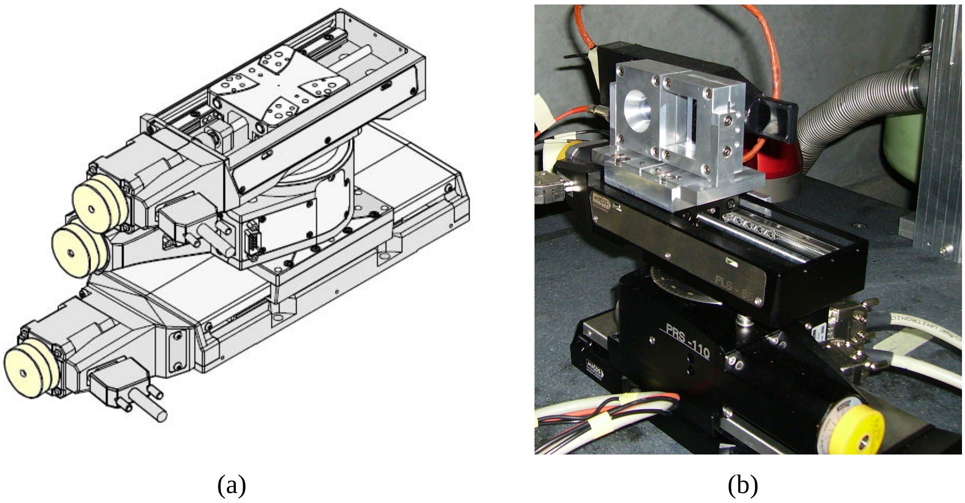

(a) (b)

Figure 3.8: (a) A schematic of the goniometric system; (b) a photo of the system during the operation in the H8 beamline.

one has a 1 μrad average accuracy, 1 μrad repeatability and 0.25 μrad resolution. The accuracy is defined as the difference between the real and the nominal position of the stages; the repeatability is the spread of the stage positions in case of repeated motion to the same value. The resolution is defined as the smallest possible step of the translation/rotation movement.

In order to improve the mechanical stability of the goniometer and to precisely define its relative position with respect to the beam, the whole system was installed on a precisely machined granite table.

The readout of the angular and linear stages position is performed by optical encoders; the system is remotely controlled via PC and the information from the encoders is stored in dedicated data files by the data acquisition system.

3.1.4 The crystals

Two different types of crystals have been used in the experiment: the strip and quasimosaic which are characterized by a different bending technique. Fig. 3.10 shows a strip crystal mounted on its holder (a) and a quasimosaic one (b).

3.1.4.1 Strip crystals

The name strip comes from the shape of the crystal which is chosen to exploit the anticlastic curvature in order to obtain a uniform bending in the beam direction. Fig. 3.11(a) shows the curvature scheme of a strip crystal: a mechanical holder

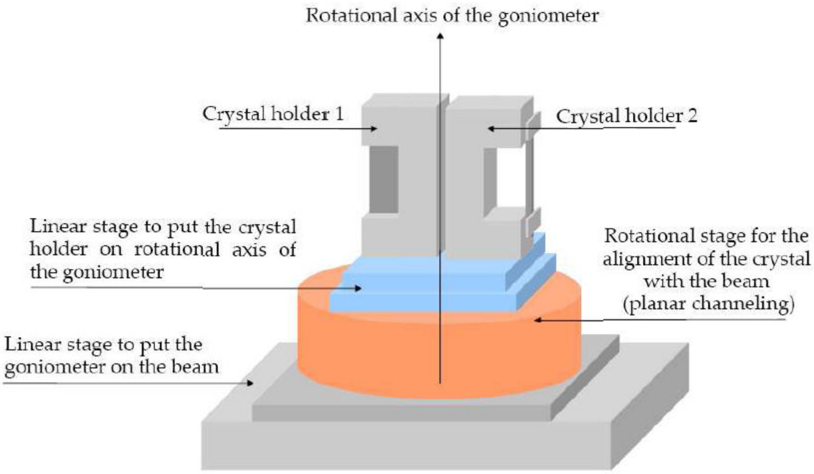

Figure 3.9: A scheme of the different stages of the goniometer.

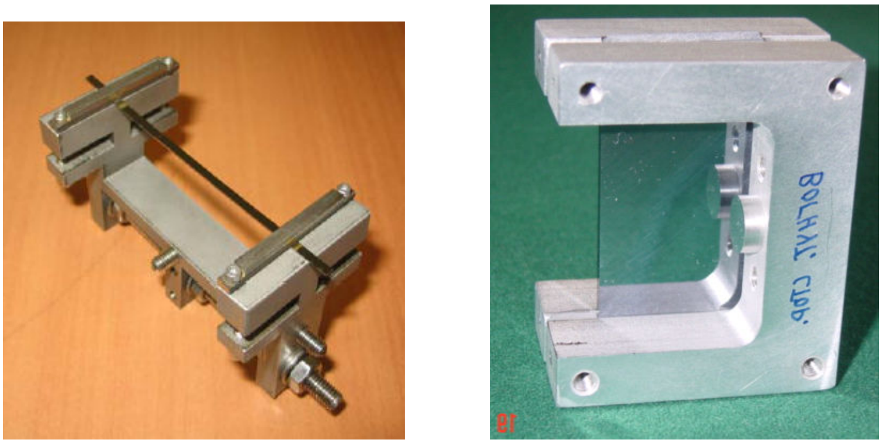

(a) (b)

Figure 3.10: Two examples of the crystals used during the experiment: (a) a strip crystal ; (b) a quasimosaic one.

bends the strip (fig. 3.11(a)) along its major direction producing a primary curvature (indicated with P_c); the anticlastic forces generate a secondary curvature (indicated with A_c) which is used to deflect the proton beam.

The silicon strips used in the experiment have been manufactured at the Sensors and Semiconductors Laboratory at Ferrara University in collaboration with IHEP. The strip crystals are obtained dicing the silicon wafers with a fine grane-blade in order to induce minimal lattice damages; the residual lattice damage has been removed through wet isotropic chemical etching in acid solutions [64]. The

Crystal	orientation	length (mm)	area (mm^2)	bend radius (m)
ST4	(110)	3.0	0.9×70	18.47
ST1	(111)	1.0	0.2×70	11.17
ST2	(111)	1.85	0.5×70	8.55

Table 3.1: Geometrical parameters of the analyzed strip crystals; length corresponds to the *z* direction and area to the *xy* ones, defined in fig. 3.11(b). The analysis of the ST4 crystal is presented in chap. 4.

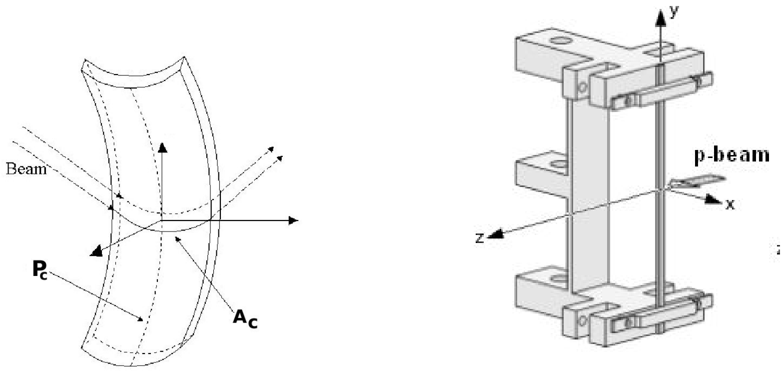

(a) (b)

Figure 3.11: (a) The bending principle of the strip crystals. (b) A scheme of the strip crystal bending device (the crystal holder).

surface characterization with the Rutherford Back Scattering technique in channeling mode demonstrated the quality of the etched surfaces [65]. Table 3.1 summarizes the geometrical characteristics of the strip crystals used during the experiment.

3.1.4.2 Quasimosaic crystals

The second type of crystals has been prepared exploiting the elastic quasi-mosaicity effect. The crystals are prepared in form of small plates in a way that the (111) crystalline planes are normal to the large face of the crystal itself and parallel to its edges (as shown in fig. 3.12(a)). The bending device (shown in fig. 3.12(b)) exploits again the anticlastic effect: it is designed to bend the crystal in the *yz* plane conferring it the principal curvature (indicated with ρ in fig. 3.12(b)); the anticlastic forces produce a secondary curvature (indicated with ρ' in fig. 3.12(b)) in the *xz* plane which causes the quasimosaic curvature of the (111) atomic plane. The quasimosaic effect is due to the crystal anisotropy which depends on the selected crystallographic planes and on the orientation of the other crystalline direction with respect to the crystal plate. Fig. 3.13 shows the condition under which the quasimosaic effect takes place.

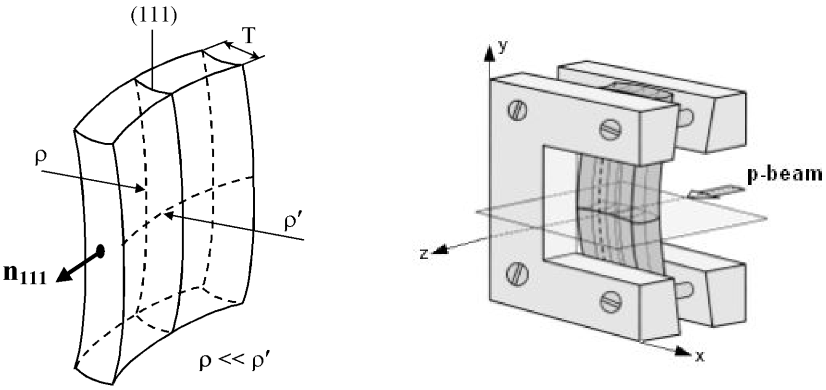

(a)

(b)

Figure 3.12: (a) The bending principle of the quasimosaic crystals. (b) A scheme of a quasimosaic crystal bending device (the crystal holder).

The quasimosaic crystals used in the experiment were prepared in PNPI (Petersburg Nuclear Physics Institute, Gatchina) as described in [66]; table 3.2 lists their geometrical characteristics.

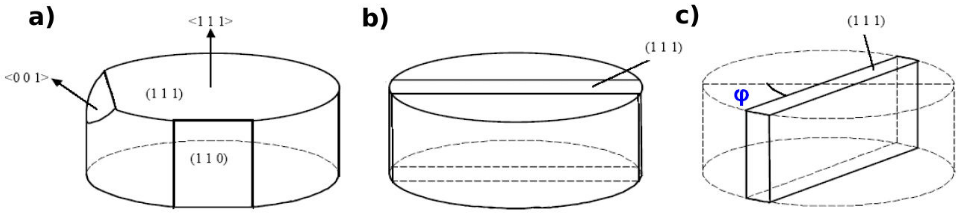

Figure 3.13: a) The silicon ingot before the cut with the interesting crystalline planes and axis indicated; b) a portion of the ingot to be cut is indicated; the corresponding crystal will not present the quasimosaic effect; c) if the cut is performed misaligned with respect to the (001) axis direction the quasimosaic effect will be present.

3.2 Experimental procedure

The standard experimental procedure to analyze a crystal is the following:

Crystal	orientation	length (mm)	area (mm^2)	bend radius (m)
QM2	(111)	0.84	30×58	12.25
QM1	(111)	0.93	30×58	11.43

Table 3.2: Geometrical parameters of the analyzed QM crystals; length corresponds to the z direction and area to the xy ones, as defined in fig. 3.12(b). The analysis of the QM2 crystal is presented in chap. 4.

- the crystal is mounted on its holder and then on the goniometer;
- the crystal is pre-aligned with a laser beam (the procedure is described in fig. 3.14(a)) with a precision of about 300 μrad;
- the crystal is placed on the beam trajectory with a lateral scan performed with the transversal movement of the goniometer (the procedure is described in fig. 3.14(b));
- given the critical angle ($\sim$ 10 μrad), the laser pre-alignment precision ($\sim$ 300 μrad) is not enough to detect the channeling angular position; for this reason a fast angular scan with the gas chamber is performed;
- the gas chamber defines, in a short time, the precise channeling angular position and the total angular range to be measured with higher statistics and higher precision with the silicon detectors; a typical high statistic angular scan is performed with a goniometer angular step of about 3 μrad collecting about 45000 events per step with the AGILE detectors (150000 in the case of AMS);

The scan angular range is chosen in a way that both the channeling and the volume reflection are probed over their whole angular acceptance. Fig. 3.15 shows the beam profile (recorded by the silicon chambers) as a function of the goniometer angle (during the ST4 crystal scan); the plot is divided in four angular regions:

1. the “amorphous” position, where the crystal effect on the beam is only a multiple scattering contribution;
2. the “channeling” position, where the channeling peak appears and the reflection starts; note that the area between the channeling peak and the reflection one is filled by the dechanneled particles;

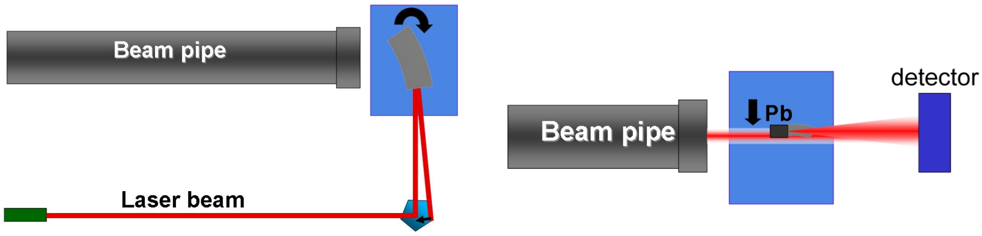

(a) (b)

Figure 3.14: a) The laser pre-alignment technique: a laser beam is aligned with respect to the beam pipe and projected at 90° towards the crystal surface with a penta prism; the crystal reflects the laser beam so that rotating it with the goniometer, once the incoming and the reflected beam overlap, the crystal is perpendicular to the proton beam; at this point a 90° rotation of the crystal aligns it for channeling. b) The lateral scan procedure to put the crystal in the beam: a Pb strip is put on the crystal which is moved in the transversal direction with respect to the beam until an increased multiple scattering is detected by the gas chamber; at this point the Pb strip is removed and the crystal is properly placed.

3. the "reflection" position, where the channeling peak disappears and part of the beam is reflected (as it will be shown, the whole beam crosses the crystal); the diagonal line which connects the channeling peak with the amorphous one is due to the volume captured particles;

4. the crystal is back in the amorphous position.

Fig. 3.15 is the sum of the beam profiles recorded in the downstream region by one of the silicon chambers as a function of the crystal rotation angle. The standard analysis is performed through gaussian fits of the amorphous, reflected and channeled peaks, if present in the beam profiles.

This fit allows to compute the crystal angular parameters such as the channeling angle (crystal bending angle, $\theta_c = \theta_b$), the channeling peak width (σ_c), the reflection angle (θ_r) and the increase of the main peak width during reflection ($\sigma_r - \sigma_a$, where σ_a is the width of the amorphous beam).

Fig. 3.16(a) shows an example of a gaussian fit of the channeling peak; the beam profile is taken from the ST4 scan (fig. 3.15 region (2)). The values from the fits of the different profiles are then summarized in plots like the one shown in fig. 3.16(b) where the main value of the channeling peak is reported.

Fig. 3.17(a) shows the gaussian fit of a reflected peak in a beam profile taken from the ST4 scan (fig. 3.15 region (3)); since the crystal is smaller than the beam, both the reflected and the "unperturbed" beam are present, so the fit is the sum of two gaussian functions. The main gaussian peak trend is shown in fig. 3.17(b).

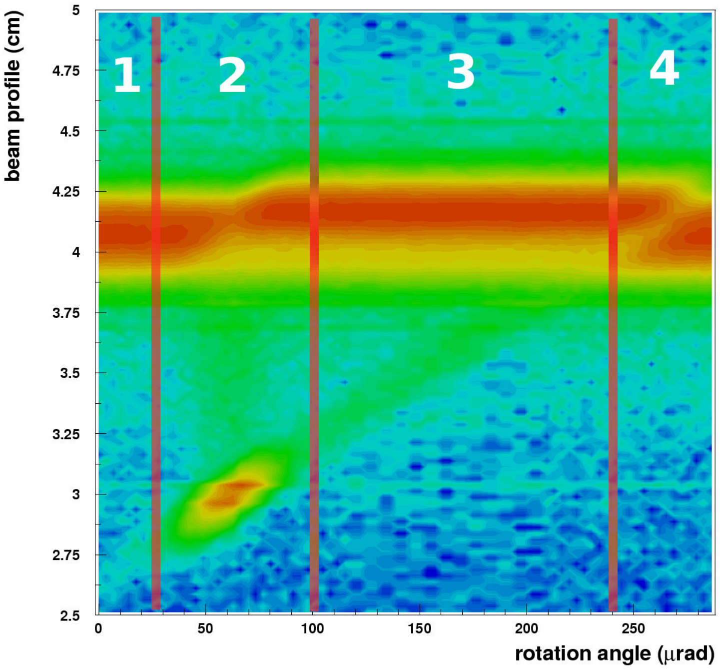

Figure 3.15: Bidimensional plot of the ST4 crystal scan (logarithmic scale): on the horizontal axis the crystal rotation angle, on the vertical axis the beam profile in the downstream zone, reconstructed using the information from a silicon chamber (the 2^{nd} one with respect to the beam).

The channeling angle corresponding to the different goniometer positions is computed from the distance difference between the main peak amorphous position (determined in fig. 3.17(b)) and the channeling peak one divided by the distance between the chamber and the crystal. The bending angle of the crystal is the channeling angle value which corresponds to the goniometer position in which the channeling is more efficient (the procedure is described in sec. 4.4). In the same way the reflection angle is the difference between the reflected peak position and the amorphous one.

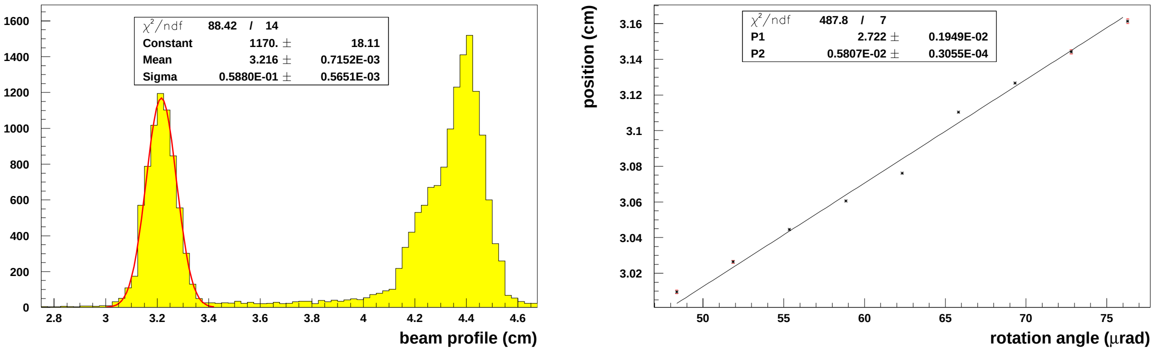

(a) (b)

Figure 3.16: (a) A frame of the ST4 crystal scan during channeling (fig. 3.15 region (2)); the channeling peak is fitted with a gaussian. (b) The channeling peak trend as a function of the goniometer angle.

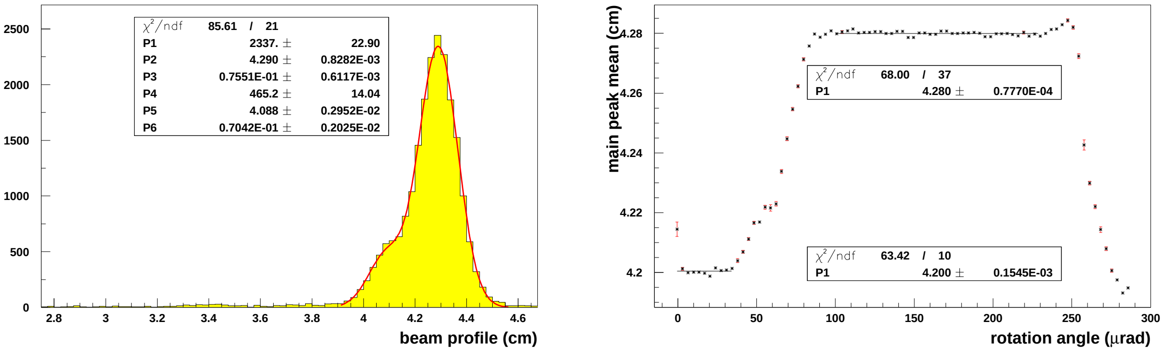

(a) (b)

Figure 3.17: (a) A frame of the ST4 crystal scan during reflection (fig. 3.15 region (3)), the main peak is fitted with the sum of two gaussians. (b) The main peak trend (biggest gaussian) as a function of the goniometer angle; the fit with the constant function gives an average displacement of 796 ± 2 μm which corresponds to an angle of 11.53 ± 0.02 μrad.

Chapter 4

The September 2006 results

This chapter presents the analysis work performed on the data collected in the September 2006 run with the setup described in the previous chapter.

The analysis starts with the research of the most efficient way to exploit the information from many detectors (sec. 4.1) leading to the reconstruction of the divergence profile of the protons which have crossed the crystal.

Two different analysis methods will be described: the one based on the beam profile of a single detector and the one exploiting the angular information obtained reconstructing the tracks. This thesis work is based on the second method, whose advantages will be clearly demonstrated with several examples.

The presence of a high resolution detector near the crystal allows, for the first time, the analysis of the crystal properties with respect to the different regions of the crystal surface: the method used to define the section of the beam which impinges on the ST4 crystal (which is a 900 μm strip) is presented in sec. 4.2 while in sec. 4.3 an analysis of the crystal effect as a function of the proton impact point on the crystal itself in the vertical direction is described. In fact, both the quasimosaic crystal and the strip one seem characterized by a small rotation of the surface with respect to the vertical position which has been interpreted as a torsion of the crystal due to the forces applied by the holder to obtain the curvature.

The last part of the chapter is dedicated to the method developed to compute the efficiencies of the different crystal effects (sec. 4.4).

The analysis has been performed on the crystals which have been tested after the first module installation, which are a strip crystal (ST4), a quasimosaic one (QM2) and a double crystal (QM1 and QM2 in series) which provided a double reflection.

Among the various results presented in this chapter the evidence of a very efficient volume reflection (in agreement with the theoretical and simulation expectations) is the most significant result of this experiment. The measurement performed with the two aligned crystals suggests the possibility to develop multi reflectors to exploit the volume reflection large efficiency and large angular acceptance while at the same time obtaining an adequate deflection angle.

4.1 Track reconstruction

As already said, two different analysis methods have been studied: the beam profile and the reconstructed angle. The first one is based on the information of a single silicon tile. The attention was focused on the beam profile variation caused by the insertion and the rotation of the crystal. The beam dimension at the goniometer position is small compared with its dimension in the downstream zone (about 10 times smaller, see sec. 3.1.1) so, once it is divided by the distance from the crystal, the beam profile roughly corresponds to its divergence profile. The first published results [67] have been analyzed using this first method.

The analysis presented in the next sections is based on the second method which uses the information from the different silicon modules to improve the measurements precision; this method can be divided in 3 steps:

- detectors alignment;
- reconstruction of the proton position in the downstream region;
- computation of the protons angle using the information of the upstream detector.

To use the information from many detectors, their relative positions should be known at least with a precision of the order of their spatial resolution which is a hard task to achieve with just external measurements (the ones performed by the surveyors) especially when the detectors are very distant as in this case. The difficulty can be overcome exploiting the information given by the detectors themselves when hit by the beam. The alignment procedure, in principle, can be very complex as the position of any silicon x-y couple is determined by 5 parameters; so to know the relative position of the AGILE detectors (for the time being only the downstream silicon chambers and minitracker are considered, that is 9 detectors) $5 \times 8 = 40$ parameters are needed. The task can be simplified taking into account a smaller number of parameters which added to the information from the external measurements allow to reach the desired precision, as it was done in this case.

The 5 parameters which determine the position of one detector can be chosen as: three coordinates that define the position of one point of the detector in space (two describe the transversal alignment with respect to the beam (horizontal and vertical coordinate) and the other one the longitudinal alignment) and two parameters for the rotation angles around the vertical and the horizontal axis.

In the alignment of the AGILE detector the number of parameters has been reduced from 40 to 18: the two rotation angles around the vertical axis (one for the silicon chambers and one for the silicon minitracker) and 16 parameters which define the relative transversal alignment.

The 8 parameters concerning the longitudinal alignment have been neglected because the possible error on the external measurements of the distance between the detectors ($\Delta z \simeq 0.15$ mm) when propagated on the transversal plane taking into account the largest measured angle (that is the channeling one of about 150 μrad) gives a transversal error negligible with respect to the detectors resolution ($\Delta x = \Delta z \cdot \theta_{max} \simeq 2$ μm).

As far as the angular parameters are concerned, the rotation angles of the single detectors have not been considered because the mechanical supports ensure the fact that the single modules are parallel to each other; only the rotation angles of the two detector blocks have to be adjusted and among these only the one around the vertical axis could influence the measurement as the bending due to the crystal is in the horizontal plane.

Once the interesting parameters have been chosen, the alignment procedure has been performed using a set of data of the unperturbed (without crystal) beam as follows:

- the maximum of the beam profile on the first silicon chamber is taken as a benchmark; in other words the measured points of the other detectors will be shifted in a reference system in which this point is fixed;
- the first detector of the minitracker is shifted in the transversal direction so that the measured beam profile is aligned with the one measured by the first chamber;
- the silicon chambers ensemble and the minitracker one are rotated around a vertical axis placed on the beam profile maximum of the first detector (the first chamber and the first layer of the silicon tracker); the rotation angle is chosen to minimize the offsets of the residuals computed as the measured position on the remaining layers minus the one extrapolated from the track reconstructed using the information from the first module of the two detectors blocks;
- to cancel an eventual offset, an additional shift for each detector is needed so that the residuals are centered in 0;
- this same shift procedure is applied to the vertical residuals.

Fig. 4.1 shows a residual of the silicon chamber after the alignment procedure.

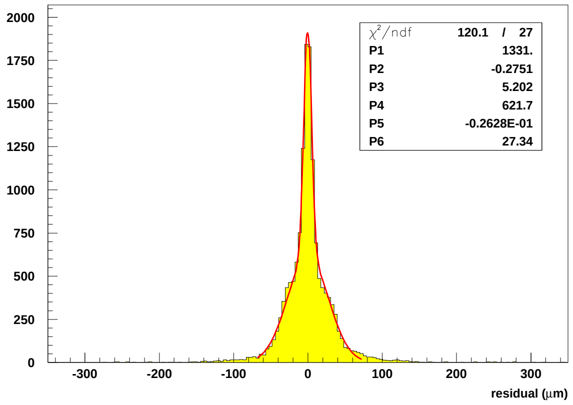

Figure 4.1: The residual of an AGILE microstrip silicon detector (the third silicon chamber crossed by the beam, horizontal direction). The distribution is fitted with the sum of two gaussians with σ=5.2 and 27.3 μrad, the average σ value (weighed on the gaussian areas) is 20.9 μrad.

Once the detectors have been aligned, the second step in the analysis is the reconstruction of the particle tracks, in order to obtain the angle and the position of the proton coming from the crystal. Before performing a linear fit it is necessary to consider the multiple scattering contribution: in particular, the scattering introduced by the silicon chambers on the impact point measured by the minitracker is not negligible with respect to the resolution. For this reason it has been decided not to use the minitracker information in this analysis.

The chambers are very near one to the other so the effect of the multiple scattering in the chambers can be neglected. On the other hand, the expected track angle is very small compared to the chamber resolution (20 μm best value) so that the information from the silicon chambers is not enough to reconstruct the particles tracks with the precision needed to investigate both the channeling and volume reflection effect. Anyway the information of the 4 chambers is used to have a better reconstruction of the particles position in the downstream region exploiting the redundancy to recover eventually dead or noisy strips; a comparison between the beam profile of a single chamber with respect to the one obtained using the information of the 4 detectors is presented in fig. 4.2.

Once the position of the protons in the downstream region is reconstructed, the first module can be considered. It is located about four meters before the goniometer, just before the first bending magnet and can be used to compute the angle of the proton which has crossed the crystal.

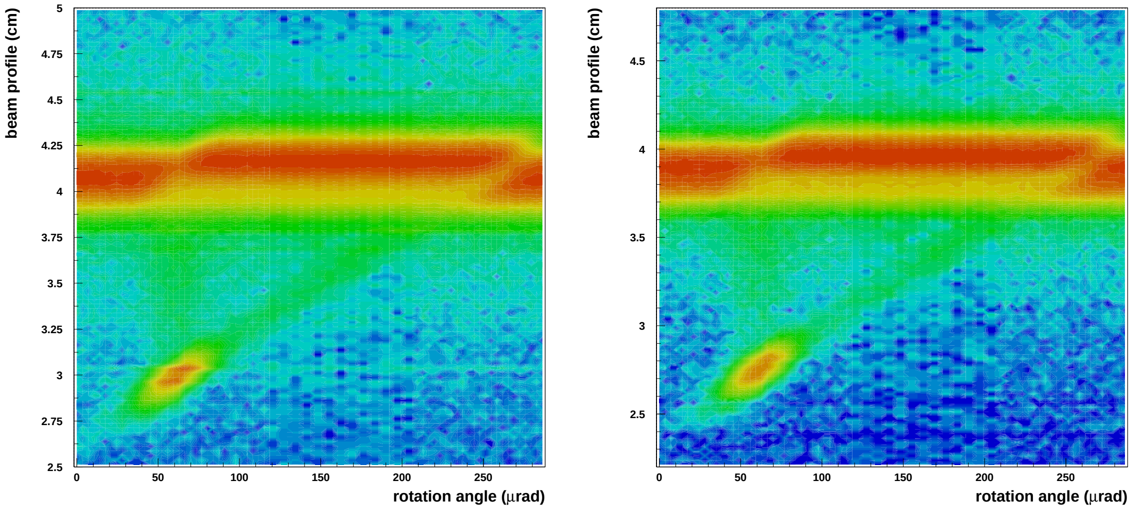

(a) (b)

Figure 4.2: The ST4 crystal angular scan, a comparison between: (a) the beam profile obtained from a single silicon module; (b) the beam profile reconstructed using the information of the 4 silicon chambers.

In the approach which involves the first module information, the beam shape before the crystal is taken into account with the hypothesis that the protons have the same transversal position with respect to the beam core, before the first magnet and at the goniometer. This approximation is based on the fact that the particles trajectories in the dipole magnet are parallel and it is reasonable if the average transversal shift of the protons in the path between the detector and the goniometer is small compared to the spatial beam dimension.

The beam divergence measured without the crystal is about 9 μrad and this number is actually an upper limit as it includes the multiple scattering contribution (detector, air, other) and an eventual contribution of the second bending magnet in spreading the beam itself. 9 μrad means an average transversal shift of 35 μm while the beam profile FWHM is 260 μm so the approximation is acceptable.

This method, if compared to the beam profile one, has at least 3 advantages that will become clear further on:

- better resolution;
- better evaluation of the beam and channeling divergence;
- correction of eventual effects due to the crystal surface.

The next three examples will compare the beam profile method with the reconstructed angle one; the plots are relative to the ST4 crystal at the channeling position.

In fig. 4.3 the beam profile of a single silicon tile is compared with the angular profile obtained using the silicon chambers and the upstream module. The resolution in the second case is better; in fact, in the beam profile a bin corresponds to a readout channel (242 μm) which means 3.48 μrad while in the divergence profile a bin is 2 μrad and no effect due to the strip granularity is evident.

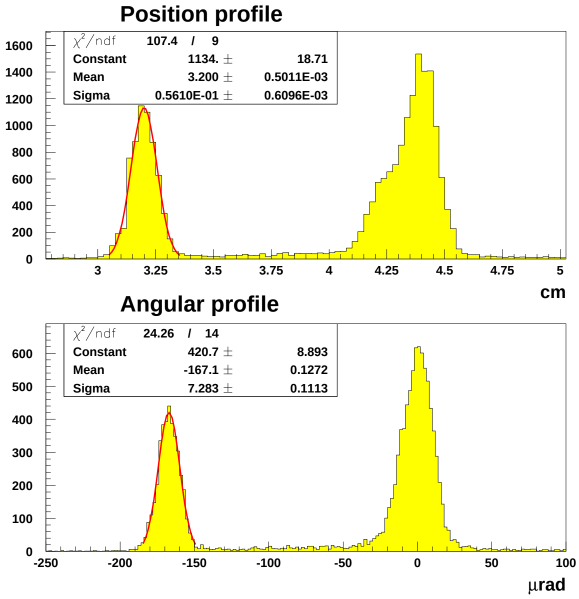

Figure 4.3: Comparison between the gaussian fits of the channeling peak in the beam profile method (top) and in the reconstructed angle one (bottom). Note that: 1) in the first plot a bin corresponds to 242 μm that divided by the distance from the crystal (69 m) gives a value of 3.48 μrad, while in the second plot a bin is 2 μrad; 2) the channeling peak sigma value is 0.56 cm (top) that divided by the distance from the crystal gives a value of 8.06 μrad while its value measured with the first module is 7.283 μrad (bottom).

Fig. 4.3 compares also the channeling parameters obtained from the position profile (top) and the angular profile (bottom): the beam profile method overestimates the channeling sigma of more than 0.7 μrad which corresponds to a systematic error of about 10%.

As said before, the last advantage of the angular method is the correction of eventual effects depending on the proton impact position. If there are regions of the crystal which act in different ways on the beam modifying the beam profile itself and causing systematic effects, they can be removed considering the impact point of the proton on the crystal itself.

Going back to the example this fact will become clearer; in fig. 4.3 the main peak presents a “bump” on the left, corresponding to the part of the beam that doesn’t pass through the crystal. However, while this bump is clearly visible with the beam profile method it seems to be hidden in the beam divergence profile, where it appears only as an asymmetry of the main peak. Fig. 4.4 shows the main peak fit performed with two gaussians in order to evaluate the angular distance between the unperturbed beam and the region of the beam in reflection.

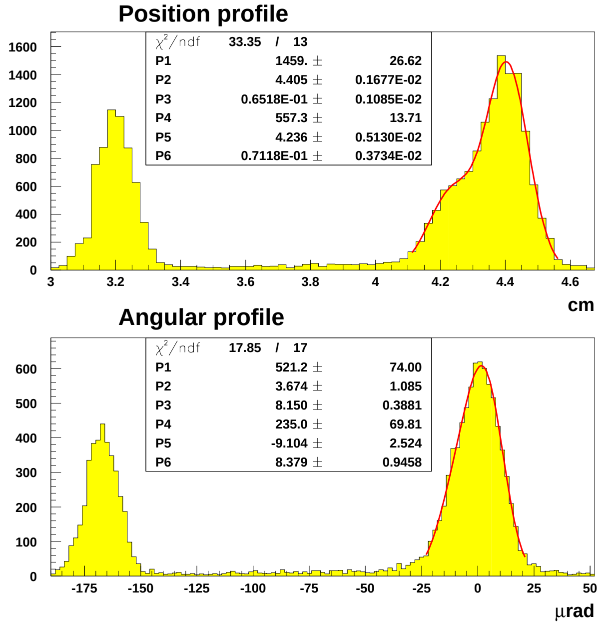
Position profile

Angular profile

Figure 4.4: Fit of the main peak with two gaussians. Top plot: the distance between the two peaks is 0.191 cm corresponding to 27.52 μrad. Bottom plot: the distance between the two peaks is 14.98 μrad.

The angular distance of the two gaussians is different in the two cases: the beam profile method gives a distance of 27.52 μrad while the angular method a distance of 14.98 μrad which is compatible with the reflection angle. It is evident that there is an effect that enlarges this distance only in the beam profile. Fig. 4.5 explains this effect: in the beam profile the distance between the particles which cross the crystal and the unperturbed beam is the sum of the reflection process and the original distribution of the particles in the beam at the crystal. In the beam profile method this second component is neglected (the beam is assumed point-like at the crystal) thus overestimating the reflection angle.

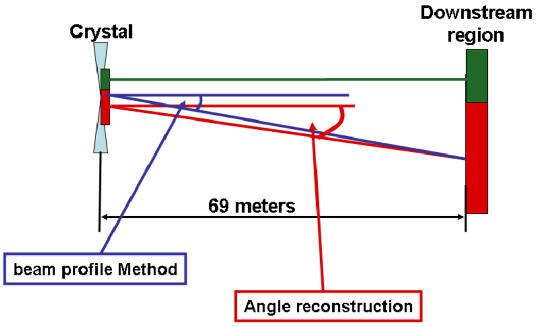

Figure 4.5: This scheme explains why with the beam profile method the angle between the unperturbed peak and the reflection peak appears greater than the one obtained using the reconstructed angle.

4.2 Definition of the ST4 crystal horizontal size

The previous section has shown that the ST4 crystal is smaller than the beam size; this section shows how the effective ST4 area has been defined with respect to the first module position. The following description starts from the observation of a beam profile peculiarity recorded in the ST4 crystal scan.

To extrapolate the reflection and channeling parameters from the beam profile both the channeling peak and the reflection one are fitted with a gaussian function at each angular step. In the case of the ST4 crystal the main peak has two gaussian components when in reflection, the reflected one and the one due to the beam not crossing the crystal; thus the fit is performed only on the reflection part as shown in fig. 4.6(a).

The results of the gaussian fits are shown in fig. 4.6(b). It is remarkable, according to the sigma trend (bottom of the figure), that the beam width seems to decrease when it is in reflection. This strange effect could be an analysis artifact: by means of the fit shown in fig. 4.6(a), when the crystal is in reflection only a part of the beam is considered by the fit while when it is in the amorphous position the whole beam is considered because it is not possible to distinguish two different components. This could explain an apparent beam reduction in width but, as will be demonstrated later on, not its entity.

Fig. 4.7 presents the two dimensional plot of the beam divergence with respect to the proton horizontal position on the crystal. The data are taken from the ST4 crystal scan when it was in the amorphous position.

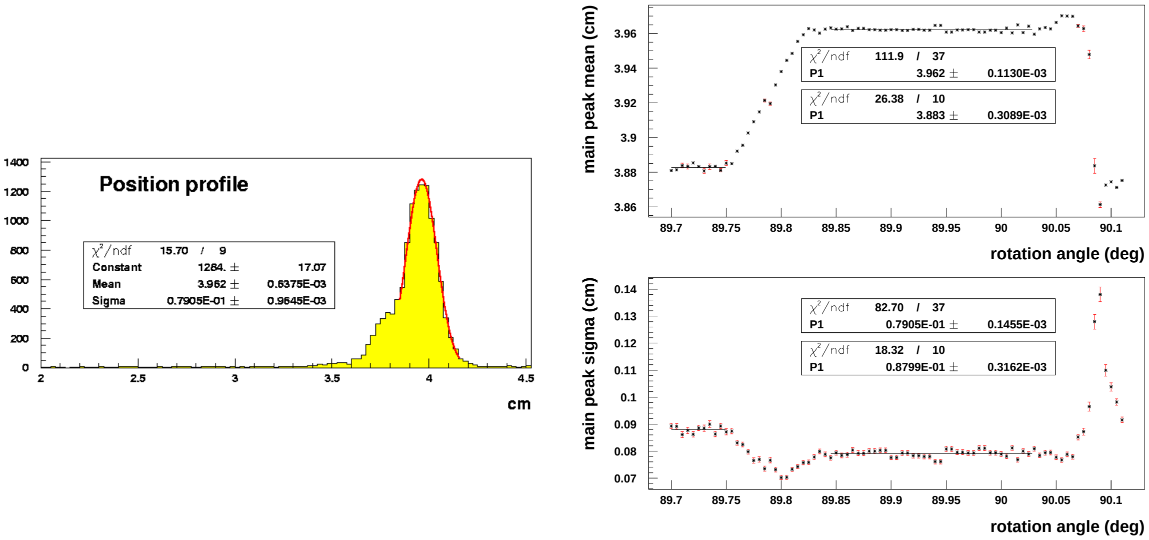

(a) (b)

Figure 4.6: (a) Plot of the beam profile in the reflection position. A gaussian fit has been performed only on the part of the beam that actually crossed the crystal. (b) Results of the gaussian fits (performed as shown in plot (a)) of the beam profile main peak of the ST4 crystal. Top plot: the gaussian mean trend; the amorphous position and the reflection one are fitted with a constant to measure the reflection gap which is 0.0795 ± 0.0003 cm that is 11.42 ± 0.05 μrad. Bottom plot: the gaussian sigma trend; the amorphous position and the reflection one are fitted with a constant to measure the sigma variation between them which is -0.0089 ± 0.0003 cm corresponding to -1.28 ± 0.05 μrad.

Fig. 4.8 shows two other frames of the ST4 crystal scan, during channeling (a) and during reflection (b). The superimposed red lines are the contours of the amorphous position plot (fig. 4.7); they underline the channeling and reflection effect.

In both plots three zones are recognizable. From the bottom to the top of the figure they are:

1. both channeling and reflection are absent; this part of the beam doesn't cross the crystal and corresponds to the bump on the left side of the beam profile (see fig. 4.6(a));

2. both channeling and reflection are present; this part of the beam crosses the crystal;

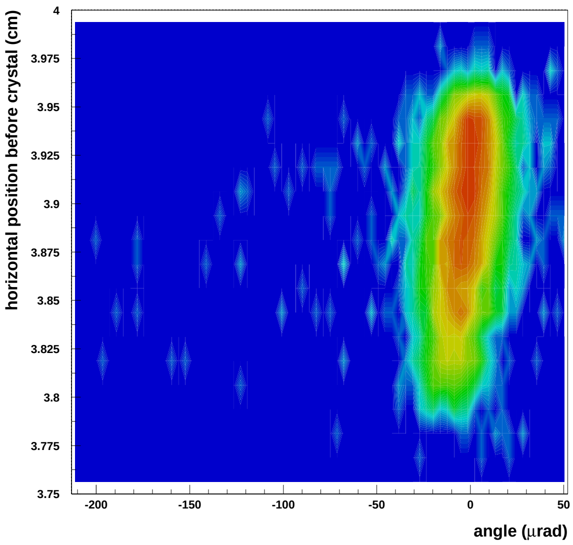

Figure 4.7: Bidimensional plot showing the protons horizontal position, measured by the first module (vertical axis), with respect to their angle. The data are taken from the ST4 crystal scan when it was in the amorphous position, that means both channeling and reflection are absent.

3. both channeling and reflection are absent but there is no evidence of this third beam component in the position beam profile detected in the downstream zone.

The knowledge of the protons position allows to select for the analysis precise regions of the incoming beam. Fig. 4.9(a) presents again the evolution of the beam profile with respect to the crystal rotation angle but in this case the part of the beam that doesn't cross the crystal (marked with 1 in fig. 4.8) is excluded; the difference with the plot of fig. 3.15 is evident in the reflection position where the unperturbed part of the beam disappears. Fig. 4.9(b) shows the result of the gaussian fit of the beam main peak after the cut. Also in this case, according to the sigma trend (bottom of the figure), the beam width seems to decrease when it goes in reflection. This beam compression actually becomes smaller after the cut: the sigma difference goes from about 80 μm for the whole beam (fig. 4.6(b)) to about 50 μm for the one with the cut (fig. 4.9(b)). This means that the analysis performed on the whole beam (the fit of only a part of the beam shown in fig. 4.6) actually causes an apparent beam width decrease but it can't explain completely the effect.

Until now the analysis has been performed using only the beam profile but, as

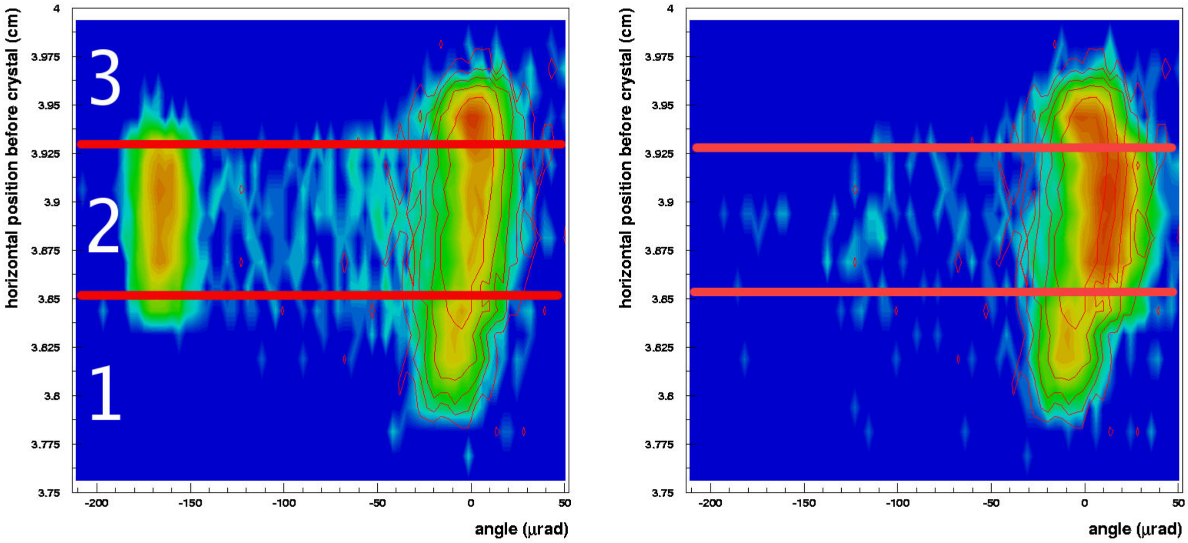

(a) (b)

Figure 4.8: Two interesting frames of the ST4 crystal scan showing the protons horizontal position with respect to their angle. They are taken when: (a) the channeling effect is at its maximum, (b) the reflection effect is complete. Three regions are separated by red lines; the effect of channeling and reflection is present only in the middle one (marked with 2).

shown in sec. 4.1, using the first module information it is possible to compute the angular beam profile with several advantages. The bidimensional plot shown in fig. 4.10(a) is the equivalent of fig. 4.9 (the one with the cut) but it has been obtained with the angular profile instead of the position one. The two plots are similar but performing the main peak analysis (fit of the peak with a gaussian function; the results are presented in fig. 4.10(b)) an interesting difference appears: while in the position profile case the beam sigma in reflection becomes smaller, in the case of the angular profile it increases. So a decrease in beam width corresponds to an increase in its divergence indicating that a focusing effect is present. Fig. 4.11 explains what is happening: the third beam component (marked with 3 in fig. 4.8), which does not suffer channeling and reflection effects, due to its position and propagation angle, is superimposed to the part of the beam in reflection.

The final test to be sure that the beam width decrease is due to the presence of a third beam component is to exclude from the analysis also that component, that means taking into account only the inner part of the beam. Fig. 4.12 shows the bidimensional plot of the ST4 crystal scan obtained with just the beam inner

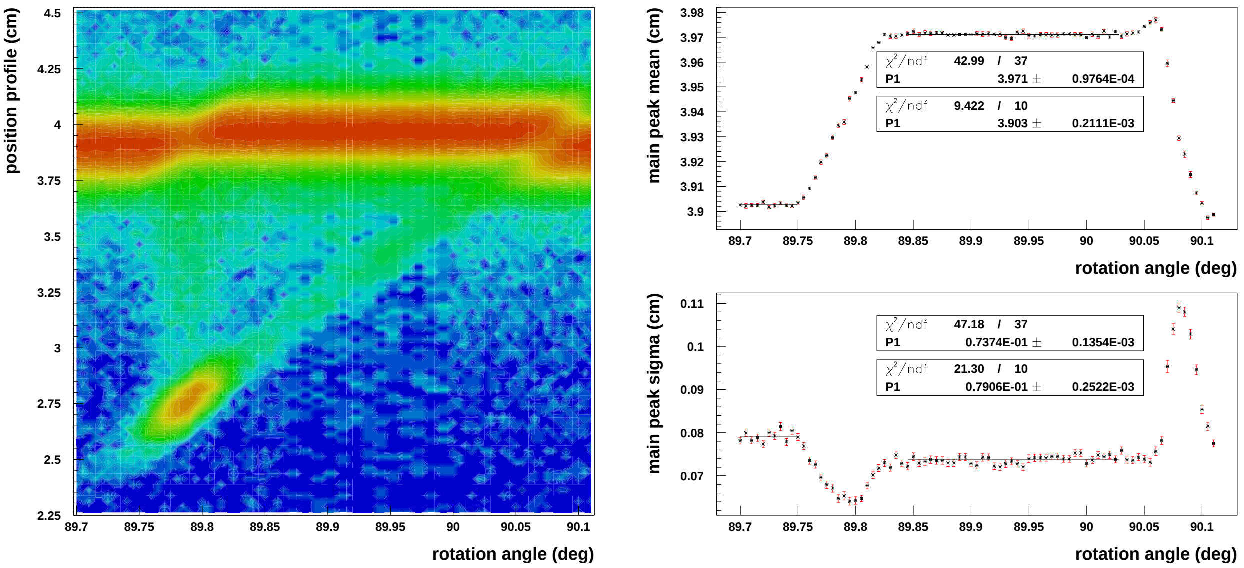

(a) (b)

Figure 4.9: (a) Bidimensional plot of the ST4 crystal scan: on the horizontal axis the crystal rotation angle, on the vertical one the beam profile in the downstream zone, reconstructed using the information from the silicon chambers as described in sec. 4.1. The beam component that doesn't cross the crystal (marked with 1 in fig. 4.8) is excluded. (b) Results of the gaussian fits of the beam profile main peak of the ST4 crystal. Top plot: the gaussian mean trend; the amorphous and reflection positions are fitted with a constant to measure the reflection gap which is 0.0684 ± 0.0002 cm corresponding to 9.83 ± 0.03 μrad. Bottom plot: the gaussian sigma trend; the amorphous and reflection positions are fitted with a constant to measure the sigma variation which is -0.0053 ± 0.0003 cm that is -0.76 ± 0.041 μrad.

part (marked with 2 in fig. 4.8): as expected the sigma decrease in reflection is replaced by a small increase (about 0.51 μrad). Fig. 4.13 shows similar results with the analysis performed with the angular profile.

To give a more quantitative evaluation of the interesting region in the ST4 scan the reflection angle has been computed as a function of the horizontal position detected by the first module; the result is shown in fig. 4.14. The crystal dimension can be roughly estimated as $\sim 875 \pm 50$ μm which is in agreement with the crystal width (900 μm). The plot also shows that the crystal edge is not identified with a very high precision (the first module detector is placed 4 m before the crystal);

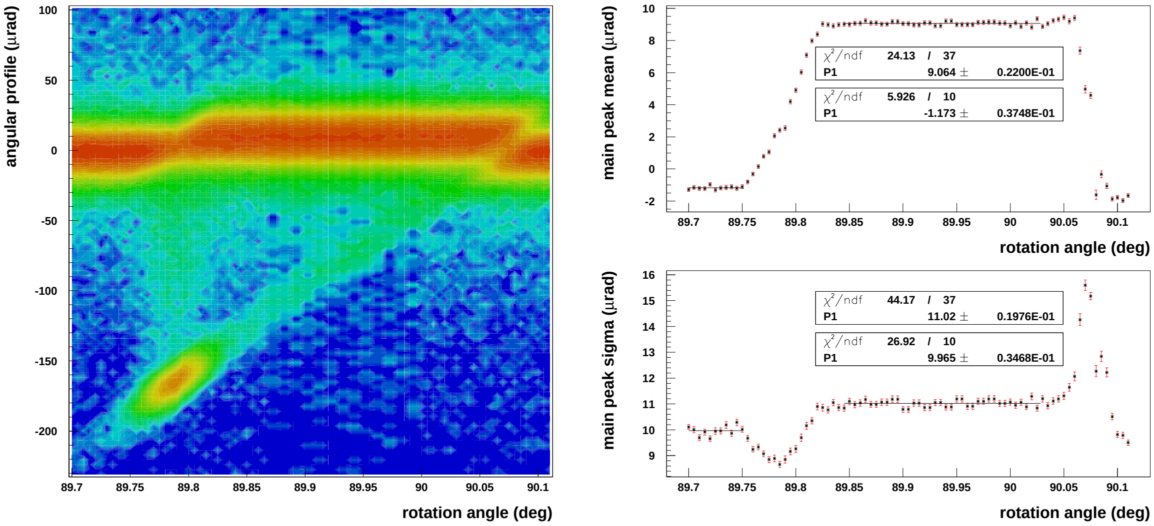

(a) (b)

Figure 4.10: (a) Bidimensional plot of the ST4 crystal scan: on the horizontal axis the crystal rotation angle, on the vertical one the beam angular profile. The beam component that doesn't cross the crystal (marked with 1 in fig. 4.8) is excluded. (b) Results of the gaussian fits of the beam profile main peak of the ST4 crystal. Top plot: the gaussian mean trend; the amorphous and reflection positions are fitted with a constant to measure the reflection gap which is 10.24 ± 0.04 μrad. Bottom plot: the gaussian sigma trend; the amorphous and reflection positions are fitted with a constant to measure the sigma variation which is 1.05 ± 0.04 μrad.

thus the following analysis is performed in a narrower region of 500 μm inside which all the beam should cross the crystal.

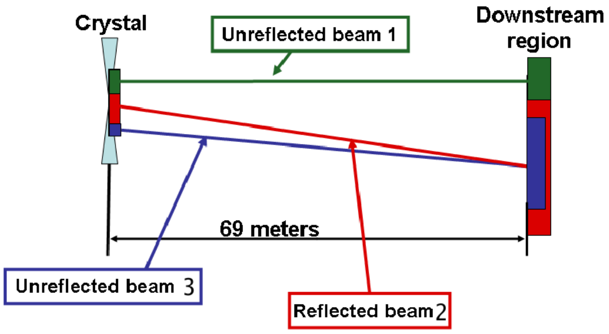

Figure 4.11: Composition of the downstream beam profile when the ST4 crystal is in reflection: only the inner part of the beam is reflected (marked with 2) and so changes its angle, resulting in an effect of separation with respect to the external component of the beam (the one marked with 1); at the same time a focusing effect is present for the other one (marked with 3) causing a beam width decrease during reflection.

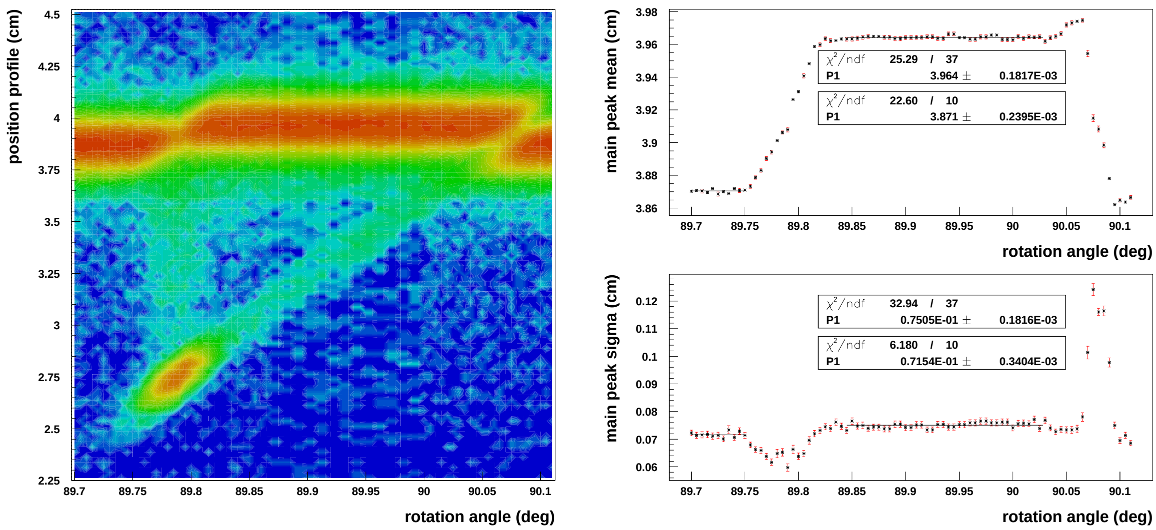

(a) (b)

Figure 4.12: (a) Bidimensional plot of the ST4 crystal scan considering only the inner horizontal part of the beam (beam profile). (b) The results from the gaussian fit of the main peak: in the top plot, the reflection displacement is 0.0937 ± 0.0003 cm that is 13.59 ± 0.04 μrad; in the bottom one, the beam sigma variation in reflection which is 0.0035 ± 0.0004 cm corresponding to 0.51 ± 0.06 μrad.

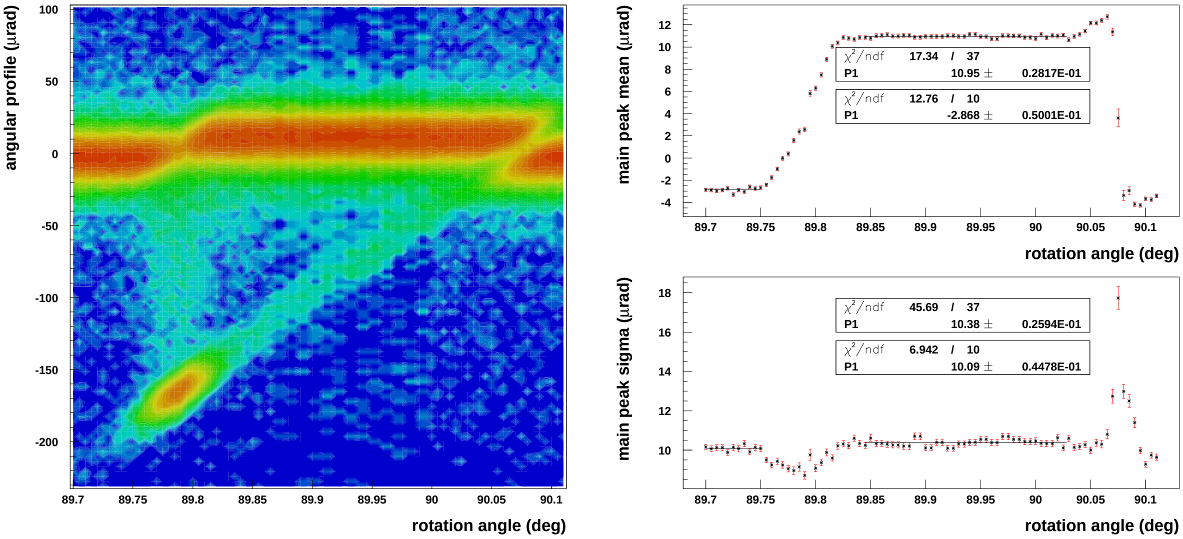

(a) (b)

Figure 4.13: (a) Bidimensional plot of the ST4 crystal scan considering only the inner horizontal part of the beam. On the horizontal axis the crystal rotation angle; on the vertical axis the angular beam profile. (b) The results from the gaussian fit of the main peak: top, the reflection displacement which is 13.82 ± 0.06 μrad; in the bottom one, the beam sigma variation in reflection which is 0.27 ± 0.05 μrad.

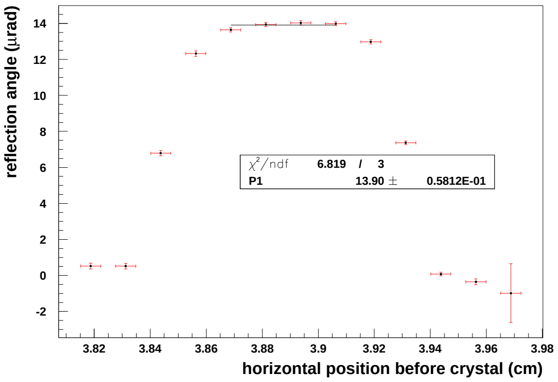

Figure 4.14: Volume reflection angle as a function of the horizontal position before the crystal.

4.2.1 Check on QM2 and double crystals

The plots of fig. 4.8 were crucial for the analysis of the ST4 crystal so it is significant to show them also with data from the other crystals. The first module has been installed only for part of the time so its information is available only for the QM2 crystal and for the data of the double crystals apart from of course the ST4 crystal. Fig. 4.15 shows the QM2 crystal properties of reflection and channeling as a function of the proton horizontal position on the crystal surface, while in fig. 4.16 the same plots are obtained with the data from the double crystals (QM1 and QM2 aligned). In both cases the reflection and the channeling show, differently from the ST4 crystal, a uniform behaviour with respect to the proton horizontal position. This is consistent with the crystal dimension which is bigger than the beam one.

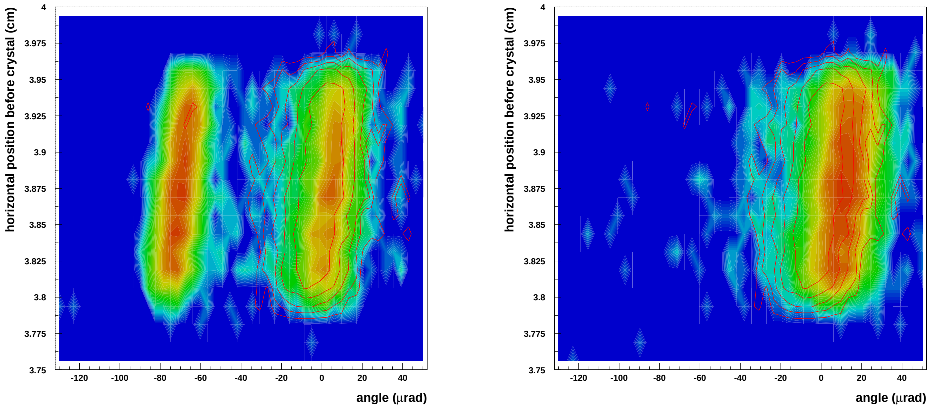

(a) (b)

Figure 4.15: Two frames of the QM2 crystal scan showing the protons horizontal position (vertical axis) with respect to their angle (horizontal axis): (a) the channeling effect is at its maximum; (b) the reflection effect is complete. A uniform behaviour is visible from the comparison with the red superimposed lines which represent the contour of the amorphous position.

4.3 Rotational effect

In the previous section the uniformity of the crystal behaviour in its horizontal dimension has been checked plotting the angle of the protons with respect to their horizontal position on the crystal surface (see for example fig. 4.8). The same kind of plot, using the vertical proton position shows some interesting aspects of non

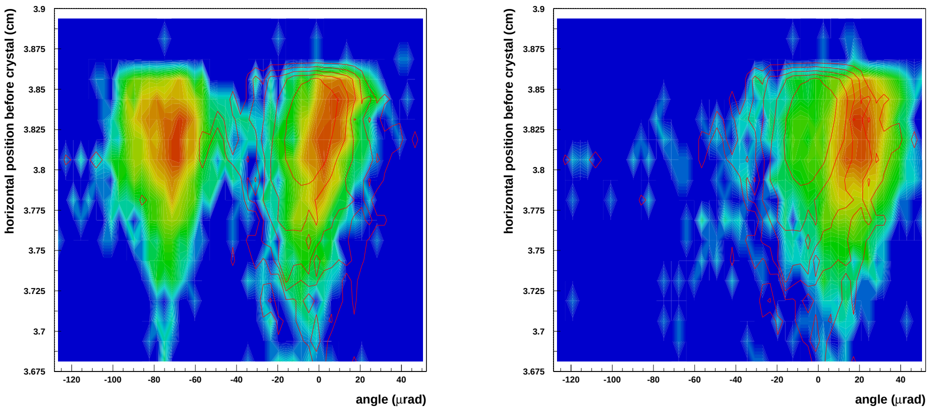

(a) (b)

Figure 4.16: Two frames of the double crystal scan showing the protons horizontal position (vertical axis) with respect to their angle (horizontal axis): (a) the channeling effect is at its maximum; (b) the reflection effect is complete. A uniform behaviour is visible from the comparison with the superimposed red lines which represent the contour of the amorphous position.

uniformity that, as will be demonstrated, have a common explanation: a vertical displacement on the crystal surface has the same effect of a crystal rotation. This effect is common to all the analyzed crystals.

In this section a quantitative evaluation of the effect for the QM2 and the ST4 crystals will be given and it will be shown how this effect could be used “to change” the alignment condition in the double crystal case.

4.3.1 Evaluation of the effect (QM2, ST4 crystals)

Fig. 4.17 presents three frames from the QM2 crystal scan; each plot shows the relation between the protons angle (horizontal axis) and their vertical position on the crystal surface at a different crystal rotation angle; the superimposed red lines are the contour of the same plot taken when the crystal is in the amorphous position and underline the reflection effect. The three plots show:

- a) the beginning of the channeling effect; the channeling peak appears in the lower region of the beam, the reflection effect is almost absent;

- b) the maximum of the channeling effect; the channeling peak is equally spread along the vertical beam direction but it is not parallel to the beam

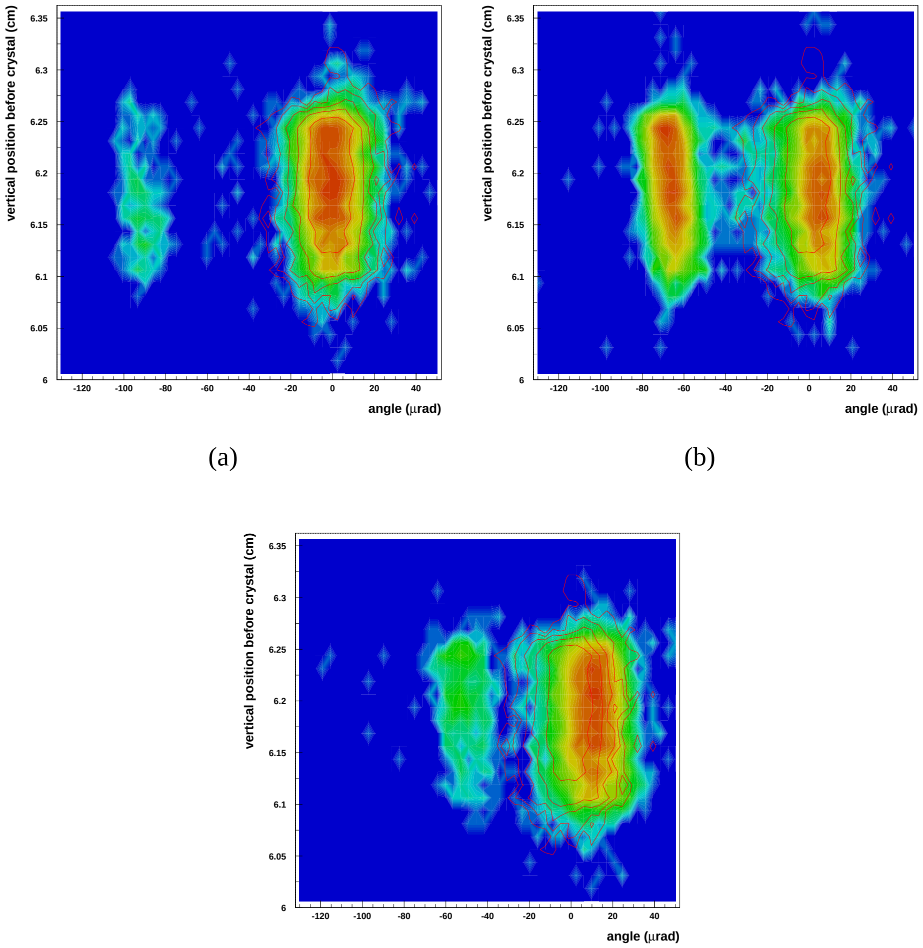

(a) (b)

(c)

Figure 4.17: Three plots of the QM2 crystal scan during the channeling effect showing the beam angular profile (on the horizontal axis) with respect to the vertical beam profile at the crystal (on the vertical axis); the superimposed red lines are the contour of the amorphous position. (a) The channeling peak is appearing, the reflection one is almost absent. (b) The channeling effect is at its maximum. (c) The channeling peak is disappearing, the reflection is almost complete.

main peak indicating that the channeling angle depends on the proton vertical position on the crystal surface;

- c) the end of the channeling effect; the situation is reversed with respect to the beginning of the channeling; the channeling peak disappears in the upper region of the beam and the reflection is almost complete.

If it's assumed that to an increase in the vertical position on the crystal surface corresponds a decrease in its rotation angle, the various situations shown in fig. 4.17 could be explained. In fact according to this assumption:

- the channeling peak appears and disappears before in the lower region of the beam than in the upper one (plots (a), (b) in fig. 4.17);
- the channeling effect has a larger angle in the lower part of the beam, which decreases when the rotation angle increases (plot (b) in fig. 4.17).

The same plot of fig. 4.17(b) is shown in fig. 4.18; the red lines divide the beam in three regions. The aim is to perform a separate analysis with the particles of the upper beam side (marked with 1 in the plot) and of the lower one (marked with 2). Fig. 4.18(b) compares, from a qualitative point of view, the behaviour of the two crystal regions. The bidimensional plot summarizes the QM2 scan with

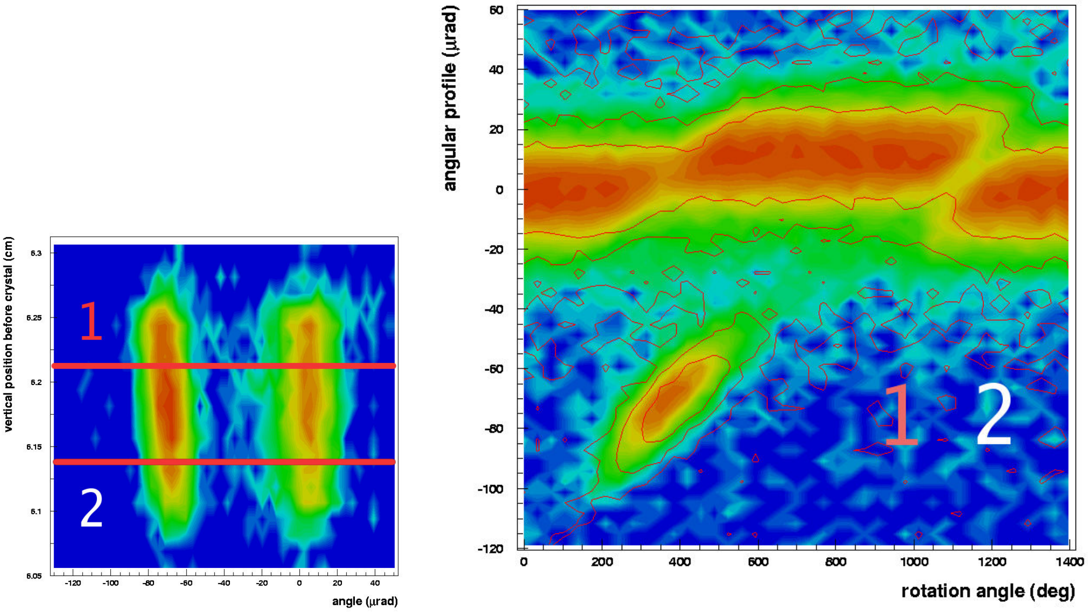

(a) (b)

Figure 4.18: (a) A frame of the QM2 crystal scan during channeling; the red lines limit the two external areas of the beam that will be used in the following analysis (the beam upper region 1 and the lower one 2). (b) Comparison between the bidimensional plots of the QM2 crystal scan obtained with the data from region (1) (red lines) and from region (2) (coloured plot in the background).

the rotation angle on the horizontal axis and the beam divergence on the vertical one: the coloured plot is filled with data from the lower beam region (2) while the superimposed red lines are the contour of the same plot but with data from the upper beam region (1). The contour of the second plot fits well the first one apart from a horizontal shift which, as anticipated, represents the effect of a vertical shift on the crystal surface.

A way to perform a more quantitative analysis consists in taking into account one of the effects of the beam variation due to the crystal, and computing the crystal rotation angle at which it happens. From the comparison of the different angles obtained with the upper and lower part of the beam an estimation of the effect could be given. The chosen reference points are the channeling peak trend and the main peak one during the entrance in reflection. It would be possible to consider also the exit from reflection but, given the presence of a discontinuity, the analysis would be much more complicated. Fig. 4.19 shows the comparison between the behaviour of the channeling peak in case 1 (a) and in case 2 (b). The points are fitted with a straight line then a point that corresponds to the channeling maximum (-70.4 μrad) on the vertical axis is taken and the projection of that point on the horizontal axis is computed. The results are: -36.77 ± 0.88 μrad for case 1 and -40.33 ± 1.82 μrad for case 2 that means a horizontal shift of 3.56 ± 2.02 μrad.

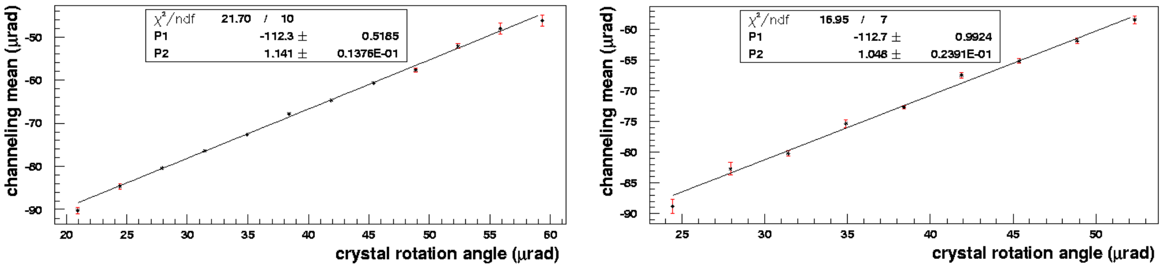

(a) (b)

Figure 4.19: The points in the plots represent the channeling peak angular position as a function of the rotation angle of the crystal; they are the mean value of the gaussian that fits the channeling peak; the error bars are the error values given by the fit. (a) Data from the upper beam region (marked with 1 in fig. 4.18); the horizontal value which corresponds to the projection of the vertical coordinate -70.4 μrad is -36.77 ± 0.88 μrad. (b) Data from the lower beam region (marked with 2 in fig. 4.18); the horizontal value which corresponds to the projection of the vertical coordinate -70.4 μrad is -40.33 ± 1.82 μrad.

The second reference point taken into account is the main peak entrance in reflection. This second measurement combined with the previous one will give a more precise result. Fig. 4.20 shows the comparison between the main peak trend in case 1 (a) and in case 2 (b). The diagonal points that represent the movement of the main peak to the reflection position are fitted with two straight lines (the entrance in reflection happens in two steps). The projections on the horizontal axis of an intermediate point of the two segments are found in both cases. The rotational shift values computed for the two segments are: 2.93 ± 4.62 μrad for the first segment and 3.79 ± 4.97 μrad for the second one; the average is 3.36 ± 3.39 μrad. The agreement of the values obtained with the channeling peak trend and the main peak one proves that the effect of non homogeneity shown in fig. 4.17(a) (c) and the effect of channeling "diagonality" of fig. 4.17(b) are two aspects of the same phenomenon that is the rotation effect, whose final value, computed as the average of the two, is 3.46 ± 1.98 μrad.

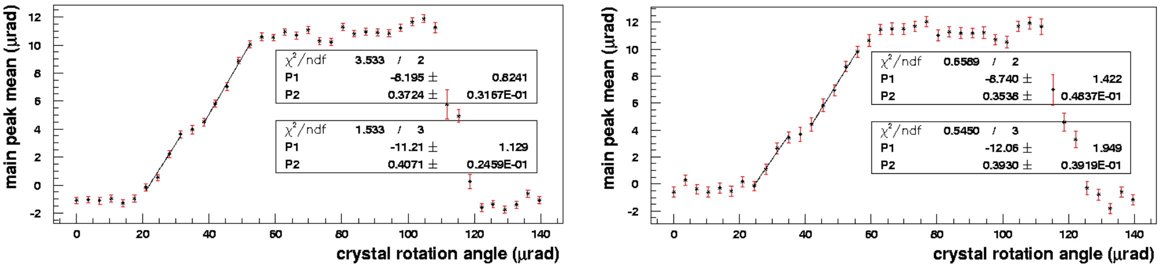

(a) (b)

Figure 4.20: The points in the plots represent the main peak angular position as a function of the crystal rotation angle; they are the mean values of the gaussian that fits the main peak; the error bars are the error values given by the fits. The diagonal points of the main peak shift from the amorphous to the reflection position are fitted with two straight lines; then the projections on the horizontal axis of an intermediate point of the two segments are computed. (a) Data from the upper beam region (marked with 1 in fig. 4.18): the first rotation angle is -26.46 ± 2.23 μrad corresponding to the vertical value 1.66 μrad (bottom segment); the second rotation angle is -45.60 ± 2.78 μrad corresponding to a vertical value of 7.35 μrad (top segment). (b) Data from the lower beam region (marked with 2 in fig. 4.18): the first rotation angle is -29.39 ±4.05 μrad corresponding to a vertical value of 1.66 μrad (bottom segment); the second rotation angle is -49.39 ± 4.97 μrad corresponding to a vertical value of 7.35 μrad (top segment).

As anticipated, the rotation effect is common in all the cases that can be analyzed by means of the first module information. Fig. 4.21 shows two interesting frames of the ST4 crystal scan; the plots are the beam angular profile with respect to the protons vertical position at the crystal. The first frame (4.21(a)) shows the comparison between the beginning (superimposed red lines) and the end of the channeling effect (plot in the background); the channeling peak appears and disappears in the upper region of the beam. This means that the ST4 crystal has the opposite behaviour with respect to the QM2 crystal and, in fact, also the diagonal described by the channeling peak has the opposite direction (see fig. 4.17 for comparison). The second frame (4.21(b)) shows two steps of the beam exit from the reflection position: the amorphous peak appears in the upper part of the beam (first step represented by the red lines) while the reflection peak disappears in its lower part.

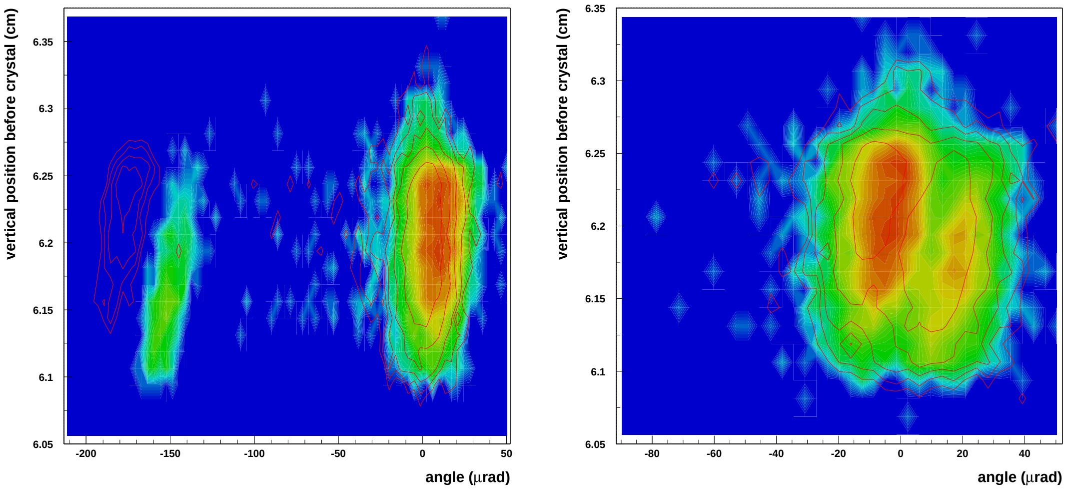

(a) (b)

Figure 4.21: Two interesting frames of the ST4 crystal scan; they show the protons vertical position at the crystal with respect to their angle. They are taken when: (a) the channeling effect is at its maximum, (b) the reflection effect is complete.

The same analysis method used to estimate the rotation effect for the QM2 crystal can be used also for the ST4 crystal. Fig. 4.22(a) shows the two beam slices which will be used for the following differential analysis. Unlike the QM2 crystal case, the regions chosen are smaller and more distant one from the other, in order to maximize the effect and simplify the computation of their physical distance. The rotation effect is linear with the vertical displacement on the crystal, as can be understood from the fact that the channeling peak forms a diagonal (a straight line) with respect to the main one (see it in fig. 4.22(a)). Thus it can be interesting to measure not only the absolute value of the rotational displacement, but also the ratio between it and the vertical displacement. The two slices width is 500 μm and they are centered on the two values: 6.265 cm (slice 1), 6.115 cm (slice 2) so their distance is roughly 1500 ± 100 μm. In fig. 4.22(b) the data of the two slices form the bidimensional plot of the beam angular profile as a function of the crystal rotation angle. The red lines contour plot (data from slice 1) is visibly shifted with respect to the coloured one (data from slice 2) in the background.

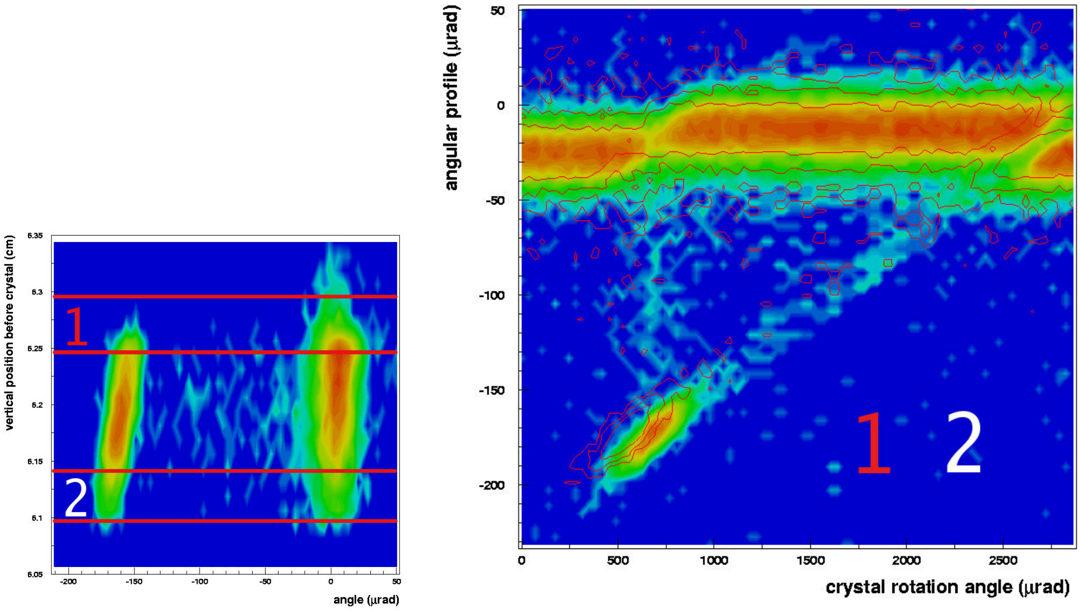

(a) (b)

Figure 4.22: (a) A frame of the ST4 crystal scan during channeling; the red lines limit the two beam slices that will be used in the following analysis (the beam upper region 1 and the lower one 2). (b) Comparison between the bidimensional plots of the ST4 crystal scan obtained with the data from the upper region of the beam (1) (red lines) and from the lower one (2) (coloured plot the in background).

The effect of the angular shift between the two slices is computed as it was done for the QM2 crystal:

- in fig. 4.23 the comparison between the trends of the channeling peaks is shown. Projecting the same vertical value (the channeling maximum, -170.1 μrad) on the horizontal axis the two obtained values are shifted of 14.68 ± 4.41 μrad;
- fig. 4.24 shows the comparison between the trends of the main peak in the two cases; the movement from the amorphous position to the channeling one is fitted with a straight line; the projection of an intermediate point

between the two positions is computed. The values obtained in the two cases differ of 14.06 ± 2.93 μrad;

- as the value obtained with the channeling peak comparison is consistent with the one obtained with the main peak comparison, it is meaningful to compute their average which is 14.37 ± 2.65 μrad.

Thus a crystal rotation of 14.37 ± 2.65 μrad is equivalent to a vertical displacement of 1500 ± 100 μm on the ST4 crystal surface which means $9.58 \pm 1.89\ \frac{\mu\text{rad}}{\text{mm}}$.

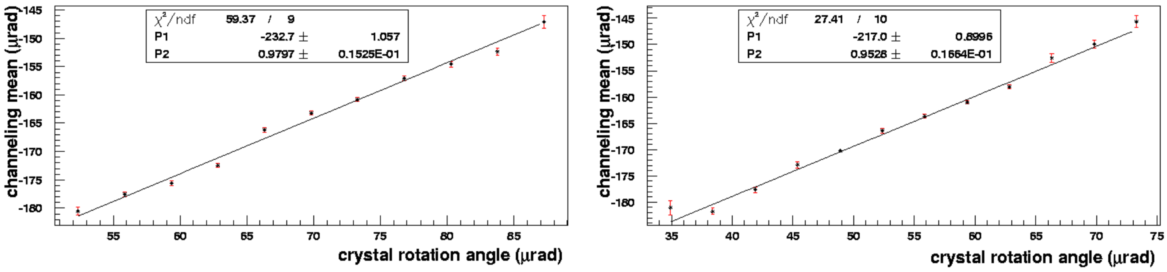

(a) (b)

Figure 4.23: The points in the plots represent the channeling peak angular position as a function of the rotation angle of the crystal; they are the mean value of the gaussian that fits the channeling peak; the error bars are the error values given by the fit. (a) Data from the upper beam region (marked with 1 in fig. 4.22); the horizontal value which corresponds to the projection of the vertical coordinate -171.1 μrad is -62.87 ± 2.94 μrad. (b) Data from the lower beam region (marked with 2 in fig. 4.22); the horizontal value which corresponds to the projection of the vertical coordinate -171.1 μrad is -48.19 ± 3.29 μrad.

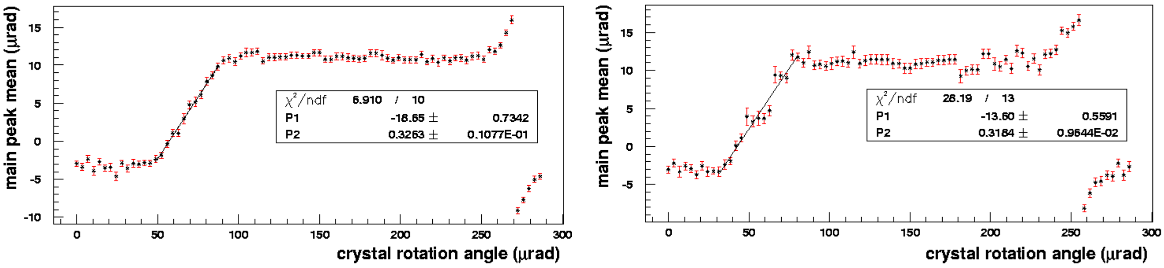

(a) (b)

Figure 4.24: The points in the plots represent the main peak angular position as a function of the crystal rotation angle; they are the mean values of the gaussian that fits the main peak; the error bars are the error values given by the fits. The diagonal points of the main peak shift from the amorphous to the reflection position are fitted with a straight line, then the projection on the horizontal axis of an intermediate point of the line is computed. (a) Data from the upper beam region (marked with 1 in fig. 4.22): the rotation angle -72.79 ± 2.30 μrad corresponds to the vertical value 5.1 μrad. (b) Data from the lower beam region (marked with 2 in fig. 4.22): the rotation angle -58.73 ± 1.81 μrad corresponds to the vertical value 5.1 μrad.

4.3.2 Double crystal scan

In the double crystal analysis even if the crystals are properly aligned their effect on the beam is more complex with respect to the effect of the single crystal. This is evident observing the bidimensional plot of the beam divergence as a function of the crystals rotation angle, presented in fig. 4.25:

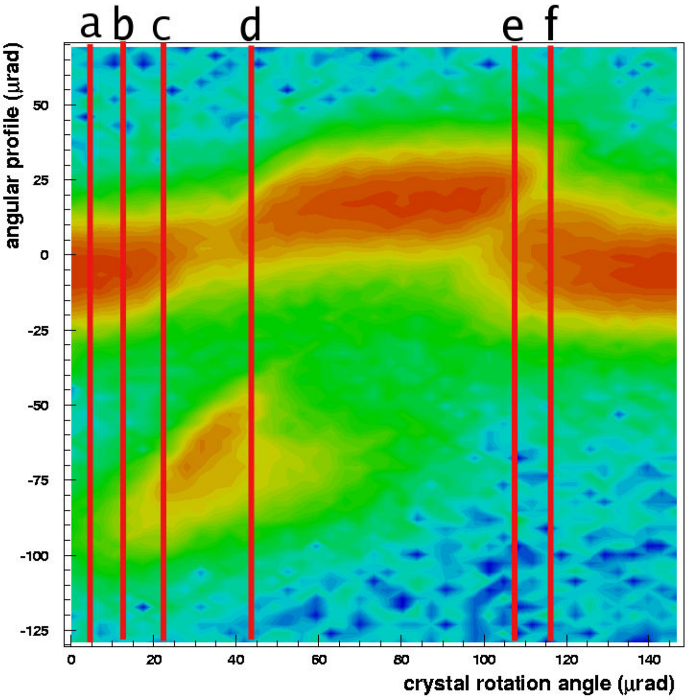

Figure 4.25: Bidimensional plot of the double crystal scan: on the horizontal axis the crystal rotation angle, on the vertical axis the beam angular profile, reconstructed using the information from the silicon chambers and the first module, as described in sec. 4.1.

- the reflection effect could be seen as the sum of the two single crystal effects; since the two crystals are different they can't be perfectly aligned, so the entrance into and the exit from the reflection position happen in different steps depending on which crystal is in the reflection position. In addition, when the first crystal crossed by the beam is in reflection, it bends the protons that impinge on the second crystal interfering with its normal behaviour;

- the channeling effect happens independently for the two crystals but they interfere with each other in two ways: the channeling peaks are overlapped in space and if the crystals are in the channeling position at the same time, the first crystal crossed by the beam subtracts straight particles to the second one due to its channeling peak, so that the second channeling peak appears less intense.

To understand the contribution of each single crystal in the behaviour of the double crystal scan, an analysis has been performed based on the rotation effect described in sec. 4.3.1.
Fig. 4.26-4.28 show six plots of the proton vertical position with respect to the beam divergence; they are taken from the double crystal scan. The angles at which each frame corresponds are shown by a vertical red line in fig. 4.25; the plots are ordered according to the position (from left to right) of the corresponding line.
It will be shown how each plot allows to understand which crystal is working in that specific goniometer position, but before analyzing the single positions in detail, a comment has to be made on the one of fig. 4.27(a) which shows a frame in which both the channeling peaks are present with a similar intensity. The remarkable thing is their orientation with respect to the vertical direction as they form an opposite angle. As shown in sec. 4.3.1 this means that for one crystal (the one that will be called A, for simplicity) the upper part of the beam anticipates the behaviour of the lower one, while for the other crystal (it will be called B) the rotation effect is opposite, that is the lower part of the beam will anticipate the upper one. According to this statement the beam behaviour in the different plots can be understood:

- *fig. 4.26(a)*, the A channeling peak is appearing in the upper region of the beam; this means the channeling effect of the A crystal is beginning;

- *fig. 4.26(b)*, the channeling peak of the B crystal appears in the lower part of the beam; the channeling effect of the B crystal is starting;

- *fig. 4.27(a)*, the upper region of the beam is going into the reflection position; at this rotation angle the reflection contribution of the A crystal starts. The channeling peak of the B crystal is much more intense than the A crystal one, suggesting that the beam first crosses the B crystal and then the A one;

- *fig. 4.27(b)*, the two channeling peaks and so their angles with respect to the beam main peak are clearly visible. For what concerns the main peak, the situation is complicated by the interference between the two crystals. Fig. 4.27(a) states that the A crystal starts reflection before the B one; this last one, however, is crossed by the beam first, so when it starts reflection, it bends the A crystal incoming beam, disturbing its normal reflection trend. Assuming this hypothesis is correct, there are two possibilities: either the bending angle is in phase with the goniometer one, that means it accelerates the A crystal entrance in reflection, or it has an opposite phase in which case the B crystal bending effect extends the A crystal entrance in reflection. The entrance in reflection runs in parallel with the channeling effect so the reflection interference should compress or enlarge the A crystal channeling peak in the plot of fig. 4.25. Observing the plot, the two channeling peaks are visible; they are underlined in fig. 4.29 with different colours; the less intense one is the A crystal one as stated watching fig. 4.27(b) and it is the one marked in blue. The channeling peak usually forms an angle of about 45° in the beam divergence crystal rotation angle plane, but in fig. 4.29 it is evident that the A crystal channeling peak forms an angle greater than 45° with respect to the vertical axis and that means it is subject to a horizontal dilatation which is due to the reflection interference of the B crystal that bends the beam in the opposite direction with respect to the goniometer movement. Once this effect of reflection interference is understood, the main peak trend shown in fig. 4.27-4.28 can be explained. Its peculiarity is that it has the same shape of fig. 4.27(a) but it is shifted to the right (to the reflection position). This happens because, unlike in fig. 4.27(a), in fig. 4.27(b) the B crystal reflection contribution is adding and at the same time the A crystal contribution doesn't evolve due to the reflection interference caused by the B crystal;

- *fig. 4.28(a),* the lower part of the beam goes back to the amorphous position, that means the B crystal starts its exit from the reflection position;
- *fig. 4.28(b),* the lower part of the beam is in an intermediate position between the amorphous and the reflection one while its upper part has just gone back in the amorphous position. That means the B crystal has concluded its exit from reflection while the A crystal is starting its one.

The information obtained from the double reflection scan is summarized in fig. 4.29(a). Black and blue lines are superimposed to the bidimensional plot of the proton angle as a function of the goniometer angle; they point out the single crystal contribution. The lines relative to the A crystal are blue while the B ones are black:

- the A crystal starts the entrance in the reflection position before the B one but B completes its entrance in reflection before A;
- the B crystal starts and ends its exit from reflection before A;

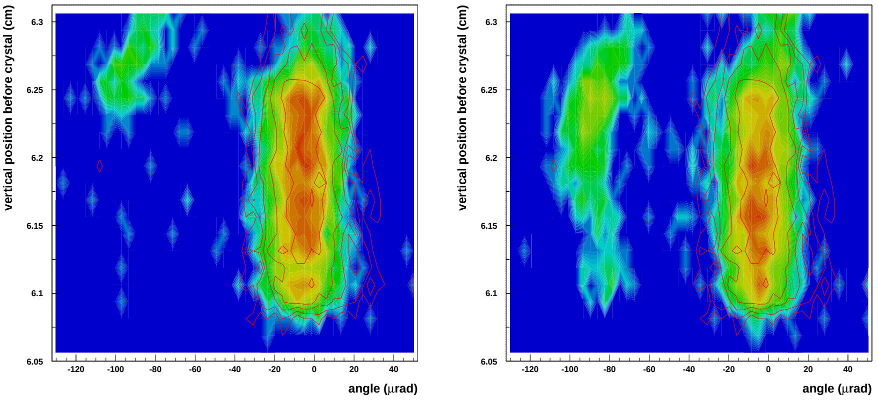

(a) (b)

Figure 4.26: Two plots of the double crystal scan that show the proton vertical position with respect to their angle: (a) the A crystal channeling peak is appearing in the upper part of the beam; (b) the B crystal channeling peak is appearing in the lower part of the beam.

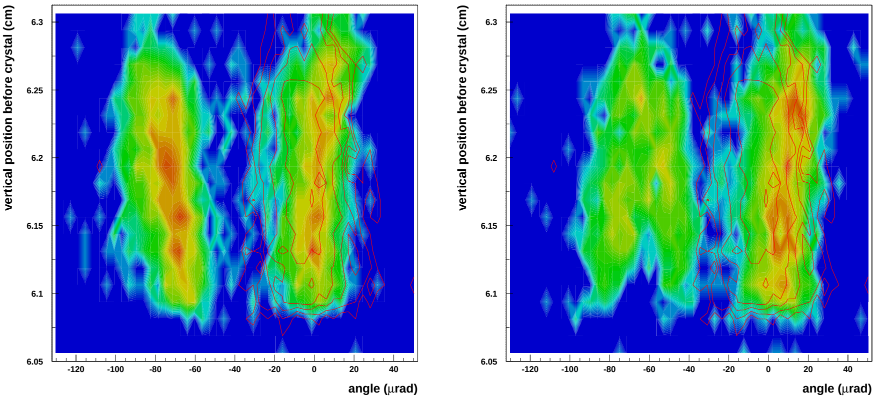

(a) (b)

Figure 4.27: Two plots of the double crystal scan that show the proton vertical position with respect to their angle: (a) the A crystal is going into reflection; (b) the two channeling peaks and their orientation with respect to the beam main peak.

- the channeling peak of the B crystal is much more evident than the A one which is recognizable as it appears before and disappears after the B one.

The beam crosses first the B crystal, so this crystal is not influenced by the other one and it is likely that some of its characteristics can been seen in the beam

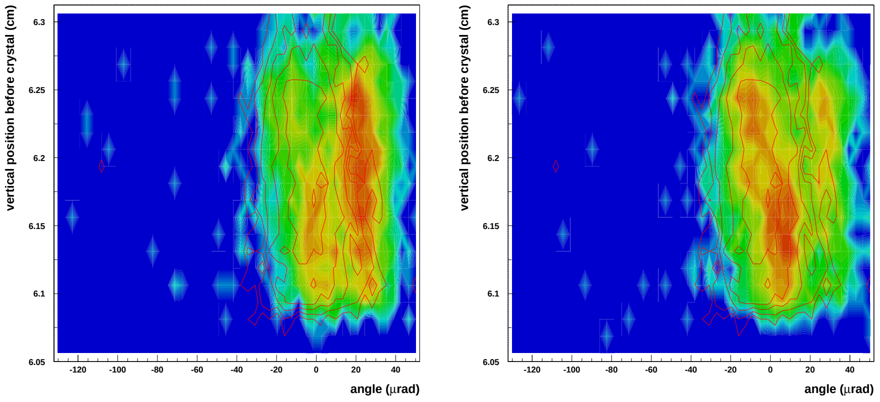

(a) (b)

Figure 4.28: Two plots of the double crystal scan that show the proton vertical position with respect to their angle: (a) the B crystal is going back to the amorphous position; (b) the B crystal has completed its exit from reflection while the A crystal is starting it.

profile. For this reason it is meaningful to try to compare the bidimensional plot of the double reflection scan with the one of the single crystal. In fig. 4.29(b) the comparison of the double crystal scan with the one of the QM2 crystal is shown: the QM2 channeling peak seems to fit well the channeling peak of the B crystal and so do its entrance and exit from reflection. Thus it is possible to affirm that the B crystal is QM2.

The previous section showed that if the beam is divided in vertical slices the effects of the crystal on these slices are shifted with respect to the rotation angle. This angular shift can't be obtained in the double crystal case because (see fig. 4.27(a)) the rotation effect has the opposite direction for the two crystals. According to this, a division of the beam in vertical slices should show different alignment conditions in the beam slices.
Fig. 4.30(a) shows the beam vertical profile as a function of its divergence (during the double crystal scan at the channeling position); the region above the red line is the one used for the plot of fig. 4.30(b) in which the beam divergence is plotted as a function of the goniometer angle. The rotation effect implies that in the upper part of the beam the A crystal anticipates its effect while the B crystal delays its own. Therefore comparing fig. 4.30(b) with fig. 4.29(b) the contribution of the A crystal is shifted to the left while the B crystal effect is shifted to the right. In this configuration the crystals alignment is more accurate: the two channeling peaks are almost overlapped; the passage from the reflection to the amorphous posi-

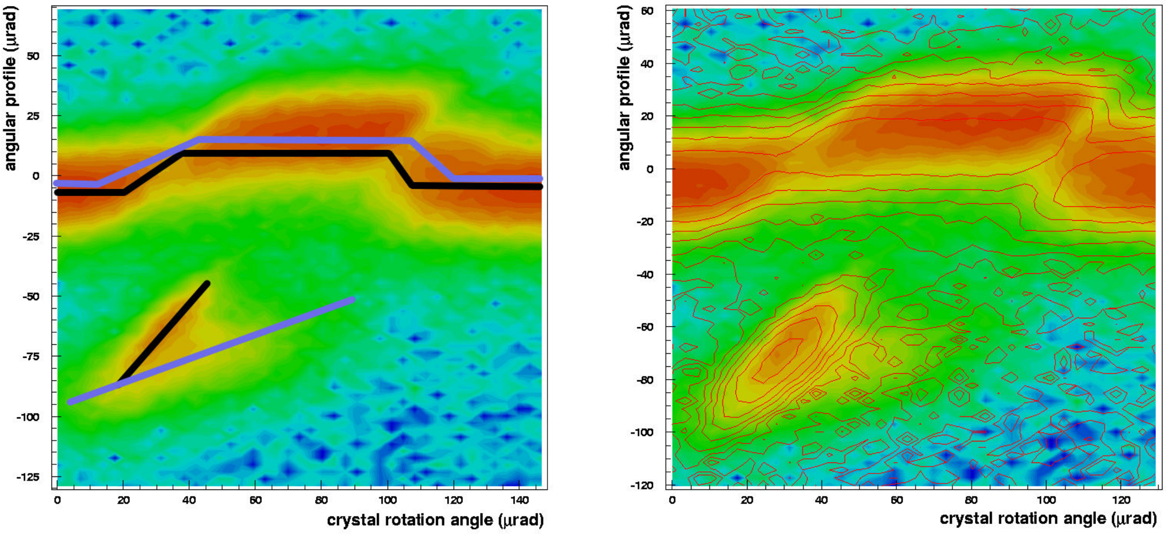

(a) (b)

Figure 4.29: (a) Bidimensional plot of the double crystal scan (rotation angle on the horizontal axis, beam divergence on the vertical one); the superimposed lines represent the contribution of the two crystals, in blue the A crystal, in black the B one. (b) The same plot with the contour of the QM2 crystal superimposed; the comparison between the channeling peak shapes suggests that the B crystal is QM2.

tion is the same for the two crystals while the entrance in channeling seems more gradual but this is caused by the reflection interference between the two crystals.

If the beam region taken into account is the lower one, the direction of the crystals shift will be inverted with respect to the upper one.
Fig. 4.30(b) shows a better crystal alignment (compared with the global plot). According to this, the data from the lower region of the beam should show a worse crystal alignment; in fact in fig. 4.31, presenting the beam divergence plotted as a function of the goniometer angle, the two channeling peaks are separate and both the entrance into and the exit from the reflection position show the presence of the different contributions from the two crystals.

The main and channeling peak trends extracted from the data of the upper and lower part of the beam are compared in fig. 4.32 (main peak) and in fig. 4.33 (channeling peak); they are obtained by means of a gaussian fit of the peak, so that the peak position corresponds to the gaussian mean while the error bars are the error of the fits.

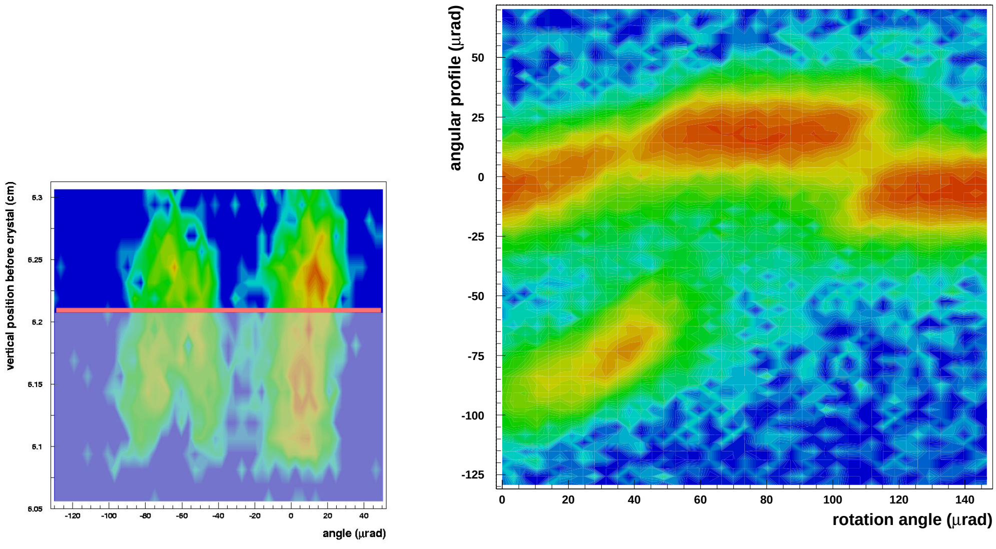

(a) (b)

Figure 4.30: (a) A frame of the double crystal scan during channeling; the red lines limit the external area of the beam, whose data are used to produce the (b) plot. (b) Beam divergence with respect to the goniometer rotation angle. The plot should be compared with the one shown in fig. 4.29(b); here a better crystal alignment is visible.

Fig. 4.32(a) shows the main peak trend of the upper part of the beam, which is the beam region in which the best alignment is present; this is confirmed by the superposition of the two crystals entrance to and exit from the reflection position. This behaviour is not visible in fig. 4.32(b) which shows the main peak trend of the lower beam region, the more disaligned one. On one hand, a longer entrance in the reflection position with respect to the (a) figure is visible, which indicates less superposition between the two crystals; on the other hand the exit from the reflection position is divided in two distinct steps. As stated, in the lower beam region the contribution of the A crystal is shifted to the right while the B crystal effect is shifted to the left. Therefore the first step from the reflection position to the amorphous one corresponds to the B crystal (QM2) while the second step is due to the A crystal; it is remarkable that differently from the (a) figure the two processes are separate so no interference is present. Comparing the two exits from reflection, in the first case it happens in about 5 goniometer steps (each step is about 3.5 μrad) while in the second one it needs two phases, the first (B crystal) is of 5 goniometer steps, the second (A crystal) in about 8 steps which means that

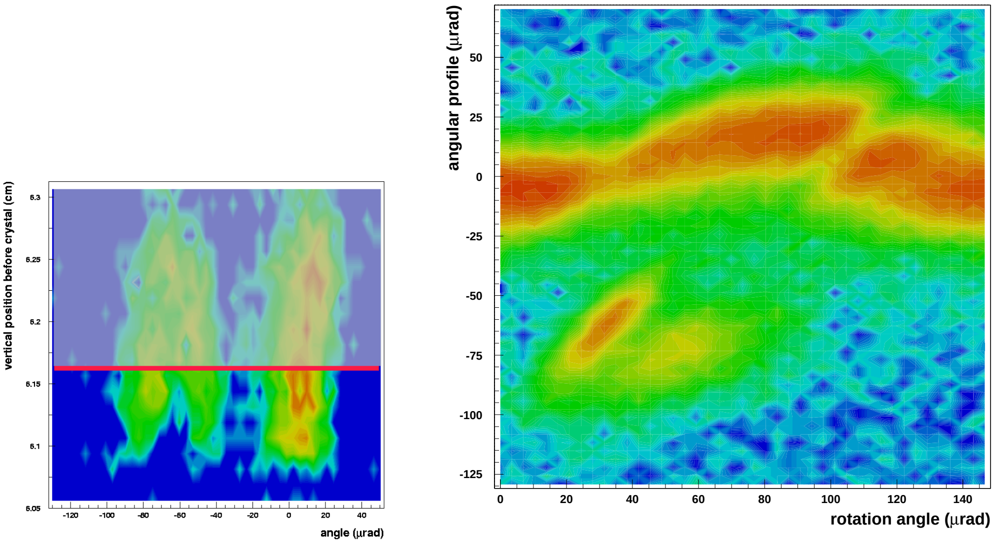

(a) (b)

Figure 4.31: (a) A frame of the double crystal scan during channeling, the red lines limit the external area of the beam, whose data are used to produce the (b) plot. (b) Beam divergence with respect to the goniometer rotation angle. The plot should be compared with the one shown in fig. 4.29(b); here a worse crystal alignment is visible.

also assuming that in the (a) plot the crystals start the exit from reflection at the same time about 3 (10.5 μrad) goniometer steps of the A crystal exit are missing with respect to the (b) figure. In the (a) figure the two exits from the reflection are interfering with each other. As this interference delays the entrance in reflection, it compresses the exit. During its exit from reflection, the B crystal bends the beam impinging on the A crystal in the same goniometer direction, so the A crystal undergoes the standard goniometer rotation plus the B crystal reflection angle (about 12 μrad) that explains the apparent disappearance of a part of the A crystal exit from reflection. The comparison between the channeling peak trends in the “aligned” and “disaligned” case gives a clear indication of the direction in which the two crystals contribution has been shifted. In fig. 4.33(a) the two channeling peaks merging, figured out in fig. 4.30(b), is confirmed. Their fits, in fact, follow a continuous line; however three different regions are detectable:

- *first 3 points*, only the A crystal channeling peak is present;
- *following 4 points*, the A crystal channeling peak is still the object of the fit

but the slope is decreased due to the interference with the B crystal entrance in reflection;

- *last 7 points,* only the B crystal channeling peak is present.

So the A crystal channeling peak anticipates the B crystal one while fig. 4.33(b) describes the opposite situation where the B crystal channeling peak precedes the A crystal one which is recognizable because of its lower slope caused by the interference with the B crystal entrance in reflection.

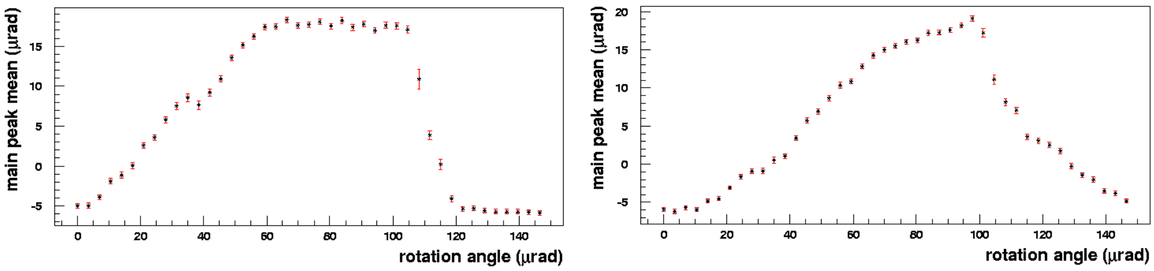

(a) (b)

Figure 4.32: The main peak trend; the points are the means of the gaussian that fits the peak and the error bars are the errors from the fit; the two plots concern the double crystal scan with data from: (a) the upper part of the beam (see fig. 4.30), (b) the lower part of the beam (see fig. 4.31).

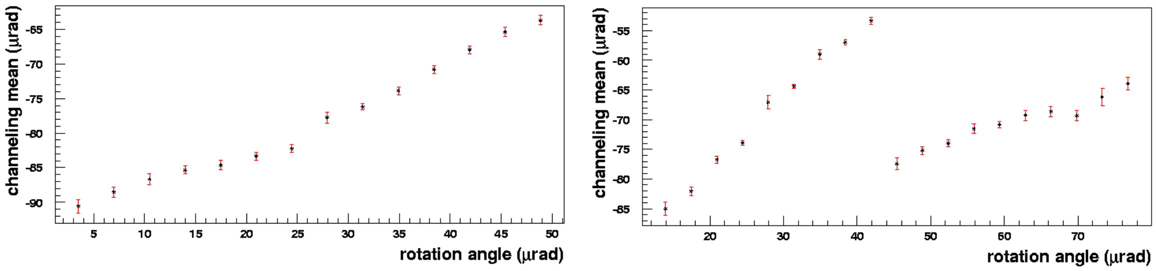

(a) (b)

Figure 4.33: The channeling peak trend; the points are the means of the gaussian that fits the peak and the error bars are the errors from the fit; the two plots concern the double crystal scan with data from: (a) the upper part of the beam (see fig. 4.30), (b) the lower part of the beam (see fig. 4.31).

4.4 Efficiency measurements

The crystal efficiency will be given as a function of the effect the crystal has on the proton beam, that is an efficiency for channeling, for reflection, dechanneling and volume capture. This efficiency is a function of the angle between the impinging proton and the crystal itself.

Thus, the efficiency should be measured in a way that given this angle, it would be possible to assign to the proton a probability for each single effect. To compute this “ideal” efficiency, it is necessary to:

- once chosen the reference frame, measure: (1) the proton angle before the crystal; (2) the crystal rotation angle; (3) the proton outcoming angle after the crystal. These three numbers will allow the calculation of the proton impact angle on the crystal and the proton bending because of the crystal;
- assign to each impact angle a bending angle range for each crystal effect;
- the efficiency of an effect is the ratio between the number of particles undergoing this effect and the total number of particles impinging on the crystal.

Such an ideal efficiency cannot be computed with this experiment:

- an intrinsic limitation is given by the presence of the crystal itself, that transforms the theoretical bending angle in an angular range so that the effects are not sharply separated;
- the experimental setup for these data does not allow the computation of the incoming angle; the basic hypothesis is that the beam we have measured with the first module arrives undeflected on the crystal; in other words, the divergence of the beam between the module and the crystal is neglected;
- the angular resolution of the detectors system is finite and in particular the multiple scattering effects of the materials on the beam path result in a larger range for the bending angles.

These preliminary considerations suggest the changes in the detectors system to improve its performance: the particles incoming angle should be measured and the contribution to the multiple scattering should be minimized. Chap. 5 shows how these requests have been satisfied by the detectors apparatus implemented for the May 2007 testbeam.

Anyway, these limitations can be overcome considering another way to measure the efficiency just comparing the number of protons in the amorphous peak with the number in the different channels. In this way, what happens upstream is not taken into consideration.

4.4.1 Method definition (ST4 crystal)

In this section, using the ST4 crystal as an example, it will be explained how the various effects are characterized and how their efficiency could be estimated by a comparison with the beam in the amorphous position.

The analysis is performed with the following spatial cuts applied on the first module coordinate:

- in the horizontal direction the 500 μm slice which is contained in the crystal shape (individuated in fig. 4.14) has been considered;
- in the vertical direction the beam tails have been excluded, to reduce the background (a slice of ~ 3 mm is taken into account).

4.4.1.1 Reflection efficiency

As anticipated, before computing the various efficiency values it is necessary to study the crystal characteristics in order to assign to each rotation angle a bending angle range for each crystal effect. This is done fitting the beam main peak and the channeling one with gaussian functions.

Fig. 4.13(b) shows the main peak divergence trend for the ST4 crystal scan; the reflection angle and the peak width enlargement in reflection are computed with respect to the amorphous position as the proton angle before the crystal is unknown. Essentially for the same reason the reflection efficiency is computed in comparison with the amorphous peak with the following procedure:

- for each frame of the crystal scan the total number of events has been computed and rescaled to 100; this procedure which is fundamental for all the efficiency measurements, has also been applied to normalize all the presented bidimensional scan plots;
- for each goniometer step, using the values from the gaussian fit of the main peak, the events within 3σ from the mean of the peak are counted and the percentages computed in this way are shown in fig. 4.34 as a function of the goniometer angle;
- the average number of the events under the main peak in the reflection position, $N_{R(3\sigma)}$, and in the amorphous one, $N_{A(3\sigma)}$, is computed by means of a constant fit; the reflection efficiency is defined as the ratio between the two numbers:

$$\varepsilon_R = \frac{N_{R(3\sigma)}}{N_{A(3\sigma)}} \tag{4.1}$$

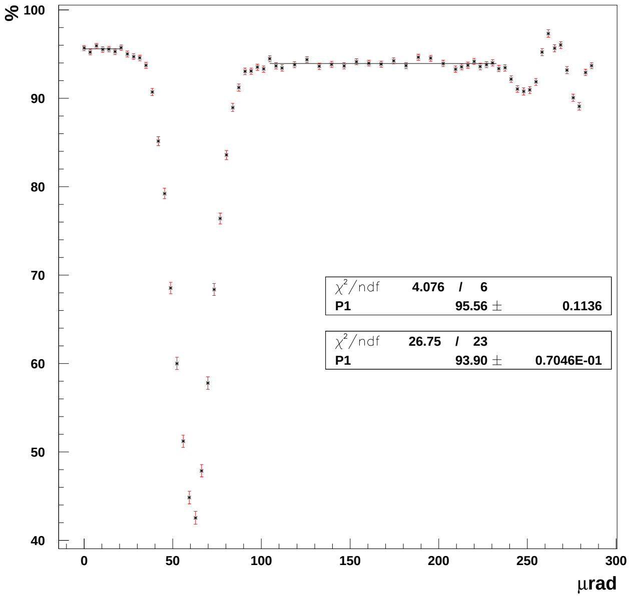

Figure 4.34: The plot shows the number of events within 3σ from the main peak as a function of the goniometer angle; the mean and sigma values are the ones from the fits shown in fig. 4.13(b) for each goniometer step; the errors are computed according to the binomial statistics. Both the amorphous and the reflection plateau are fitted with a constant to obtain their average values

The reflection efficiency of the ST4 crystal is $98.26 \pm 0.14\%$. Two questions are still to be discussed:

- the efficiency definition doesn't allow to check the angular shift and the sigma stability of the beam during reflection; for example, if the reflection angle varies (during the reflection position), the fit parameters (used to compute the efficiency) will follow the peak movement, thus the variation of the reflection angle will not influence the reflection efficiency measurements;
- the method assumes the gaussian shape of the divergence beam profile during the reflection position, but eventual deviations from this shape could mean non-detectable inefficiency effects.

The reflection stability can be independently checked observing the main peak trend and the ST4 crystal, for example, doesn't show any stability problem (fig. 4.13(b)) as the position of the reflected peak is constant within the experimental error. Anyway, the efficiency definition can be slightly changed in order to be self consistent with the reflection angle definition, which is unique and corresponds to the average position of the beam in reflection.

The plots in fig. 4.13 show that one value for the main peak angle and its sigma for the amorphous position and one value for the reflection situation are computed (with constant fits) averaging on the scan values. The reflection efficiency can be estimated taking into account these mean and sigma average values instead of updating them each goniometer step.

Fig. 4.35 is the analogous of fig. 4.34 obtained taking into account the mean and sigma average value of the amorphous position in the initial and final part of the scan and the reflection one in the central part.

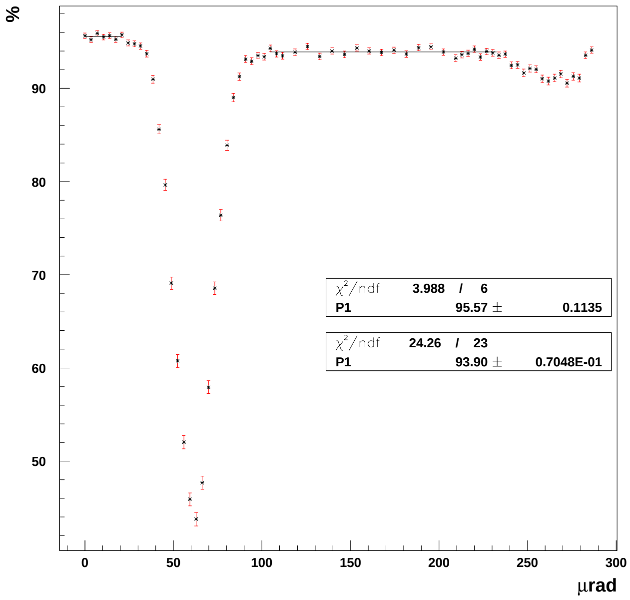

Figure 4.35: The plot shows the number of events within 3σ from the amorphous position (initial and final part of the scan) and the reflection one (central scan region) as a function of the goniometer angle. The two constant fits give the percentage of the events in the main peak (within 3σ).

The reflection efficiency value computed with the modified method is 98.25 ± 0.13% which is compatible with the 98.26% of the first version of the method. This result demonstrates the beam stability during reflection. Although the two methods seem to be equivalent, this second method makes the reflection efficiency definition stronger with respect to the reflection angle definition and less influenced by errors in the single gaussian fit.

The second possible objection to the proposed method regards the possibility that the gaussian shape of the beam profile is modified when in reflection.
The efficiency results have been computed considering a 3σ area around the peak, thus about 99% of the gaussian area which takes into account the majority of the events excluding the beam tails. But if the amorphous and the reflected peak have the same shape, the variation of this area shouldn't cause a significant variation in the reflection efficiency value.

Therefore computing the efficiency with different sigma values could underline on one hand an eventual dependence of the obtained value on this number and on the other a deviation from the gaussian shape during reflection. Such a behaviour should be included in the efficiency value as a systematic error. Fig. 4.36 shows the efficiency as a function of the number of sigmas computed between 1 and 4σ: a clear increasing trend with sigma is shown over 3σ which could be due to the beam tails and to the fact that the volume capture starts to be included. Below 3σ it is difficult to identify and explain a trend also because the errors are great; the intrinsic asymmetry of the reflection effect (see sec. 1.2.3) which here is almost hidden by the beam shape, and the multiple scattering can play a role that has been studied in the May 2007 beam test (chap. 5). Anyway the average value (98.15%) obtained by this σ-scan is compatible with the previous one confirming the reliability of the method.

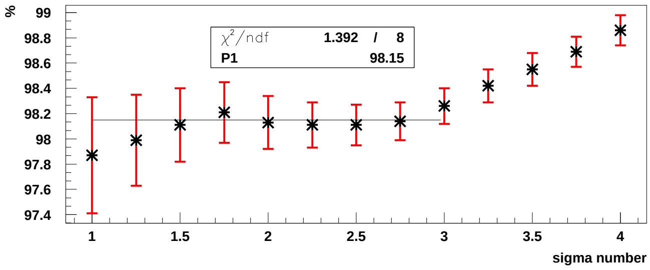

Figure 4.36: The reflection efficiency computed with the described method with different sigma values.

4.4.1.2 Channeling efficiency

The channeling efficiency can be evaluated by analogy with the reflection one counting the number of protons within 3σ from the channeling peak and comparing this number with the number of protons within 3σ from the amorphous peak. Fig. 4.37 shows the channeling peak trend for the ST4 crystal, its mean in the top plot and its sigma in the bottom one.

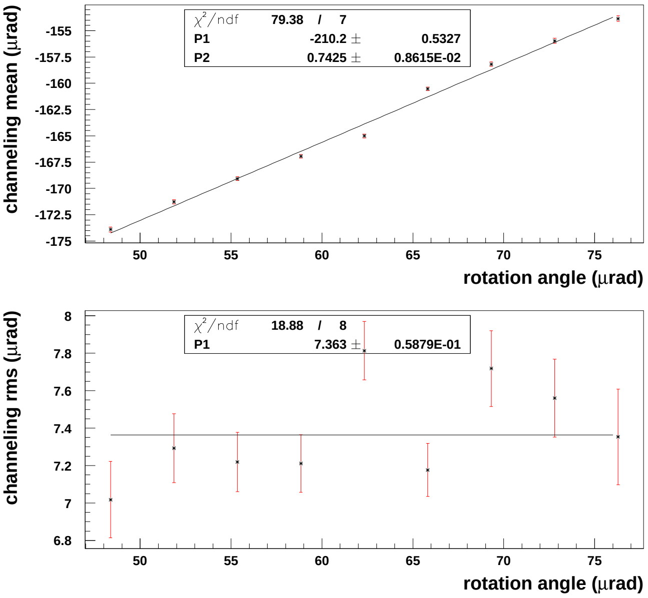

Figure 4.37: The channeling peak trend during the ST4 crystal scan: (top plot) its angular position, the points are the mean values of the gaussians that fit the peak and the error bars are the errors of the fit; (bottom plot) its rms trend, the points are the sigma values of the gaussian fits and the error bars are the errors of the fits.

The channeling peak position and width depend on the crystal rotation angle; for this reason, to obtain a better description of the area covered by the channeling peak, the mean and sigma values, that will define the boundaries of that area, have to be updated each goniometer step with the parameters of the fit (the data shown in fig. 4.37). Therefore this is the procedure to obtain the channeling efficiency:

- the total number of the events is normalized at each goniometer step;
- the events within 3σ from the amorphous peak are counted with the mean and sigma values updated each goniometer step; the average number of the events in the amorphous position is computed;

- the events within 3σ from the mean of the channeling peak are counted;
- the channeling efficiency is defined as the ratio between this last number and the previous one:

$$\varepsilon_C = \frac{N_{C(3\sigma)}}{N_{A(3\sigma)}} \tag{4.2}$$

Fig. 4.38 shows the channeling efficiency of the ST4 crystal as a function of the crystal rotation angle; the maximum efficiency value is $51.18 \pm 0.72\%$. The efficiency point trend is the result of the matching between the angular acceptance window of the crystal and the incoming beam divergence; the fit shows a good agreement with a gaussian function and it is remarkable that the gaussian σ is 10.7 μrad which is very close to the critical angle for silicon at this energy ($\theta_c \sim 10$ μrad).

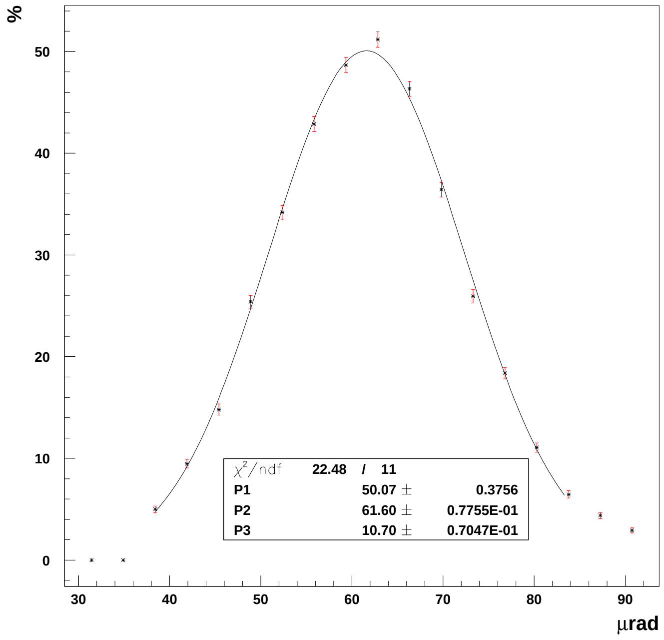

Figure 4.38: The channeling efficiency trend of the ST4 crystal as a function of the goniometer angle. The maximum value is $51.18 \pm 0.72\%$.

The channeling efficiency trend provides an unambiguous method to find the crystal rotation axis corresponding to the channeling maximum thus identifying the crystal bending angle. In the ST4 crystal the bending angle results to be $\theta_c = 157.63 \pm 0.18$ μrad.

Fig. 4.39 shows the trend of the maximum channeling efficiency as a function of the number of σ considered in the efficiency computation. An opposite trend with respect to the reflection case is shown: the efficiency decreases as the area considered for the measurement increases. The reason is that both the amorphous and the channeling peaks slightly deviate from the gaussian shape in the opposite direction: the amorphous peak has larger non gaussian tails while the channeling one (being extracted from the crystal) has sharper edges. Although the plot in fig. 4.39 is interesting, as it shows a different shape of the channeling peak with respect to the beam, it is not so much significant with respect to the efficiency value since differently from the reflection case the channeling peak is clearly separate from the amorphous one. According to this the 3σ choice seems a good compromise as it allows to integrate the majority of the channeling and amorphous events without taking into account the beam tails.

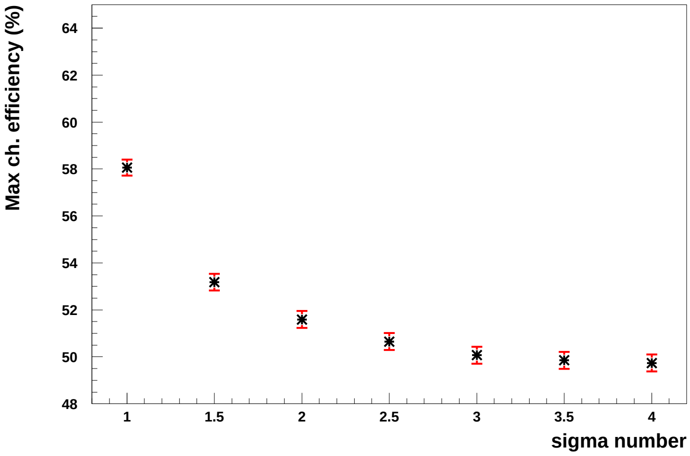

Figure 4.39: The channeling efficiency computed with the described method as a function of the chosen area (number of σ).

Finally it is interesting to note that the channeling efficiency trend is affected by the crystal torsion; fig. 4.40 shows the channeling efficiency trend of the ST4 crystal computed in a horizontal slice of 700 μm centered on the beam maximum. If compared with the one shown in fig. 4.38 the gaussian which fits the data is narrower ($\sigma = 9.72$ μrad) and higher ($P1 = 54.04$) meaning that the channeling angular acceptance has decreased while the efficiency has increased.

This depends on the crystal torsion; in fact when the beam impinges on a larger crystal area (in the vertical direction) it experiences different alignment conditions. This on one hand spreads the range in which particles can be channeled and on the other prevents the impinging beam to be all aligned at the same time with the crystal surface, reducing the maximum efficiency value.

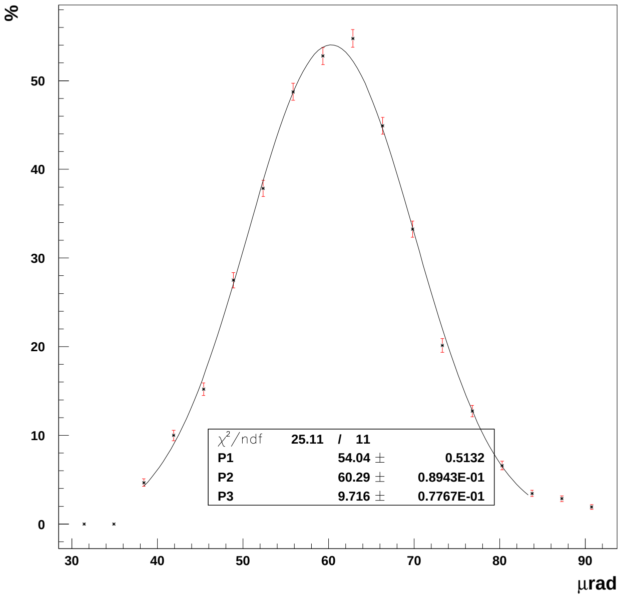

Figure 4.40: The channeling efficiency trend of the ST4 crystal (data from a horizontal slice of 700 μm) as a function of the goniometer angle. The maximum value is $54.76 \pm 0.97\%$.

4.4.1.3 Volume capture and dechanneling

Although most of the attention was dedicated to develop a reliable definition of the volume reflection and channeling efficiency, the estimation of the percentage of the events that go in the volume capture and dechanneling effects have been done.

The efficiencies are computed counting the number of particles which are in a region (of the phase space beam angle-rotation angle) identified as the volume capture or the dechanneling region. The procedures to determine the limits of these two regions are:

- *(dechanneling)* using the data from the fits, the areas within 3σ from the main and channeling peak are excluded; the dechanneling region is the area between the main and channeling peak;

- *(volume capture)* the volume capture peak is fitted with a gaussian function and the events within 3σ are counted.

Fig. 4.41(a) shows the dechanneling and volume capture regions underlined on the plot of the ST4 crystal scan while fig. 4.41(b) shows the number of events within 3σ of the volume capture peak (top) and in the dechanneling region (bottom).

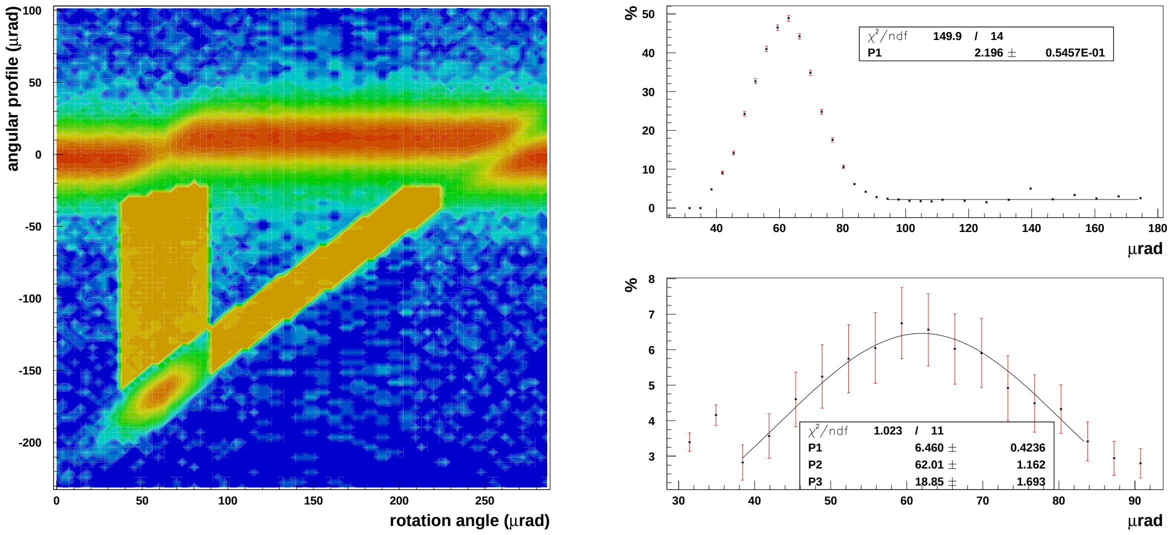

Figure 4.41: (a) The ST4 crystal scan: the beam angular profile, reconstructed as described in sec. 4.1, as a function of the goniometer angle. The regions in which the dechanneling and volume capture events are counted are underlined. (b) The number of events: in the volume capture region (top, also the events under the channeling peak are shown) and in the dechanneling region (bottom) where the events are fitted with a gaussian function; the total number of events of each goniometer step has been rescaled to 100.

The average percentage of the particles in the volume captured region is $\varepsilon_{vc}^{0} = 2.20 \pm 0.05\%$ while the one in the dechanneling one reaches the value of $\varepsilon_{d}^{0} = 6.46 \pm 0.42\%$.
These values overestimate the real volume capture and dechanneling efficiencies due to the background contribution of the main peak which is not negligible if compared to the low volume capture and dechanneling efficiencies.

To perform a background estimation the number of particles outside the main peak (from 3σ to $\pm$ 200 μrad) have been counted; the results are shown in fig. 4.42(b)

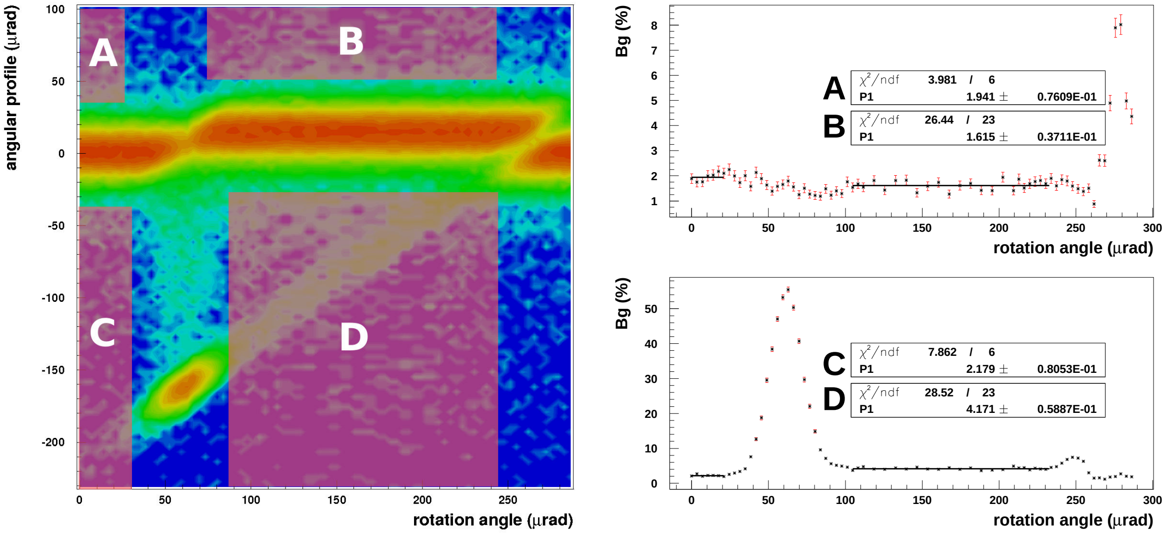

(a) (b)

Figure 4.42: Background estimation in the ST4 crystal scan: (a) the underlined regions correspond to the ones in which the events are counted the result is shown in (b) together with the fit values.

divided in four regions as schematically shown in fig. 4.42(a). The D region should be excluded since it includes the volume capture contribution. The C region is chosen to estimate the background level as it is on the same side of the volume capture and dechanneling with respect to the main peak thus no asymmetry in the background (originated by the beam) is expected. The average background level in this region is $B_c = 2.18 \pm 0.08\%$; the region starts from 3σ below the main peak (~ -30 μrad) and ends at -200 μrad so its extension is about $L_B = 170$ μrad. The background subtracted volume capture (dechanneling) efficiency is:

$$\varepsilon_{vc(d)} = \varepsilon^0_{vc(d)} - B_c \cdot \frac{L_B}{L_{vc(d)}} \tag{4.3}$$

where $L_{vc(d)}$ is the average region dimension of the volume capture (dechanneling) in the divergence beam profile (the vertical sections of the plot in fig. 4.41(a)):

- *volume capture*: $L_{vc} = 6 \cdot \sigma_{vc}$ where $\sigma_{vc} = 11.90 \pm 0.37$ μrad is the value computed with the gaussian fit of the volume capture peak and it is multiplied by 6 because the volume capture region is defined within $\pm 3\sigma$ from the peak;

- *dechanneling*: $L_d = \theta_{ch} - 3\sigma_{ch} - 3\sigma_{amo}$ where $\theta_c = -167.87 \pm 0.18$ μrad is the channeling angle while $\sigma_{ch} = 7.81 \pm 0.16$ μrad and $\sigma_{amo} = 10.09 \pm 0.04$ μrad are the main and channeling σ, since the dechanneling region is between the amorphous and the reflection peak.

According to these parameters, eq. 4.3 gives the following efficiencies: for the volume capture $\varepsilon_{vc} = \varepsilon^0_{vd} - B_{vc} = (2.20 \pm 0.05 - 0.92 \pm 0.03)\% = 1.28 \pm 0.06\%$; for the dechanneling $\varepsilon_d = \varepsilon^0_d - B_d = (6.46 \pm 0.42 - 1.46 \pm 0.05)\% = 5.00 \pm 0.42\%$ where the errors are only statistical. Both the angular and efficiency values obtained in the ST4 crystal analysis are collected in table 4.1.

V. reflection		**Channeling**		**V. capture** (ε %)
θ_r (μrad)	13.82 ± 0.06	θ_c (μrad)	157.63 ± 0.18 μrad	1.28 ± 0.06
$\Delta\sigma$ (μrad)	0.27 ± 0.05	σ_c (μrad)	7.36 ± 0.39	**Dechanneling** (ε %)
ε (%)	98.25 ± 0.13	ε (%)	51.18 ± 0.72	5.00 ± 0.42

Table 4.1: The measured ST4 parameters.

4.4.2 The QM2 Crystal

The efficiency analysis described in the previous section has been performed also for the QM2 crystal (fig. 4.43(a)); this section presents the results and the most significant plots. The analysis has been performed in a window of 4 mm^2 (selected with the first module information) to cut the beam tails and to reduce the background rate; fig. 4.43(b) shows the results of the QM2 scan with the selected events.

Fig. 4.44 shows the main (a) and channeling (b) peaks trend while the extrapolated angular parameters are summarized in table 4.2.

Fig. 4.45(a) is the QM2 crystal equivalent of fig. 4.35 for the ST4 one, therefore it presents the number of events within 3σ from the main peak as a function of the goniometer angle. The values used as the average position and sigma for the amorphous and reflection regions are the ones computed in fig. 4.44. The constant fit of the reflection points gives an efficiency of 98.90±0.13%. Fig. 4.45(b) shows the channeling efficiency trend of the QM2 crystal as a function of the goniometer angle. The maximun value reached is 51.53±0.5% corresponding to a channeling angle of 74.39 ± 0.15 μrad ($\sigma_c = 6.87 \pm 0.10$ μrad).

It is interesting to note that the points corresponding to the reflected particles in fig. 4.45(a) show a small (but significant with respect to the errors) increasing trend with the goniometer angle which for example is not present in the ST4 crystal scan (fig. 4.35). The QM2 crystal has a smaller reflection angle with respect

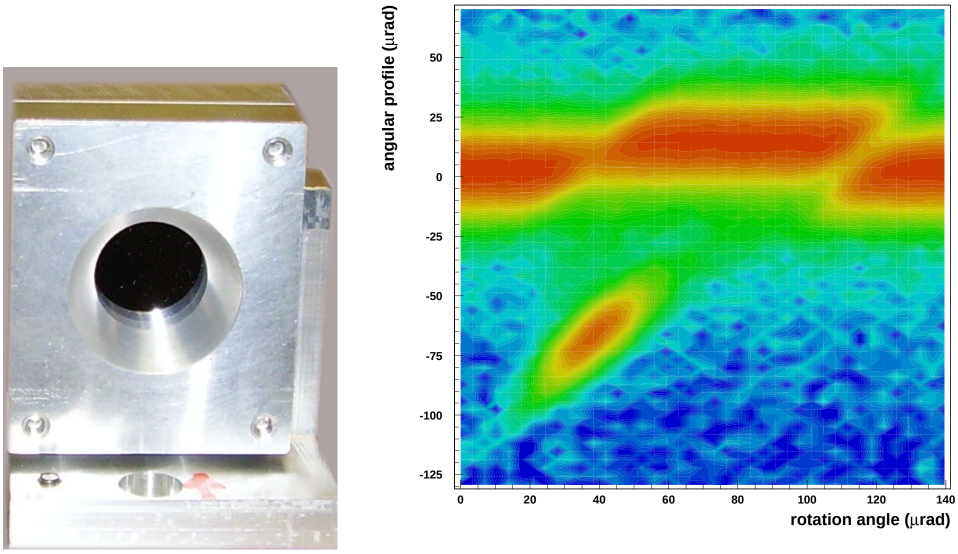

(a) (b)

Figure 4.43: (a) A photo of the QM2 crystal. (b) Bidimensional plot of the QM2 crystal scan, on the horizontal axis the crystal rotation angle, on the vertical one the angular beam profile.

to the ST4 one which implies a larger superposition between the reflected and the volume captured particles populations (see fig. 4.43(b)) especially for large goniometer angles, in the region where the two peaks are nearer. This gradual superposition explains the increasing trend present in fig. 4.45(a) and results in the overestimation of the volume reflection efficiency. Fig. 4.46(a) in fact shows that if the volume reflection efficiency is computed taking into account only the points before the increasing trend, the obtained value is $98.68 \pm 0.16\%$ which is smaller (apart from the errors) than the previous one. The same efficiency plot is also shown in fig. 4.46(b) but in this case it is computed taking into account the events within 2σ from the main peak. It is remarkable that on one hand the increasing trend has disappeared and on the other the resulting reflection efficiency is $98.56 \pm 0.19\%$ which is consistent with the value of fig. 4.46(a).

Following the method presented in the previous section, the volume capture and dechanneling efficiencies have been computed with the following results: $\varepsilon_{vc} = 2.16 \pm 0.15\%$; $\varepsilon_d = 1.42 \pm 0.39\%$.

Differently from the ST4 crystal in the QM2 case the volume capture probability is not totally consistent with the reflection efficiency as their sum exceeds 100% apart from the errors. The problem also in this case is due to the superposi-

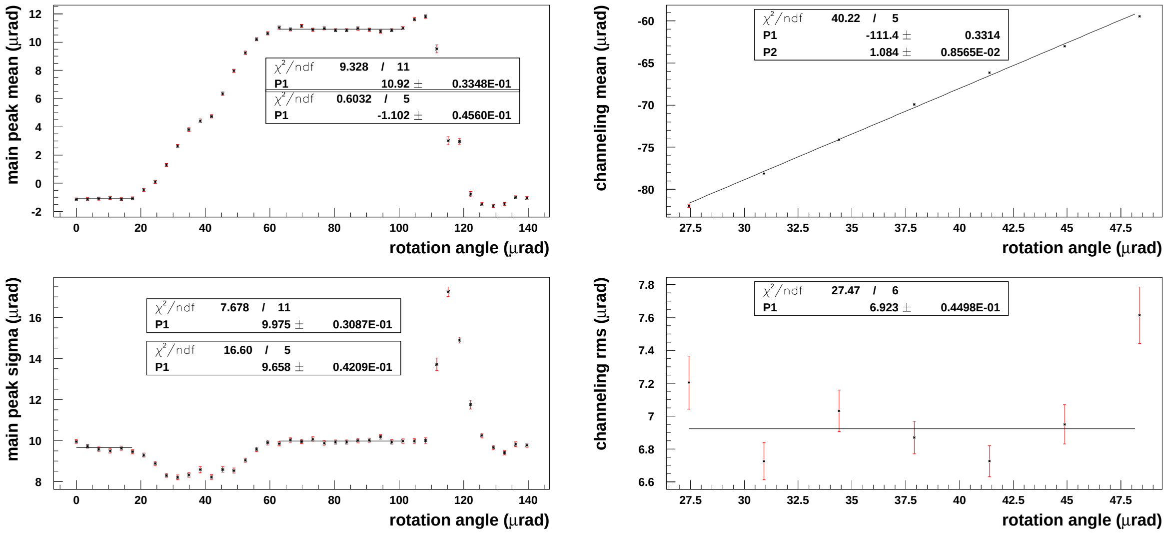

(a) (b)

Figure 4.44: Result of the systematic gaussian fit on the QM2 angular scan: (a) the main peak angular position (top plot) and its sigma trend (bottom plot); (b) the channeling peak angular position (top plot) and its sigma trend (bottom plot).

tion between the volume capture and the reflected peak clearly shown in fig. 4.47.

To limit this effect, the volume capture efficiency has been computed considering the events within 1σ of its peak (instead of 3 as shown in the ST4 case) multiplying the obtained number for $1/0.68$ to estimate the total value.

Anyway the final value obtained ($\varepsilon_{vc} = 2.16 \pm 0.15\%$) seems to overestimate the real volume capture efficiency because if added to the reflection efficiency the sum is slightly greater than 100%. Probably the reason is that in the background subtraction procedure the background in the amorphous position is taken into account assuming that it is equivalent to the reflection position one. But the reflection peak could have a higher tail in the volume capture side due to its small asymmetry (intrinsic in the reflection phenomenon). This small asymmetry can be important in the volume capture efficiency evaluation in the QM2 case as the volume capture peak is superimposed to the reflection peak tail as it is shown in fig. 4.47.

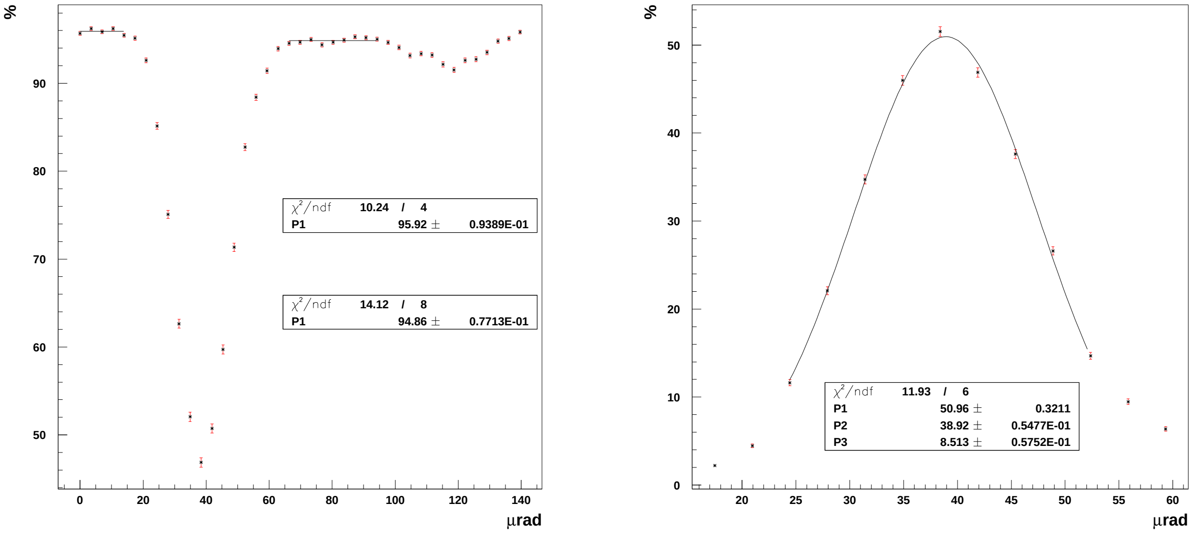

(a) (b)

Figure 4.45: (a) Number of events within 3σ from the main peak as a function of the goniometer angle. (b) Number of events within 3σ from the channeling peak as a function of the goniometer angle rescaled to the number of events in the amorphous peak.

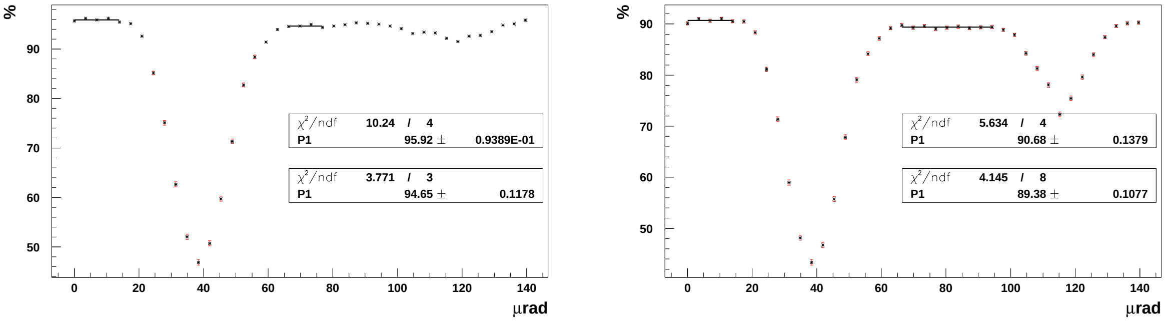

(a) (b)

Figure 4.46: Number of events within 3σ (a) (2σ (b)) from the main peak as a function of the goniometer angle: (a) only the first points of the reflection are taken into account to compute the reflection efficiency, $\varepsilon_r = 98.56 \pm 0.19\%$; (b) the reflection region points form a plateau which fitted gives an efficiency of $\varepsilon_r = 98.68 \pm 0.16\%$.

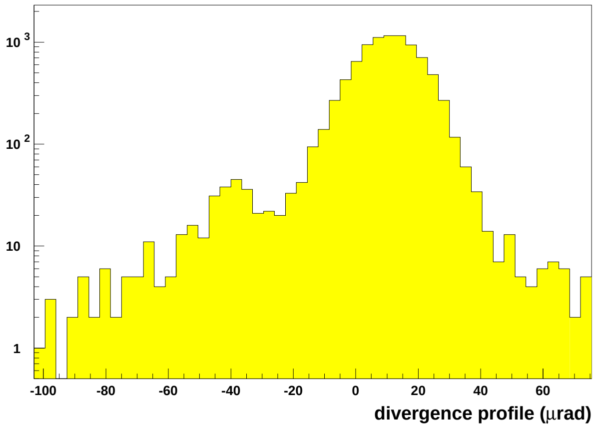

Figure 4.47: A frame of the QM2 scan in logarithmic scale; the volume captured peak is small compared to the reflected beam tail.

V. reflection		**Channeling**		**V. capture** (ε %)
θ_r (μrad)	12.04 ± 0.06	θ_c (μrad)	74.39 ± 0.15	2.16 ± 0.15
$\Delta\sigma$ (μrad)	0.37 ± 0.05	σ_c (μrad)	6.87 ± 0.10	**Dechanneling** (ε %)
ε (%)	98.25 ± 0.13	ε (%)	51.53 ± 0.5%	1.42 ± 0.39

Table 4.2: The measured QM2 parameters.

4.4.3 Double crystal

Fig. 4.48(a) shows the double crystal scan. The channeling peak is present since the first frame of the scan; this implies that the reflection efficiency has to be computed in comparison with the last frame of the scan.

Fig. 4.48(b) shows the main peak mean and sigma trend during the double crystal scan; it is evident that both in the reflection and in the amorphous position there aren't stable angular positions to be fitted with a constant to obtain an average reflection angle. The reflection angle can be computed between two frames of the scan: for the reflection one a position in which the channeling peaks are absent is chosen (fig. 4.49(b)) while for the amorphous one the first position of the scan is taken into account (fig. 4.49(a)), as it is the farthest from the reflection peak (see fig. 4.48(b)) and so the nearest to the effective amorphous position. A small channeling peak is present; therefore the extrapolated reflection angle could

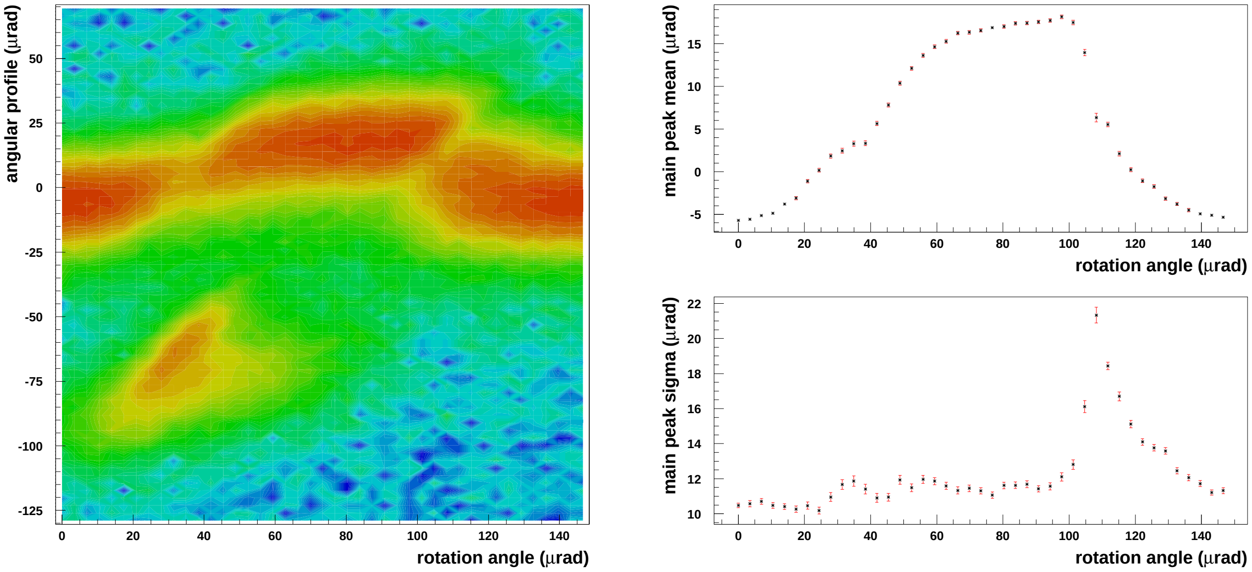

(a) (b)

Figure 4.48: (a) Bidimensional plot of the double crystal scan (angular profile method). On the horizontal axis the crystal rotation angle; on the vertical axis the position beam profile. (b) The main peak angular position (top plot) and its sigma trend (bottom plot).

slightly underestimate the effective reflection angle, a fact that will be checked further on.

The reflection efficiency measurement cannot be performed with the second method (taking into account the average parameters) because the reflection angle is defined from the first scan position but this position cannot be taken into account to compute the efficiency as the channeling peak is present (the computed value would largely overestimate the effective one). According to this, the measurement will be performed following the first method (updating the cut limits at each goniometer step with the fit information).

Fig. 4.50 shows the number of events of the main peak as a function of the goniometer angle. The reflection efficiency obtained in this way is 95.74±0.42%.

The same efficiency measurements have been performed with the data from the beam vertical slice shown in fig. 4.30(a) which, as described in sec. 4.3.2, presents a better crystals alignment.

The double crystal behaviour in this beam slice is represented in fig. 4.51(a) while the (b) plots show the main peak trend. Unlike fig. 4.48(b) which represents

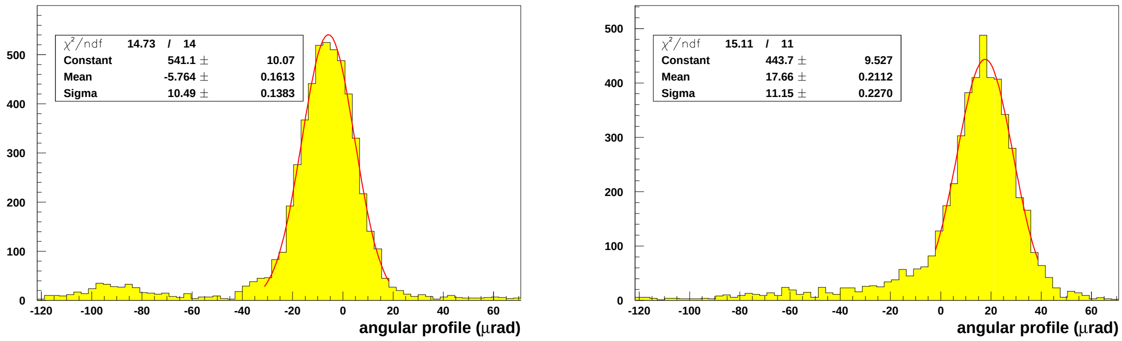

(a) (b)

Figure 4.49: Two frames of the double crystal scan (fig. 4.48): (a) the nearest to the amorphous position; (b) the one in full reflection; the reflection angle computed as the difference between the two mean values is 23.42 ± 0.27 μrad.

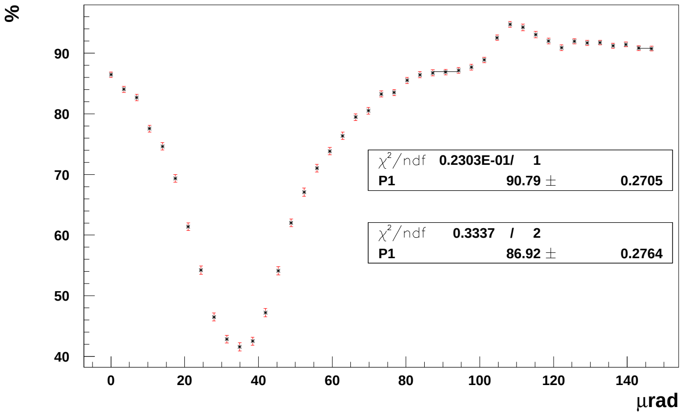

Figure 4.50: The plot shows the number of events within 3σ from the main peak as a function of the goniometer angle; the mean and sigma values are the ones from the fits shown in fig. 4.48(b) for each goniometer step.

the whole data, here both in the reflection and in the amorphous position, there are stable angular positions to be fitted with a constant giving a reflection angle of 23.50 ± 0.20 μrad which is consistent with the value measured with the complete data set.

Thanks to both the angular stability in reflection and a clear amorphous region

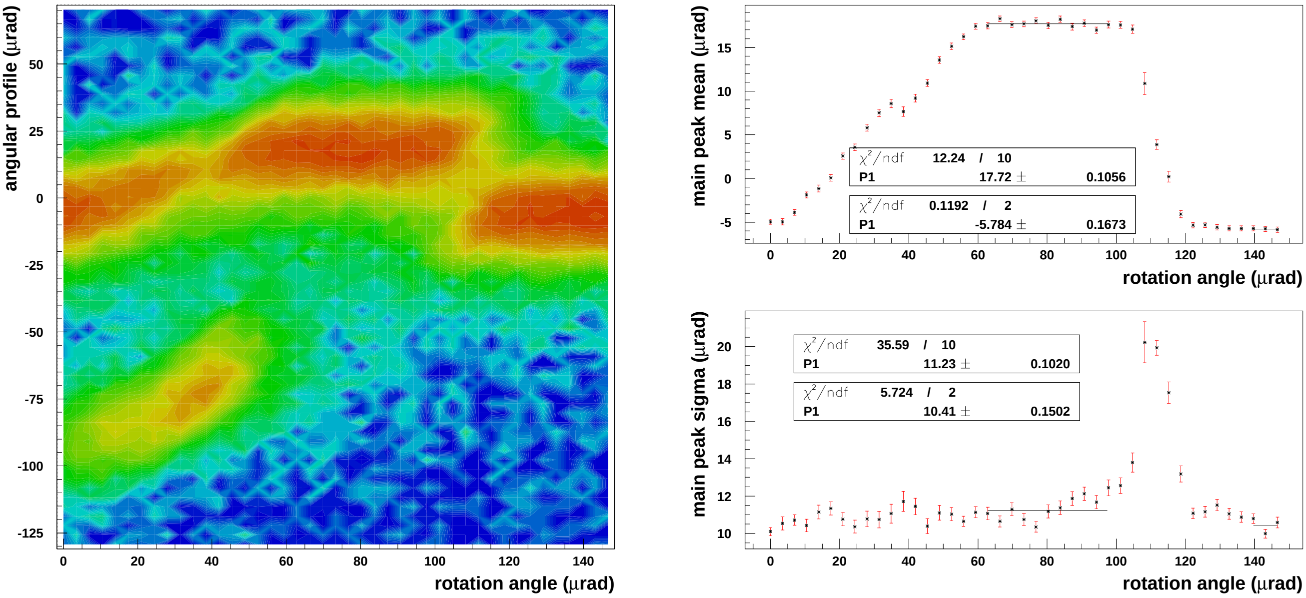

(a) (b)

Figure 4.51: (a) Bidimensional plot of the double crystal scan selecting the lower beam region. On the horizontal axis the crystal rotation angle; on the vertical axis the position beam profile. (b) The main peak angular position (top plot) and its sigma trend (bottom plot).

the efficiency measurement can be performed with the second method. Fig 4.52 presents the number of events within 3σ from the main peak as a function of the goniometer angle. The values used as the average position and sigma for the amorphous and reflection regions are the ones computed in fig. 4.51. The constant fit of the reflection and amorphous points gives an efficiency of 96.87±0.55%. This value shows that a better alignment besides increasing the crystals angular range of complete double reflection slightly increases its efficiency; this is due to the perfect superposition of the channeling peaks which prevents a fraction of the beam from being channeled during reflection.

The alignment difference between the two presented cases (all data and data from a small horizontal slice) should be of the order of 10 μrad (this can be deduced from the measurements on the single crystal, sec. 4.3.1) and the effect of this difference on the efficiency does not seem crucial in the two crystal case ($\sim$ 1%); a more complicated situation can be foreseen if the crystals number increases. In fact, apart from a small decrease of the reflection efficiency, in the misaligned case (all data) the full reflection is reached in a smaller goniometer angular range (fig. 4.48) if compared to the single crystal of the most aligned case. This essentially happens because one of the channelings is extended by the reflection interference of the other crystal (sec. 4.3.2).

It is therefore probable that when the number of crystals increases the full reflection cannot be reached without a perfect alignment which turns out to be the only way to maintain a high reflection efficiency increasing the reflection angle using a multicrystal setup.

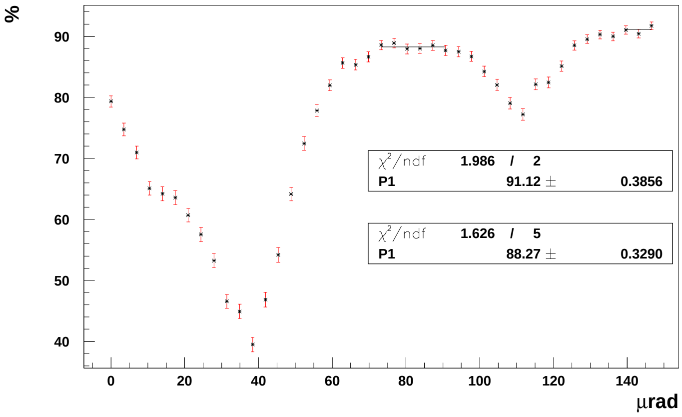

Figure 4.52: The plot shows the number of events within 3σ from the amorphous position (in the external regions) and the reflection one (in the middle region) as a function of the goniometer angle; in both cases, each goniometer step, the total number of events is normalized and rescaled to 100. The measured reflection efficiency is 95.74±0.42%.

Finally it is possible to correlate the reflection efficiency and the reflection angle of the single crystal with those of the double one. The reflection angle should be the sum of the reflection angles of the single crystals. The reflection efficiency is defined as the proton probability of going into reflection, expressed as a percentage. Therefore in the double crystal, if the two reflection processes are independent, the double reflection efficiency should be computed as the product of the single crystal efficiencies.

In this case the two crystals are QM1 and QM2, the reflection angle (efficiency) of the first one has not been computed in the framework of this thesis, but it has been analyzed in an equivalent way using the data from the AMS silicon microstrip detectors (the corresponding values are presented in table 4.3).

The obtained reflection efficiency value is 96.51±0.42% whose consistency with the measured value (maximum alignment case) is an excellent proof of both the reliability of the analysis method and the possibility of producing multicrystal deflectors. The relevance of this technique is that, once a good alignment is found, the multicrystal reflection properties can be extrapolated from the single crystal characteristics.

	θ_r (μrad)	ε_r (%)
All	23.42 ± 0.27	95.74 ± 0.42
Max alignment	23.50 ± 0.20	96.87 ± 0.55
QM2	12.04 ± 0.06	98.68 ± 0.16
QM1	11.90 ± 0.04	97.80 ± 0.40
QM2+QM1$_{th}$	23.94 ± 0.07	96.51 ± 0.42

Table 4.3: The double crystals reflection parameters summarized and compared to the theoretical values computed from the single crystal measurements.

Chapter 5

The May 2007 beam test

The September 2006 beam test described in the previous two chapters gave valuable results, leading to plan a series of new experiments on the H8 beamline. In this chapter the past experiment results will be summarized and used as the starting point to define the requests for the next beam tests, which are addressed to both the measurement apparatus upgrade (sec. 5.2) and a new crystal design (sec. 5.3).

A description of how these requests have been fulfilled during the last May 2007 beam test will be given; the advantages of the new measurement setup will be discussed and some preliminary results obtained with the new crystals will be presented.

5.1 Going beyond

The results of the September 2006 beam test can be summarized as follows:

- the measurement apparatus (detectors and goniometer) allowed to investigate the channeling and the other related effects with unprecedented precision; both the angular parameters and the efficiency ones have been computed and it was possible to investigate the homogeneity of the crystal behaviour with respect to its different regions;

- the volume reflection has been observed for the first time at this energy showing its great efficiency and angular acceptance in agreement with the simulation expectations; these features suggest to exploit the volume reflection to develop a collimation system which should be characterized by a high efficiency;

- the double reflection has been observed; this first investigation on the multireflection turned out to be a fundamental ingredient in the collimation system development since the volume reflection angle of a single crystal is too small to satisfy the collimation requirements.

The last item in the previous list suggests that the next experiments should verify the possibility of a multiple reflection defining an ideal crystal design and mechanical support; in this framework the crystals tested in the May 2007 beam test are briefly described in sec. 5.3 together with some preliminary results.
For what concerns the experimental apparatus, although the old system allowed to obtain good results, the experience of the September beam test resulted in the development of a new detectors system capable of:

- increasing the single particle deflection angle global resolution in order to achieve a clearer separation of the different crystal effects to make the measurements independent from the beam characteristics. Sec. 4.1 shows how using the information of a detector placed near the crystal the effects due to the beam dimension at the crystal can be neglected even if the beam divergence can still influence the result; this is particularly important considering that the measured beam divergence is at least twice the expected one (as shown in sec. 3.1.1);
- having a good spatial resolution on the particle impact point on the crystal surface to be able to precisely select the crystal (if it is smaller than the beam) or a region of it if necessary;
- making the experimental procedure to analyze a crystal fast enough reducing the dead times.

The next section describes the way these requests have been fulfilled.

5.2 Setup upgrade

The old measurement apparatus was composed of many detectors (as described in sec. 3.1.2) but it essentially allowed to measure the particle outcoming angle through the detection of the particle position near the crystal and far from it (in the downstream region at about 70 m). According to this its scheme can be reduced to the one presented in fig. 5.1(a) where the black box represents all the effects which disturb the measurement of the outcoming angle such as the multiple scattering, the angular spread induced by the bending magnets, the position of the first module (upstream AGILE detector) which is not really next to the crystal. The final angular distribution will depend on the initial beam divergence, the “black box” contribution, the detector resolution and finally on the crystal deflection which is hidden by the other effects. The weights of the different “disturbing” contributions are approximately 8 μrad for the incoming beam divergence, 4 μrad for the black box effects and since the detectors resolution is ~ 20 μm, the angular resolution will be about $(20\ \mu\text{m}/70\ \text{m})\sqrt{2} = 0.4$ μrad. Being these effects independent they add in quadrature, thus the beam divergence is the dominant effect while the angular resolution contribution can be neglected.

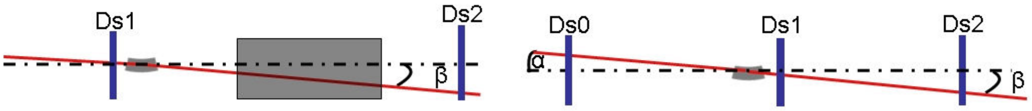

(a) (b)

Figure 5.1: (a) A simplified scheme of the September 2006 setup: two detecting stations allow the measurement of the outcoming particle angle β (the black box represents the multiple scattering due to the material between the two detector stations). (b) The new setup reconstructs both the incoming (α) and outcoming (β) particle angle so that the deflection angle $\gamma = \alpha - \beta$ can be computed.

Several steps have to be performed to improve the resolution on the single particle crystal deflection angle measurement: the beam divergence influence should be eliminated measuring the incoming particle angle; the black box contribution which was the dominant element should be limited; the angular resolution should be maintained negligible. Fig. 5.1(b) shows that adding a third detecting station before the crystal both the incoming (α) and the outcoming (β) particle angle can be measured so that the deflection angle ($\gamma = \beta - \alpha$) can be directly observed thus removing the influence of the beam divergence.

The resolution on the deflection angle is at this point determined by the angular dispersion between the first and the third detector (due to the multiple scattering and the eventual magnet crossings) and by the intrinsic detector spatial resolution. The angular spread has been minimized both moving the experimental setup in a beamline section without bending magnets between the crystal and the detectors and limiting the material thickness crossed by the particles. Between the two external detectors, in fact, there are only the 4 windows which interrupt the beam pipe vacuum to put the detector and the goniometer, the air relative to these interruptions and the central detector which being double sided allows the position measurements in both the directions introducing only 300 μm of silicon in the particle path.

Fig. 5.2(a) shows an image of the silicon detector placed before the crystal to measure the incoming angle; the tracking system is composed of four detectors of the same type positioned as in fig. 5.2(b). There are three measuring stations, one before, one next to and one after the crystal, the last of which is composed of two detectors, so to the basic scheme presented in fig. 5.1(b) a detector is added at the end of the setup. This one does not add a multiple scattering contribution and is used to have a redundant measurement of the position after the crystal. Note that the detector setup allows to use the analysis procedure presented in sec. 4.1 with the addition of a new detector before the crystal.

The detectors are four modules of silicon microstrip telescopes developed by INFN Trieste [68]; each module (the box is 12×50 cm^2 and 4 cm thick) consists of a silicon strip detector and its readout electronics. The detector sensitive area (1.92×1.92 cm^2) is a double sided high resistivity silicon microstrip detector, 300 μm thick. The p-side of the detector has a p+ implantation strip every 25 μm and a readout pitch of 50 μm while the n-side (which is perpendicular to the p-one) has n+ implantation strips every 50 μm, separated by p+ blocking strips. The p-side which has the best resolution (thanks to the presence of a floating strip) has been used to measure the horizontal direction in which the crystal deflection takes place. Each detector side has 384 DC-coupled strips; the AC coupling to the electronics is performed with external quartz capacitors. The strips are readout by 3 low noise VA2 (IDEAS) ASICs with a multiplexed readout at 5 MHz; they are glued on a thin substrate of ceramic which provides the distribution of the digital control signals to the ASICs and takes the analog ones to the frontend electronics (the so called repeater boards), which is located near the detectors.

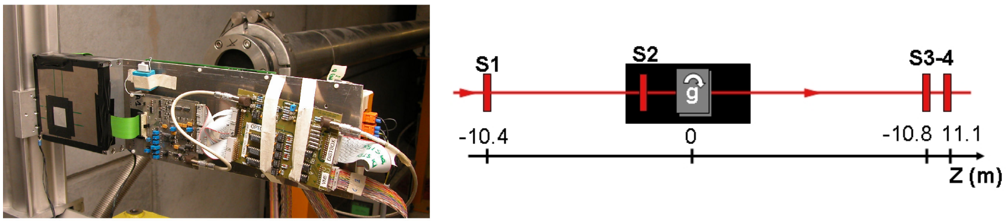

(a) (b)

Figure 5.2: (a) A photo of the silicon telescope mounted on the H8 beamline together with its electronics. (b) The May 2007 beam test setup.

Fig. 5.3 shows a silicon telescope residual; the resolution is about a factor 3.5 better than the AGILE silicon chambers one. The use of a high resolution detector system was necessary to measure the incoming and the outcoming angle with a relatively compact system and perform a precise measurement of the particle impact position on the crystal surface. A compact system was a mandatory request for two reasons: it allows the possibility to use a higher frequency readout clock (because the cables are shorter) and thus a higher rate for the data acquisition and it fits the beamline setup.

The higher spatial resolution on the particles impact point on the crystal sur-

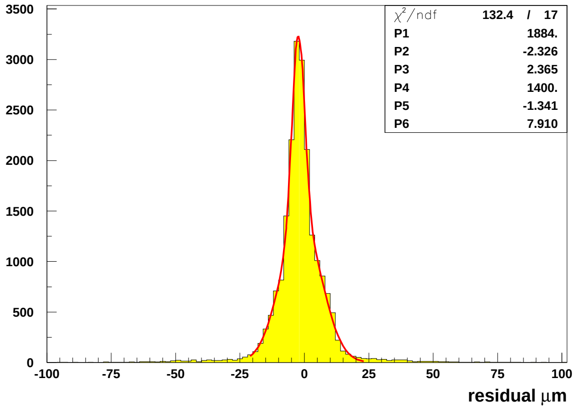

Figure 5.3: The residual of a silicon telescope. The distribution is fitted with the sum of two gaussians with σ=2.4 and 7.9 μrad; the average σ value (weighed on the gaussian areas) is 6.3 μrad.

face with respect to the one of the old setup is provided by both the higher detectors resolution and the proximity of one of them to the crystal.

Sec. 5.2.1 will summarize in a few points the comparison between the two setups while sec. 5.2.2 will show how the new system has simplified the experimental procedure to analyze the crystals.

5.2.1 Higher precision

As stated in the previous section the new measurement system is designed to reconstruct the crystal deflection angle instead of simply measure the particles outcoming angle from the crystal; its single particle deflection angle resolution is therefore independent from the beam divergence and is determined by the multiple scattering and by the detector resolution. Fig. 5.4(a) shows the distribution of the measured deflection angle without any crystal: the rms of this distribution represents the global resolution of the system and is about 3.5 μrad (to compare with 9 μrad that was the rms of the outcoming angle distribution (sec. 3.1.1)).

Fig. 5.4(b) shows the result of the scan of the QM2 crystal (the analysis of this crystal with the old setup is presented in chap. 4) with the new system; if compared with an old scan (see fig. 4.43), the different crystal effects appear more defined and separate. Fig. 5.5 compares the distribution of the outcoming angles in the amorphous and reflection position measured with the old setup (a) with the distributions of the deflection angle acquired during the last beam test (b); the

QM2 crystal is analyzed in both cases. The rms of the deflection angle distribution in the amorphous position (5.5(b)) is 4.72 μrad and it is the sum of the system resolution (fig. 5.4) and the multiple scattering of the crystal itself which adds in quadrature; the multiple scattering inside the crystal represents an intrinsic limit in the achievable deflection angle resolution. The QM2 width is 0.82 mm (table 3.2) meaning that the effective resolution of 4.72 μrad is not so far from the physical limit especially considering that the QM2 crystal is one of the thinnest crystals ever analyzed.

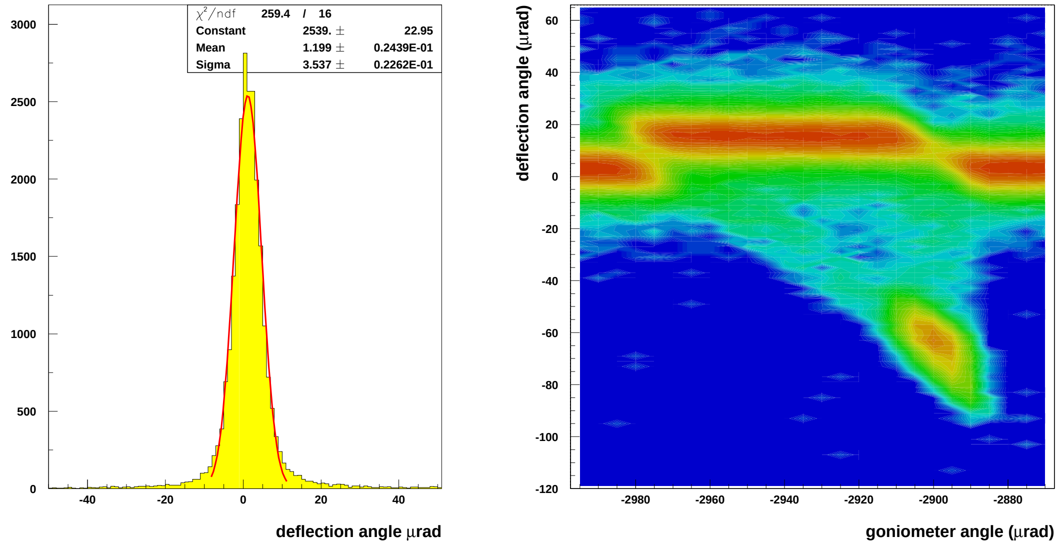

(a) (b)

Figure 5.4: (a) The deflection angle distribution measured by the silicon telescope without any crystal in place. (b) The QM2 crystal scan obtained with the silicon telescope.

5.2.2 Faster

Besides the better resolution the new setup has simplified and sped up the crystal analysis procedure. This has been possible for three reasons:

- the high resolution achieved by the system which makes it very sensitive to the crystal effects; as pointed out in the previous section, for example, the multiple scattering of one of the thinner crystals is clearly visible;
- the acquisition rate (5 kHz) which allows to acquire 10k events per spill;

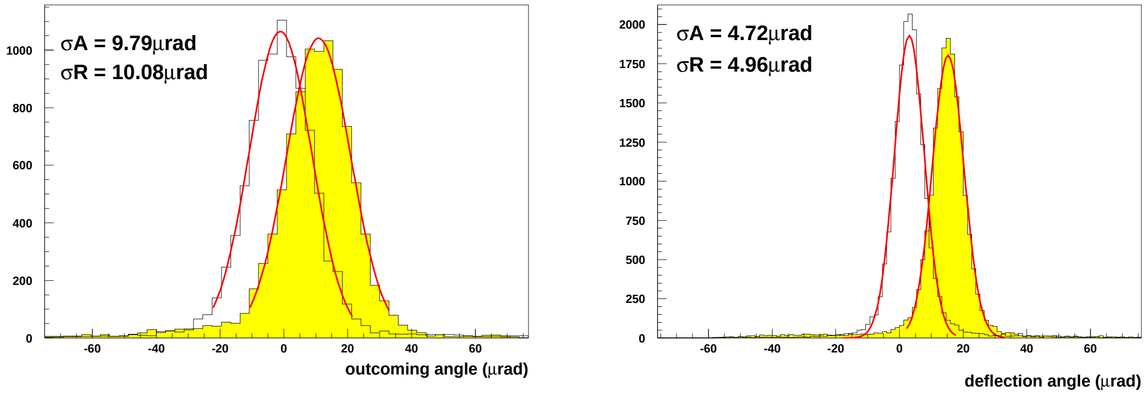

(a) (b)

Figure 5.5: A comparison between the performances of the September 2006 setup and the May one; the amorphous and reflection positions have been taken from the QM2 crystal scan: (a) the outcoming angle reconstructed with the silicon chambers; (b) the deflection angle measured by the silicon telescopes.

- the high integration level between the goniometer, the DAQ and the online analysis allows to acquire data (during the spill), move the goniometer (in the time between the different spills), while an automatic analysis procedure shows the results.

These features avoid the lateral alignment with the lead strip and the fast angular scan performed with the gas chamber to find the channeling orientation. These procedures described in sec. 3.2 which required a lot of time and beam stops have been substituted by the equivalent ones performed with the silicon telescope system in less time.

Fig. 5.6 shows the result of a lateral scan performed with the telescope to center a strip crystal on the beam; the passage of the crystal is visible as an increase of the deflection angle (due to the multiple scattering of the crystal itself) in the beam region which impinges on the crystal. This method allows to choose a particular beam region for example avoiding a dead strip of the detector near the crystal.

Once the crystal is on the beam a fast angular scan can start (without a beam stop to remove the lead strip) to determine the channeling orientation. The result of a fast angular scan performed with the silicon telescope is shown in fig. 5.7; in this case the goniometer has been set to scan an angular region of ±750 μrad around the angular position obtained with the optical pre-alignment. The angular step was 25 μm which means a total of 60 steps; since each step can be carried out in one beam cycle (16.8 s) about 17 minutes are required to complete the scan.

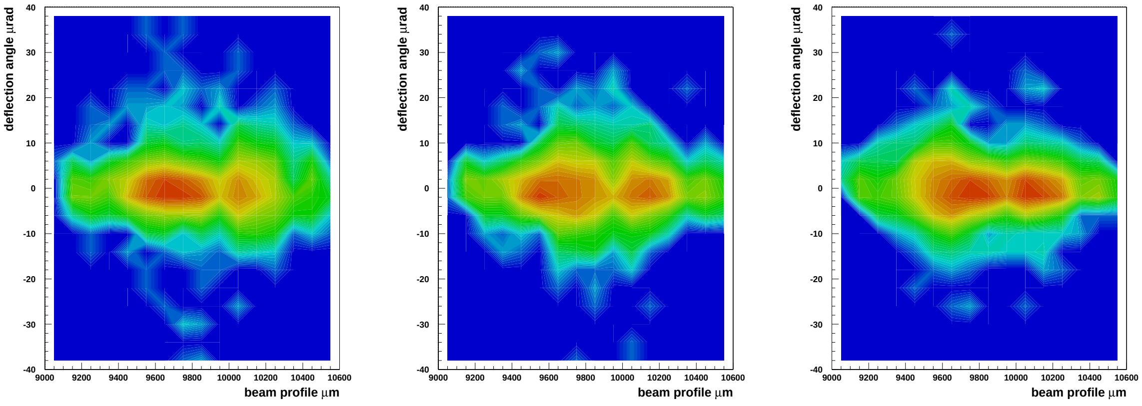

(a) (b) (c)

Figure 5.6: An example of a lateral scan performed with the silicon telescope: from (a) to (c) the crystal (500 μm wide and 2 mm thick) is moving from the right to the left of the beam profile; it is recognizable since it increases the deflection angle due to the multiple scattering.

It is interesting to note that the online analysis (which produces almost instantly the plot in fig. 5.7) can be used to interrupt the fast angular scan if the interesting region is revealed before the end of the scan thus saving time (in the presented case, for example, the scan region has been reduced to 675 μrad).

5.3 New Crystals

A study of the volume reflection has been performed during the September 2006 beam test indicating two important aspects for a possible implementation of a crystal collimation based on the volume reflection effect: the reflection efficiency is very high (98% at 400 GeV and it should increase at higher energy); the multiple reflection is an achievable task and it allows to increase the reflection angle.

According to these considerations, if for example 5 crystals are aligned for the volume reflection a deflection angle of $\theta_d = 5\theta_r \sim 65$ μrad is expected with a deflection efficiency of $\varepsilon_d = 98\%^5 \sim 90\%$, which means a deflection angle of the order of magnitude of the channeling one with a higher efficiency and more important with an angular acceptance which depending on the bending angle can be kept larger than the channeling one and independent from the particles energy.

Fig. 5.8(a) shows the multiple reflection working principle in crystals perfectly aligned with respect to each other: when the first crystal is in reflection it deviates

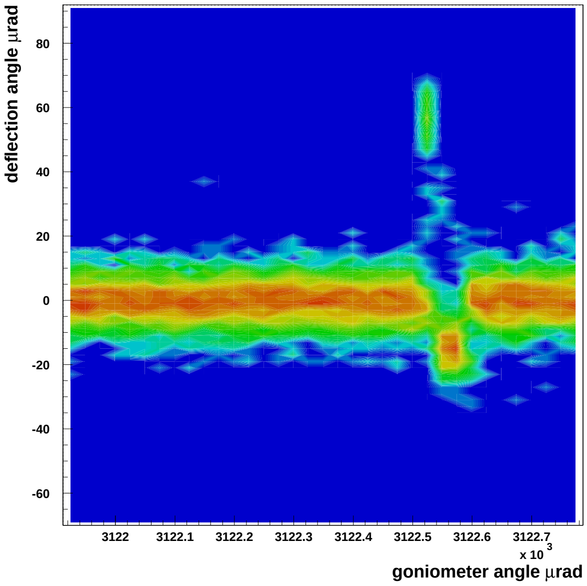

Figure 5.7: An example of a fast angular scan with the silicon telescope; the angular region is 675 μrad wide and the goniometer step is 25 μrad.

the beam of an angle θ_r which is smaller than the bending angle θ_b; as this angle corresponds to the reflection angular acceptance, the second crystal is still aligned to reflect the beam. The effect of the reflection in the previous crystal is that the tangency point in the following crystal volume moves from the end to the beginning of the curvature. Therefore the number of reflections achievable with this alignment is of the order of θ_b/θ_r which for the bending angles involved gives about 10 crystals. Fig. 5.8(b) shows that, if the crystals are progressively rotated of an angle equal to the volume reflection angle, the tangency point of the particles in the channel can be maintained at the same depth in the crystal volume. The andvantage of this relative shift is that in principle a greater number of crystals can be aligned and more important that the total angular acceptance does not decrease with respect to the single crystal.

Fig. 5.9 shows two examples of multicrystals mounted on their holder; they are based on quasimosaic crystals (a) and strip ones (b). This last exploits the bending system (described in sec. 3.1.4.1; normally used to bend the single strip) to bend 8 strips at the same time so that the crystals should have the same alignment with respect to the beam (as shown in fig. 5.8(a)). The quasimosaic crystals (fig. 5.9(a)) instead are mounted in a more complex holder which provides the curvature for

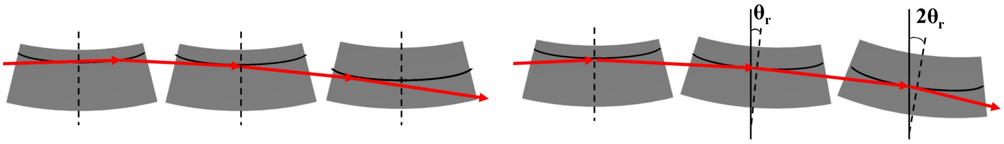

(a) (b)

Figure 5.8: Three crystals aligned for multireflection: (a) they have the same alignment with respect to the beam; (b) they are progressively rotated of an angle equal to the volume reflection angle θ_r.

each crystal and is able to vary the alignment between the different crystals acting on the screws visible in the photo.

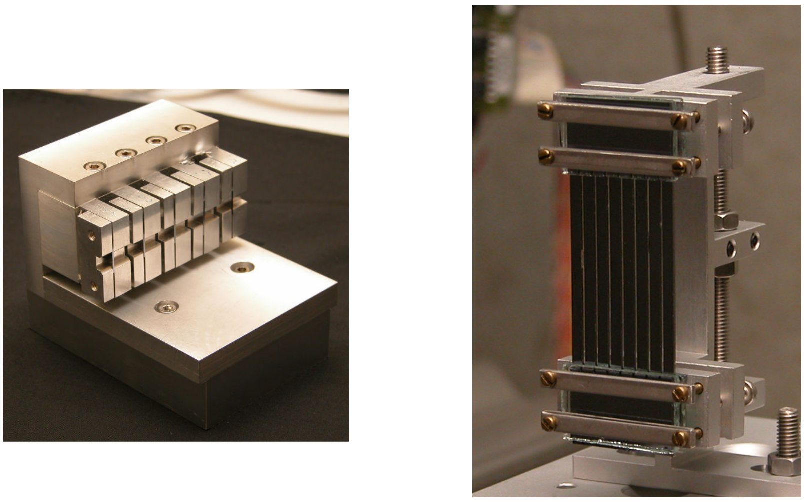

(a) (b)

Figure 5.9: The multicrystals mounted on their holder: (a) 5 quasimosaic crystals mounted in a holder which allows to adjust their relative alignment; (b) 8 silicon strip crystals bent by the same holder.

Both these crystal types have shown interesting and positive results during the beam test. In the following only the results of the quasimosaic crystal (called MQM5) will be commented as its possibility of varying the alignment between the crystals probably will be a request for all the multicrystal systems in the next test.

The alignment of the MQM5 crystal was a complex procedure in which the ability of the detector system in performing fast angular scans with an almost online data analysis turned out to be crucial. Fig. 5.10 shows two phases of the MQM5 alignment procedure. Fig. 5.10(a) presents a fast angular scan in which the

5 channeling peaks are separate and no multireflection is visible. The crystals are misaligned and measuring the distance between the channeling peaks the relative misalignment can be computed. Once this operation has been done, the beam is stopped and the screws on the holder are rotated to vary the alignment between the crystals as a function of the measured misalignment. This operation is repeated for a number of times because a feedback on the results of the action performed on the holder is needed. Fig. 5.10(b) shows a fast angular scan in which the alignment between the different crystals is better than the one shown in fig. 5.10(a) but not perfect.

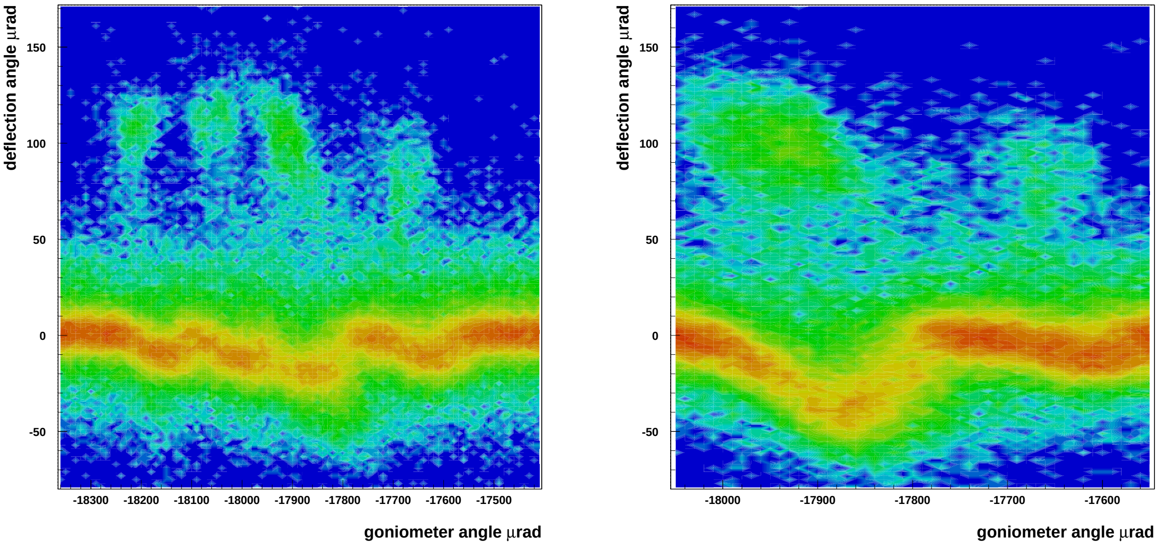

(a) (b)

Figure 5.10: Two fast angular scans of the MQM5 crystal: (a) the 5 channeling peaks are separate and observable, the crystals are not aligned; (b) after some interventions on the holder four channeling peaks are partially superimposed, the crystals are almost aligned. The data belong to the central portion of the beam profile in a window of 650×800 μm^2.

Finally, fig. 5.11 shows an angular scan of the MQM5 crystal performed once the alignment between the different crystals is almost perfect; this can be appreciated by the superposition of the different channeling peaks. Fig. 5.11(b) shows the deflection angle distribution measured when the crystal is in the amorphous position (white plot) and in reflection (coloured plot). The data relative to this crystal are at the moment under analysis but as a preliminary result a deflection angle of about 50 μrad can be estimated with an efficiency above 90% which is a result compatible with the expectations.

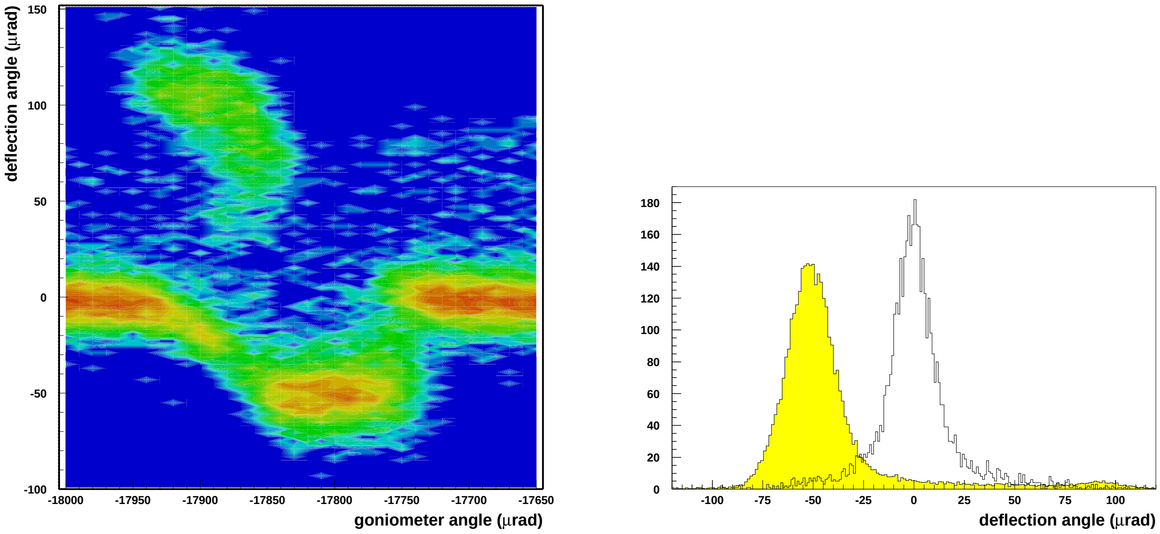

(a) (b)

Figure 5.11: (a) The angular scan of MQM5 with its 5 crystals aligned; (b) the deflection angle distribution measured when the crystal is in the amorphous position (white plot) and in reflection (coloured plot). The data belong to the central portion of the beam profile in a window of 650 × 800 μm^2.

Conclusions and outlooks

The adventure of this thesis started with the setup of the experiment performed by the RD22 collaboration on the SPS H8 beamline. The goal of this collaboration is the development of a collimation system for LHC based on the crystal channeling phenomena, which should allow the machine to reach its nominal luminosity. The beam test, which took place in September 2006, was performed to obtain an accurate study of the last crystal generation, testing both the strip and the quasimosaic crystals.

The experimental setup allowed an unprecedented precision, thanks to the track reconstruction performed by silicon microstrip detectors and an ad-hoc designed goniometric system.

During the experiment the volume reflection phenomenon has been observed for the first time at this energy: it is an impressive shift of almost the whole beam with an opposite angle with respect to channeling; it is caused by the elastic interaction of the protons with the crystalline interplanar potential. This deflection effect could be used for the crystal collimation instead of channeling which has a smaller efficiency and angular acceptance. Keeping in mind this goal the observation of the double reflection, obtained with two crystals in series, is a fundamental result as it demonstrates that, thanks to the volume reflection, a large deflection angle can be obtained with high efficiency.

A detailed analysis work has been performed on the data collected by the silicon microstrip detectors based on the AGILE satellite ones. A method to compute the proton outcoming angle from the crystal, which, exploiting the information from different detectors, increases the angular resolution and corrects for some systematic effects, has been developed. Using this method and the information of a detector placed near the crystal an analysis of the crystal properties as a function of the particles impact region on its surface has been carried out. This analysis revealed the presence of a crystal torsion along the vertical direction, observed in all the analyzed crystals; the entity of the torsion has been measured in the single crystal cases.

Also the double crystals scan is influenced by the torsion; this affects the alignment between the two crystals, which varies as a function of the vertical position.

This phenomenon has been used to discriminate the contribution of the two crystals in the combined scan and to investigate how the deflection parameters, during the multiple reflection, are influenced by the alignment level, showing that, without an almost perfect alignment, the volume reflection angular acceptance rapidly decreases.

A method to measure the efficiency of the different deflecting effects has been developed and applied on the anayzed crystals showing its consistence; the volume reflection efficiency is greater than 98% in agreement with theoretical and simulated predictions; the deflection efficiency of the double reflection (96.7%) is coherent with the hypothesis of two independent reflections and opens the way to the development of multicrystal reflectors to be used in a collimation system.

The encouraging results of this data taking led to the schedule of a series of new beam tests, the first of which was held in May 2007. This experiment was performed with a new detector setup satisfying the requirements born after the first run. The new setup is based on three detector stations located in a way that both the incoming and the outcoming angle to and from the crystal can be measured ensuring a better resolution on the single particle deflection angle measurement. This resolution, which is more than two times better than in the previous beam test and approaches the intrinsic limit of the measurement, has been achieved also minimizing the multiple scattering contributions. Moreover, the detection system is faster with a higher integration level between the DAQ, the detectors and the goniometric system.

Different measurements were performed: among them, a deep study of the volume reflection and of the axial channeling. The analysis is still ongoing.
In the thesis the results obtained with a multireflector composed of 5 quasimosaic crystals is presented as it represents the natural prosecution in the collimation system development. This crystal system showed a deflection angle of about 50 μrad maintaining an efficiency higher than 90%. Different multicrystal systems have been tested during the experiment and the particularity of the quasimosaic one is that its holder has the possibility to adjust the alignment between the crystals which turned out to be fundamental to reach the best results in terms of efficiency and angular acceptance.

The results obtained by the H8RD22 collaboration indicate that crystals for the LHC collimation upgrade are a real possibility. In the future, the ideal geometry of the multicrystal should be defined through simulations of the crystal physics and of the LHC collimation environment and new tests on the H8 beamline; one of the next tests for example will profit of an alignment system of the different crystals remotely controlled. At the same time, tests on a circular beam will be necessary to check the effective collimation efficiency in the final environment.

List of Figures

1.1 Crystalline planes and axis depending on the observation. 12
1.2 Representation of a particle trapped in the planar interatomic potential. 14
1.3 The potential generated by the (110) silicon plane in the Moliér approximation. 16
1.4 The diamond cubic lattice. 16
1.5 Miller indices in the cubic lattice system. 18
1.6 The interplanar Moliér potential for the (110) and the (111) Si channel. 18
1.7 Schematic view of a particle contained in the interplanar crystalline potential. 19
1.8 Simulated trajectories of 450 GeV/c protons in the phase space (x,θ) in the (111) silicon plane. 20
1.9 The dechanneling length, L_D trend as a function of the particles pv. 24
1.10 Schematic of a particle moving at a small angle with respect to a crystal axis. 25
1.11 Axial potential computed with the use of the Moliére approximation 26
1.12 The electron density and the mean energy loss, in the channel as a function of the transversal coordinate. 29
1.13 Energy loss spectra in a germanium crystal. 30
1.14 Photon energy spectra for a 10 GeV/c particle beam impinging on a silicon crystal. 31
1.15 The bent crystal working principle and an example of a bending device. 32
1.16 Scheme of the channeling motion of a particle which enters a bent crystal aligned with its planes. 33
1.17 The interplanar silicon ((110) planes) potential computed in the Molíer approximation for different bending radi. 35
1.18 The feed-in mechanism in straight and bent crystals. 38
1.19 Two schematic examples of volume captured particles in a bent crystal. 39

1.20 Reflection of a charged particle in the crystal volume. 42
1.21 Schematic of the effective potential at the reflection turning point. 43
1.22 Simulated angular distributions of 400 GeV protons scattered by a (110) silicon crystal bent with different curvature radii. 44
1.23 Simulated angular distributions of 400 GeV protons scattered by a (110) silicon crystal in reflection. 44
1.24 Layout of the experimental setup of the first experiment dedicated to the volume reflection observation. 47
1.25 The results of the first experiment dedicated to the volume reflection observation. 47

2.1 Extraction efficiency measured in the past SPS experiment as a function of the beam momentum. 52
2.2 Crystal extraction efficiency for 70 GeV protons as a function of the crystal length. 53
2.3 The radial beam profile observed at the entry face of the stainless steel absorber in the IHEP collimation experiment. 54
2.4 Beam profile measured on the collimator absorber entry face with 1.3 GeV protons. 55
2.5 The RHIC crystal collimation setup. 56
2.6 The O-shaped crystal. 57
2.7 A typical crystal angular scan with a gold ion beam (performed at RICH). 58
2.8 The beam horizontal phase space at the RHIC in the crystal collimator location. 59
2.9 Comparison between the 2001 RHIC data and Montecarlo simulation. 61
2.10 The relative background measured by the STAR experiment as a function of the distance between the crystal and the secondary collimator. 61
2.11 Proton halo rate recorded at the Tevatron by the two experiments CDF and D0. 63
2.12 Tevatron crystal collimation setup. 64
2.13 An angular crystal scan performed at the Tevatron. 65
2.14 RHIC data compared with several simulations with different number of turns. 66
2.15 Particle deflection angle distributions due to the passage through a misaligned crystal in the RHIC and Tevatron case. 67
2.16 Stored beam energy for various past, present and future high power accelerators. 68

2.17 Maximum energy deposit in different materials per mass length; Fluka simulation. 70
2.18 The LHC phase 1 collimators. 70
2.19 Layout for the LHC collimation during phase 1. 71
2.20 The LHC halo collimation. 72
2.21 Scheme of the crystal-based collimation system. 74
2.22 Simulated channeling efficiency at the LHC energy. 75
2.23 Scheme of the collimation system based on the volume reflection effect. 76
2.24 The preparation of the silicon crystal surface. 78
2.25 An IHEP radiation hardness test on a bent crystal. 79

3.1 The experimental setup of the September 2006 experiment. 82
3.2 Beam profile measured near the crystal. 83
3.3 Beam profile and beam divergence in the downstream region. . . . 84
3.4 Position of the AGILE silicon detectors. 85
3.5 The 4 x-y silicon chambers in the downstream region. 85
3.6 The minitracker and its 6 silicon x-y detectors. 85
3.7 A photo of the gas chamber during the experiment. 86
3.8 The goniometric system. 88
3.9 A scheme of the different stages of the goniometer. 89
3.10 Two examples of the crystals used during the experiment. 89
3.11 The bending principle of the strip crystals and a scheme of its bending device. 90
3.12 The bending principle of the quasimosaic crystals and a scheme of its bending device. 91
3.13 The origin of the quasimosaic curvature. 91
3.14 The laser pre-alignment technique and the lateral scan procedure with the lead strip. 93
3.15 The ST4 crystal scan (beam profile). 94
3.16 A frame of the ST4 crystal scan during channeling. 95
3.17 A frame of the ST4 crystal scan during reflection. 95

4.1 The residual of an AGILE microstrip silicon detector. 100
4.2 Comparison between the single module beam profile and the reconstructed one (ST4 crystal). 101
4.3 Comparison between the channeling peak in the beam profile method and in the reconstructed angle one (ST4 crystal). 102
4.4 Fit of the main peak with two gaussians (ST4 crystal). 103
4.5 Explanation of the systematic errors induced by the beam profile method (1). 104

4.6 Trend of the main peak, beam profile method (ST4 crystal). 105

4.7 Protons horizontal position with respect to their angle (ST4 crystal amorphous position). 106

4.8 Protons horizontal position with respect to their angle (ST4 crystal channeling and reflection position). 107

4.9 Trend of the main peak, beam profile method (ST4 crystal, one beam component is excluded). 108

4.10 Trend of the main peak, angular profile method (ST4 crystal, one beam component is excluded). 109

4.11 Explaination of the systematic errors induced by the beam profile method (2). 110

4.12 The ST4 crystal scan considering only the inner horizontal part of the beam (beam profile). 110

4.13 The ST4 crystal scan considering only the inner horizontal part of the beam (angular profile). 111

4.14 Volume reflection angle as a function of the horizontal position before the crystal. 111

4.15 Two frames of the QM2 crystal scan showing the protons horizontal position with respect to their angle. 112

4.16 Two frames of the double crystal scan showing the protons horizontal position with respect to their angle. 113

4.17 Three plots of the QM2 crystal scan during the channeling effect showing the beam angular profile with respect to the vertical beam profile at the crystal. 114

4.18 The QM2 crystal scan in different vertical regions of its surface. . 115

4.19 Angular shift of the channeling peak with respect to the vertical position on the QM2 crystal surface. 116

4.20 Angular shift of the main peak with respect to the vertical position on the QM2 crystal surface. 117

4.21 Two frames of the ST4 crystal scan, showing the protons vertical position at the crystal with respect to their angle. 118

4.22 The ST4 crystal scan in different vertical regions of its surface. . . 119

4.23 Angular shift of the channeling peak with respect to the vertical position on the ST4 crystal surface. 120

4.24 Angular shift of the main peak with respect to the vertical position on the ST4 crystal surface. 121

4.25 The double crystal scan (angular profile). 122

4.26 Study of the double crystal scan (1). 125

4.27 Study of the double crystal scan (2). 125

4.28 Study of the double crystal scan (3). 126

4.29 The QM1 and QM2 contribution in the double crystal scan. 127

4.30 The double crystal scan with the best alignment. 128
4.31 The double crystal scan with the worst alignment. 129
4.32 The main peak trend in the double crystal scan: comparison between best and worst alignment. 130
4.33 The channeling peak trend in the double crystal scan: comparison between best and worst alignment. 130
4.34 Number of events within 3σ from the main peak as a function of the goniometer angle (ST4 crystal). 133
4.35 Number of events within 3σ from the average positions of the main peak as a function of the goniometer angle (ST4 crystal). . . 134
4.36 The reflection efficiency computed with the described method with different sigma values. 135
4.37 The channeling peak trend during the ST4 crystal scan. 136
4.38 The channeling efficiency trend of the ST4 crystal as a function of the goniometer angle. 137
4.39 The channeling efficiency computed with the described method as a function of the chosen area. 138
4.40 The channeling efficiency trend of the ST4 crystal (data from a horizontal slice of 700 μm) as a function of the goniometer angle. 139
4.41 Regions in which the dechanneling and volume capture events are counted (ST4 crystal). 140
4.42 Background estimation in the ST4 crystal scan. 141
4.43 A photo of the QM2 crystal and the scan of the QM2 crystal. . . . 143
4.44 Result of the systematic gaussian fit on the QM2 angular scan. . . 144
4.45 Number of events within 3σ from the main peak as a function of the goniometer angle (QM2 crystal). 145
4.46 A systematic in the reflection efficiency computation of the QM2 crystal. 145
4.47 A frame of the QM2 scan which shows the volume capture peak. . 146
4.48 Bidimensional plot of the double crystal scan (angular profile method). 147
4.49 Reflection angle measurement in the double crystal scan. 148
4.50 Number of events within 3σ from the main peak as a function of the goniometer angle (double crystal). 148
4.51 The double crystal scan selecting the lower beam region. 149
4.52 Number of events within 3σ from the amorphous position and the reflection one (double crystal, best alignment). 150

5.1 A comparison between the September 2006 setup and the May 2007 one 155
5.2 The silicon telescopes on the H8 beamline 156
5.3 The residual of a silicon telescope 157

5.4 The QM2 crystal scan obtained with the silicon telescopes 158
5.5 A comparison between the performances of the September 2006 setup and the May one 159
5.6 An example of a lateral scan performed with the silicon telescope 160
5.7 An example of a fast angular scan with the silicon telescope . . . 161
5.8 Three crystals aligned for multireflection 162
5.9 The multicrystals mounted on their holder 162
5.10 The alignment of the MQM5 crystal 163
5.11 The 5 crystals of MQM5 aligned 164

List of Tables

1.1 Parameters of some planar channels in silicon, germanium and tungsten crystals. 17
1.2 Values of the dechanneling length for the single scattering at large angle as a function of the energy. 23
1.3 The potential well depth of some axial channels of silicon, germanium and tungsten crystals, in the Moliér approximation. 27

3.1 Geometrical parameters of the analyzed strip crystals. 90
3.2 Geometrical parameters of the analyzed QM crystals. 92

4.1 The measured ST4 parameters. 142
4.2 The measured QM2 parameters. 146
4.3 The double crystals reflection parameters. 151

List of acronyms

AC	Alternate Current
AGILE	Astro Rivelatore Gamma a Immagini LEggero
AMS	Alpha Magnetic Spectrometer
ASIC	Application Specific Integrated Circuit
CATCH	Crystal Channeling Simulation
CDF	Collider Detector at Fermilab
CERN	European Organization for Nuclear Research
CFC	Carbon Fiber Carbon
DC	Direct Current
D0	Particle experiment at Fermilab
DAQ	Data AcQuisition
fcc	face cubic centered
Fluka	A fully integrated particle physics MonteCarlo simulation package
FWHM	Full Width Half Maximum
FNAL	Fermi National Accelerator Laboratory
IHEP	Institute for High Energy Physics
INFN	Istituto Nazionale di Fisisca Nucleare
NA48	Particle experiment at CERN
LHC	Large Hadron Collider
PIN	P-type Intrinsic N-type diode
PNPI	Petersburg Nuclear Physics Institute
RHIC	Relativistic Heavy Ion Collider
SSC	Superconducting Super Collider
STAR	Solenoidal Tracker at RHIC
SPS	Super Proton Synchrotron
TCP	Primary collimator
TCS	Secondary collimator

Bibliography

[1] J. Stark. *Phys. Zs.*, 13(973), 1912.

[2] M. T. Robinson and O. S. Oen. *Phys. Rev. Lett.*, (132(5)):2385, 1963.

[3] G. R. Piercy, F. Brown, and J. A. Davies *et al.*. *Phys. Rev. Lett.*, (10(4)):399, 1963.

[4] J. Lindhard. *Phys. Lett.*, 12(126), 1964.

[5] D. S. Gemmel. *Rev. Mod. Phys*, 46(1), 1974.

[6] O. Fich *et al.*. *Phys. Lett.*, 57B:90, 1975.

[7] E. N. Tsyganov. *Fermilab reports TM-682,TM-684*, 1976.

[8] S. P. Mø ller. *CERN*, 94-05, 1994.

[9] V. M. Biryukov, Y. A. Chesnokov, and V. I. Kotov. *Crystal channeling and its application at high energy accelerators*. Springer, 1996.

[10] J. S. Foster *et al.*. *Nucl. Phys. B*, 318(301), 1989.

[11] J. U. Andersen. *Nucl. Instr. and Meth. B*, 33(24), 1998.

[12] V. Biryukov. Computer simulation of beam steering by crystal channeling. *Phys. Rev. E*, 51(4):3522–3528, 1995.

[13] Y. H. Ohtsuki and H. Nitta. *Software Practice and Experience*, 20(S2), 1999.

[14] V. M. Biryukov *et al.*. On measuring 70 GeV proton dechanneling lengths in silicon crystals (110) and (111). *Nucl. Instr. and Meth. B*, 86(245), 1994.

[15] V. G. Baryshevsky and V.V. Tichomirov. *Usp. Fiz. Nauk*, 159(527), 1989.

[16] L.D. Landau and E.M. Lifshits. *Mechanika (Mechanics)*, Nakua, Moscow 1973.

[17] H. Kumm *et al.*. *Radiat. eff.*, 12:52, 1972.

[18] A. Tamura and Ohtsjui. *Phys. status solidi B*, 62:477, 1974.

[19] L. D. Landau. *Phys. (USSR)*, 8:201, 1944.

[20] J.F. Bak *et al.*. *Nucl. Phys. A*, 389:533, 1982.

[21] S. Bellucci and V. A. Maisheev. Coherent bremsstrahlung in imperfect periodic atomic structures. *Phys. Rev. B*, 71:174105, 2005.

[22] Bak *et al.*. J. Channeling radiation from 2-55 GeV/c electron and positrons. *Nucl. Phys. B*, 254:491–527, 1985.

[23] A. M. Taratin and S. A. Vorobiev. *Nucl. Instr. and Meth. B*, 26(512), 1987.

[24] Yu. M. Ivanov, *et al.*. *Phys. rev. Lett.*, 84(144801), 2006.

[25] A. M. Taratin *et al.*. *Nucl. Instr. and Meth. B*, 262:340–347, 2007.

[26] V. V. Maischeev. *Arxiv:physics/0607009 v 1*, 2006.

[27] W. Scandale *et al.*. *Proceedings. of EPAC Edinburgh, Scotland*, 2004.

[28] Yu. M. Ivanov *et al.*. *JEPT lett.*, 81:99, 2005.

[29] A. G. Afonin, *et al.*. *Nucl. Instr. and Meth. B*, 234:14–22, 2005.

[30] A. G. Afonin, *et al.*. High-efficiency beam extraction and collimation using channeling in very short bent crystals. *Phys. Rev. Lett.*, 87(9):094802, 2001.

[31] E. Uggerhoj *et al.*. *Nucl. Instr. and Meth. B*, 234 (1-2):31–39, 2005.

[32] A. S. Denisov *et al.*. *Nucl. Instr. and Meth. B*, 69:382, 1992.

[33] A. Baurichter *et al.*. *Nucl. Instr. and Meth. B*, 27:164–165, 2000.

[34] A. S. Bellucci *et al.*. *Phys. Rev. Lett.*, 90:034801, 2003.

[35] V. V. Baublis *et al.*. *Nucl. Instr. and Meth. B*, 90:112, 1994.

[36] M. A. Maslov *et al.*. The SSC beam scraper system. *SSCL*, 484, 1991.

[37] K. Jukka. Proton extraction from a high energy beam with bent crystal. *PhD Thesis*, 1998.

[38] V. Biryukov. *Proceedings of the international Symposium on Near Beam Physics*, pages 179–184, sept 1997.

[39] A. Baurchter, *et al.*. *Nucl. Instr. and Meth. B*, 119:172–180, 1996.

[40] V. Biryukov. *Nucl. Instr. and Meth. B*, 53:202–207, 1991.

[41] A. G. Afonin, *et al.*. *Phys. Lett. B*, 435:240–244, 1998.

[42] R. P. Fliller. *Phys. Rev. Lett. STA B*, 9:013501, 2006.

[43] G. Arduini, *et al.*. *Phys. Rev. Lett.*, 79:4182, 1997.

[44] K. H. Ackermann *et al.*. STAR detector overview. *Nucl. Instr. and Meth. A*, 499:624–632, 2003.

[45] A. Drees *et al.*. First observation of proton reflection from bent crystals. *Proceedings. N. 773 AIP conference, New York*, 2006.

[46] D. Still. Tevatron bent crystal studies 2007. *Workshop talk: Crystal Channeling for Large Collider: Machine and Physics Application*, 2007.

[47] V. Biryukov. *Phys. Lett. B*, 645:47–52, 2006.

[48] P. Sievers *et al.*. Appropriate materials for LHC collimation. *LHC Performance Workshop - Chamonix XII*, 2003.

[49] LHC design report. *CERN*, chap. 18.

[50] H. Burkhardt *et al.*. Measurement of the LHC collimator impedance with beam in the SPS. *Proceedings PAC05*, 2005.

[51] R. W. Aßmann *et al.*. The final collimation system for the LHC. *Proceedings PAC06*, 2006.

[52] G. Robert-Demolaize *et al.*. Crytical halo loss location in the LHC. *Proceedings PAC06*, 2006.

[53] R. W. Aßmann *et al.*. Requirements for the LHC collimation system. *LHC-project-report-599*, 2002.

[54] V. M. Biryukov *et al.*. *Nucl. Instr. and Meth. B*, 234:23–30, 2005.

[55] V. Previtali. First ideas on implementation of crystal in LHC collimation system. *Workshop talk: Crystal Channeling for Large Collider: Machine and Physics Application*, 2007.

[56] R. W. Aßmann *et al.*. Collimator and cleaning: could this limit the LHC performance? *LHC Performance Workshop - Chamonix XII*, 2003.

[57] A. Vomiero. Characterization of crystals for relativistic channeling. *Workshop talk: Crystal Channeling for Large Collider: Machine and Physics Application*, 2007.

[58] A. Vomiero *et al.*. *Nucl. Instr. and Meth. B*, 249:903–906, 2006.

[59] S. I. Baker *et al.*. *Nucl. Instr. and Meth. B*, 90:119, 1994.

[60] B. Alpat *et al.*. *Nucl. Instr. and Meth. A*, 439:53, 2000.

[61] G. Barbiellini *et al.* The AGILE silicon tracker: testbeam results of the prototype silicon detector. *Nucl. Instr. and Meth. A*, 490:146–158, 2002.

[62] M. Prest *et al.* The AGILE silicon tracker: an innovative γ-ray instrument for space. *Nucl. Instr. and Meth. A*, 501:280–287, 2003.

[63] V. M. Samsonov. *Leningrad Inst. of Nuclear Physics, USSR Academy of Sciences*, preprint No. 278.

[64] V. M. Biryukov *et al.*. *Rev. Sci. Instrum.*, 73:9, 2002.

[65] S. Baricordi *et al.*. *Appl. Phys. Lett.*, 87:094102, 2005.

[66] Yu. M. Ivanov *et al.*. *JETP Lett.*, 81:99, 2005.

[67] W. Scandale *et al.*. High-Efficiency Volume Reflection of an Ultrarelativistic Proton Beam with a Bent Silicon Crystal. *Phys. Rev. Lett.*, 98:154801, 2007.

[68] L. Celano *et al.*. *Nucl. Instr. and Meth. A*, 381:49, 1996.